DIPLOMA THESIS

Numerical Computation of the Eddy Current Problem in Ferromagnetic Sheets by the Multiscale Finite Element Method Using the Vector Preisach Model

submitted at the

TU WIEN

Institute of Analysis and Scientific Computing

Under supervision of

Univ.Prof. Dipl.-Ing. Dr.techn. Joachim Schöberl
Dipl.-Ing. Dr.techn. Karl Hollaus

by

Valentin Hanser, BSc
Matr.Nr. 1325081

4th March, 2021

Abstract

To facilitate the design of electrical machines and transformers and to meet today's economic as well as ecological requirements, an efficient simulation of the electromagnetic fields using the finite element method (FEM) is indispensable.

The iron core of electrical machines and transformers is composed of many very thin sheets with excellent magnetic properties in order to keep the eddy currents and the associated losses as small as possible and to optimally guide the magnetic flux. Modelling of each single sheet by finite elements requires the solution of huge nonlinear equation systems which would make routine simulations of practically relevant problems impossible.

In the present work, a mixed multiscale finite element method (MMSFEM) was used to cope with the problem of laminated cores. A vector Preisach model was developed to account for hysteresis of ferromagnetic materials as accurately as possible with little computational effort.

The integration of hysteresis into the FEM is carried out by a differential permeability to avoid singular points occurring in case of the permeability. For simulations of magneto-static problems and eddy current problems (ECPs), a magnetic scalar potential or a mixed formulation with the current vector potential were used, respectively. This allows to directly determine the magnetic field strength from the respective potential formulation and, thus, to efficiently use the Preisach model in the so-called forward mode. The nonlinear equation system was solved by a fixed-point method.

Starting from linear via nonlinear materials with a given magnetisation curve to materials with a scalar and vector hysteresis, the developed hysteresis models were verified step-by-step as described in a scheme. Simulations with the MMSFEM were verified using reference solutions in which each single sheet was considered in the finite element model for the solution with the standard finite element method.

Finally, the ECP of a practically relevant single-phase transformer considering vector hysteresis was simulated with great success. The results were presented at the international IGTE Symposium 2020 in Graz and submitted for publication in the international peer-reviewed journal COMPEL.

Key words:
differential permeability / eddy current problem / ferromagnetic sheets / fixed-point method / mixed multiscale finite element method / nonlinear equation system / numerical computation / vector Preisach model

Kurzfassung

Um den Entwurf elektrischer Maschinen und Transformatoren wesentlich zu erleichtern und den heutigen ökonomischen als auch ökologischen Anforderungen gerecht zu werden, ist eine effiziente Simulation der elektromagnetischen Felder mit der Finite-Elemente-Methode (FEM) unumgänglich.

Der Eisenkern elektrischer Maschinen und Transformatoren wird aus vielen sehr dünnen Blechen mit ausgezeichneten magnetischen Eigenschaften hergestellt, um die Wirbelströme und die damit verbundenen Verluste möglichst klein zu halten und um den magnetischen Fluss optimal zu führen. Würde man jedes einzelne Blech im Finite-Elemente-Modell auflösen, wäre ein extrem großes nichtlineares Gleichungssystem zu lösen, was routinemäßige Simulationen der Wirbelströme praktisch relevanter Probleme unmöglich machen würde.

In der vorliegenden Arbeit wurde eine gemischte Mehrskalen-FEM (GMSFEM) verwendet, um das Problem geblechter Kerne zu lösen. Ein Vektor-Preisach-Modell wurde entwickelt, um die Hysteresis ferromagnetischer Materialen möglichst genau und mit wenig Rechenaufwand zu berücksichtigen.

Die Integration der Hysteresis in die FEM erfolgt durch eine differentielle Permeabilität, um singuläre Punkte wie sie bei der Permeabilität auftreten, zu umgehen. Für Simulationen von Problemen in der Magnetostatik und von Wirbelstromproblemen (WSP) wurde ein magnetisches Skalarpotential bzw. eine gemischte Formulierung mit dem elektrischen Vektorpotential verwendet. Damit kann unmittelbar aus den Potentialformulierungen die magnetische Feldstärke ermittelt werden und somit das Preisach-Modell effizient im sogenannten forward mode genutzt werden. Das nichtlineare Gleichungssystem wurde mit einer Fixpunktmethode gelöst.

Zur Verifikation der entwickelten Hysterese-Modelle wurde ausgehend von linearen über nichtlineare Materialien mit gegebener Magnetisierungskennlinie hin zu Materialien mit skalarer und vektorieller Hysteresis, Schritt für Schritt vorgegangen und in einem Schema festgehalten. Simulationsergebnisse mit der GMSFEM wurden anhand von Referenzlösungen, in denen jedes einzelne Blech im Finite-Elemente-Modell für die Lösung mit der Standard-FEM berücksichtigt wurden, überprüft.

Letztlich wurde mit großem Erfolg das WSP eines praktisch relevanten Einphasentransformators unter Berücksichtigung von vektorieller Hysteresis simuliert. Die Ergebnisse wurden auf dem internationalen IGTE Symposium 2020 in Graz präsentiert und zur Veröffentlichung in das international peer-reviewed Journal COMPEL eingereicht.

Schlagwörter: differentielle Permeabilität / Wirbelstromproblem / ferromagnetische Bleche / Fixpunktmethode / gemischte Mehrskalen-Finite-Elemente-Methode / nichtlineares Gleichungssystem / numerische Berechnung / Vektor-Preisach-Modell

Danksagung

Zunächst möchte ich mich bei Herrn Prof. Joachim Schöberl bedanken, der mir diese Arbeit in seinem Forschungsgebiet "Scientific Computing and Modelling" ermöglicht hat.

Besonders dankbar bin ich für die unermüdliche Unterstützung von Herrn Dr. Karl Hollaus, der die Idee und den Inhalt dieser Arbeit vorgeschlagen hat und immer mit einem offenen Ohr zur Verfügung gestanden ist und unzählige Verbesserungsvorschläge eingebracht hat. Des weiteren ermöglichte mir Herr Dr. Karl Hollaus eine finanzielle Unterstützung im Rahmen des Forschungsprojekts "Multi-Scale Finite Element Methods for Eddy Current Problems MSFEM4ECP" P31926 gefördert von FWF der Wissenschaftsfonds und die Teilnahme am IGTE Symposium 2020 in Graz.

Des weiteren möchte ich mich bei Herrn Dipl. Ing. Markus Schöbinger bedanken, der mir die Grundgerüste der implementierten Methoden zur Verfügung gestellt hat.

Allen anderen Kollegen aus der Arbeitsgruppe möchte ich für die herzliche Aufnahme danken.

Table of Contents

1 Introduction

In electrical devices dealing with magnetic fluxes, such as transformers or electrical machines, iron cores are used to conduct the magnetic flux. If the magnetic flux varies in time, eddy currents occur. Therefore, the iron core is laminated to reduce eddy current losses. The simulation of these devices allows to optimise the geometry and to reduce the losses due to eddy currents and hysteresis phenomena. Simulating the electromagnetic field, the thermal field and the mechanical stress in electrical devices, before they are built, offers a huge economical and ecological benefit. An improvement of the fundamental mathematical simulation models with respect to accuracy and computational costs will meet these goals even better.

The finite element method (FEM) allows to model complex geometries and is widely used in industry to solve the Maxwell's equations. Although FEM software has improved a lot, simulating laminated iron cores is still a challenging task, since each laminate has to be modelled individually. Moreover, electrical devices often use ferromagnetic materials. Suitable material models are required to cope with hysteresis. The simulation of hysteresis phenomena increases the computational requirements enormously.

In the frame of this thesis, a high performing scalar Preisach model (SPM) with a verification scheme will be introduced, see Section 2. The SPM deals with the mathematical description of scalar hysteresis [1]. To measure the performance of different implementations, a test set up is defined. The results of the measurements are shown for the forward and the inverse mode of the SPM. Beside that, different Everett functions (EFs) representing physical and non-physical materials are developed.

For accurate simulations of hysteresis, the vector Preisach model (VPM) can be used, see Section 3. The VPM is a superposition of SPMs which requires a feasible distribution of SPMs on the surface of a unit sphere. To evaluate the quality of this distribution, a measure is introduced and applied to several distributions.

Manipulating the parameters of the EF, see Section 2.2.1 and Section 2.3, the implemented scalar and vector Preisach models can be verified against reference models using energy based considerations, see Section 2.14 and Section 3.6.

The implemented Preisach models are integrated into the FEM software Netgen/NGSolve to easily simulate electromagnetic problems considering hysteresis phenomena [2]. To this end, different characteristic numerical examples are presented. The first example, see Section 5, investigates the fixed-point method. The second example, see Section 6, is a meaningful application for the inverse mode of the scalar Preisach model (iSPM) in which a ferromagnetic core is excited by a coil. The third example, see Section 7, deals with the static magnetic field in a rectangular laminated core excited by a filamentary current and considers the ferromagnetic material by the VPM. The fourth example, see Section 8, additionally considers eddy currents and an excitation prescribed by the Biot-Savart field of a rectangular current loop. The last example, see Section 9, introduces the mixed multiscale finite element method (MMSFEM) by solving the eddy current problem (ECP) in a single-phase transformer with up to 184 sheets with an excitation prescribed by the Biot-Savart field of four coils. The MSFEM avoids the need to model each single sheet by finite elements (FEs) and thus allows an efficient simulation of ECPs in laminated cores [3]. The MSFEM exploits the fact that the problem exhibits two different scales [4].

The scheme illustrated in Fig. 1.1 is used to verify all presented simulations. For each verification step, a more complex model is reduced in such a way that it is equivalent to a less complex model. Modifying the model parameters of the VPM, simulations with VPM can be verified against linear or nonlinear models without hysteresis.

- The verification is based on an available analytic solution.

- For time-dependent field problems, like the ECP, a calculation in the frequency domain can be carried out in the next step. However, only harmonic excitations and linear material relations can be considered.
- The allowance of arbitrary excitation forms requires a time-stepping method like the backward Euler method.
- The consideration of nonlinear material relations requires iterative nonlinear solvers, like the fixed-point method.
- In order to deal with ferromagnetic materials and the associated hysteresis, a differential approach is necessary.

In some cases the SPM can be used instead of the VPM. These cases are not denoted independently in the scheme but can be considered in the same way as the VPM.

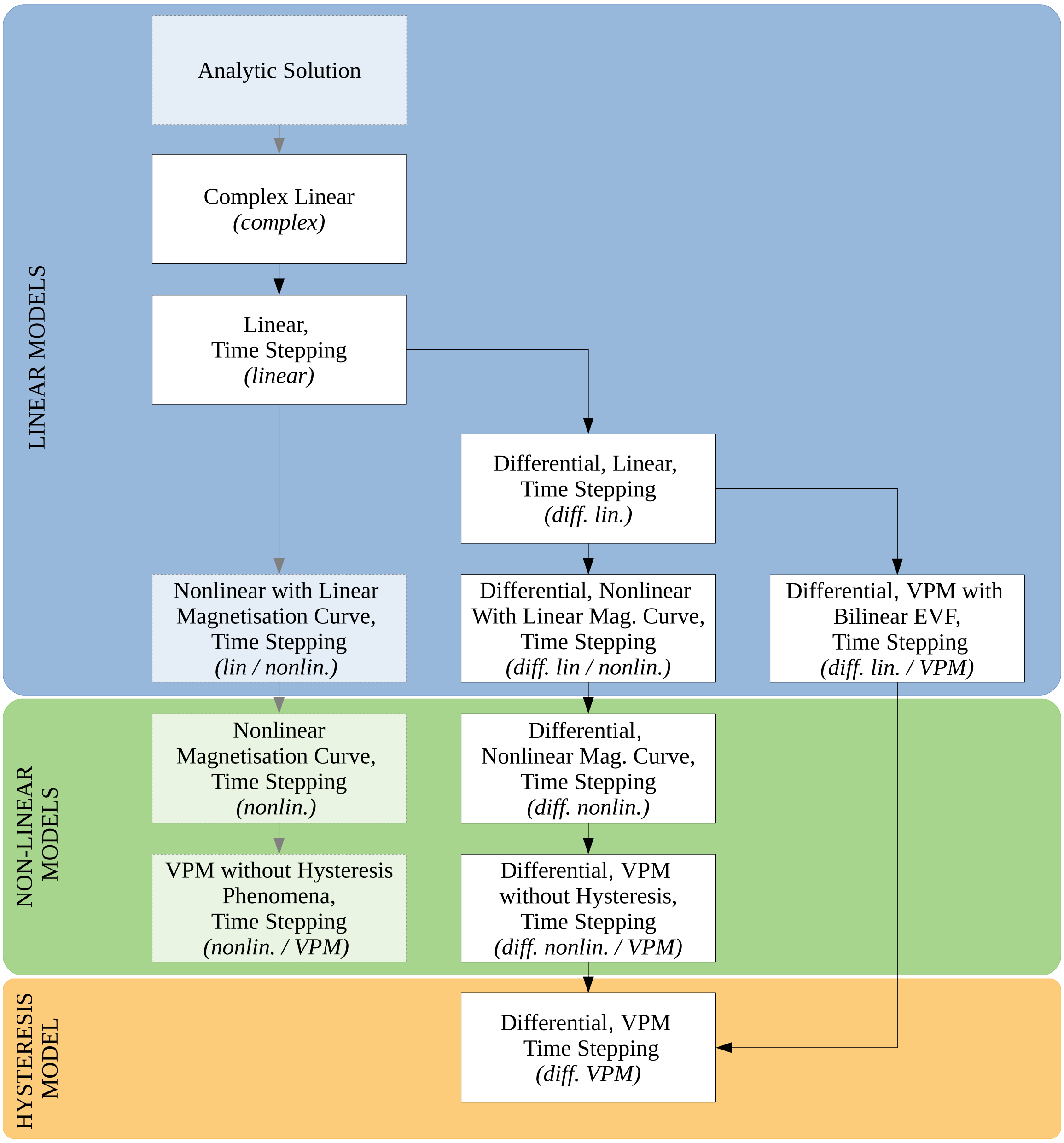

Figure 1.1: Verification scheme for all simulations. Abbreviations in brackets.

2 Scalar Preisach Model

The scalar Preisach model was developed by F. Preisach in 1935 and further extended by I. D. Mayergoyz [1]. The model describes a hysteresis phenomenon, as it appears for instance in ferromagnetic materials.
Considering this behaviour as a system, it can be described as shown in Fig. 2.1.

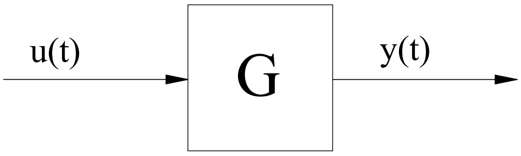

Figure 2.1: Scalar Preisach model as a system.

The scalar output signal $y(t)$ corresponding to the scalar input signal $u(t)$ of the system is not only affected by the current input state, but depends also on its past values.

2.1 Theoretical Description

The fundamental idea for the scalar Preisach model (SPM) consists of describing the hysteresis effect through an infinite number of two-state operators $\gamma_{\alpha\beta}[u(t)]$ connected in-parallel. These basic operators are called hysterons. The two values α and β, with $\alpha \geq \beta$, act as 'on' and 'off' thresholds for each hysteron. As soon as the input signal $u(t)$ exceeds the value α, the hysteron is set into the 'on' state. Analogously, if the input signal is smaller than the threshold β, the hysterons state is 'off'. In between these two thresholds, the previously set state remains. Therefore, the output of each hysteron is not only depending on the current state of the input signal, but also depends on its past. This process is illustrated in Fig. 2.2.
In order to describe a specific material, each hysteron is weighted with a previously determined function $\mu(\alpha, \beta)$, which is called the Preisach function. The output signal $y(t)$ of the system is calculated by integrating an infinite number of weighted hysterons over the Preisach plane T_{max} defined in (2.1).

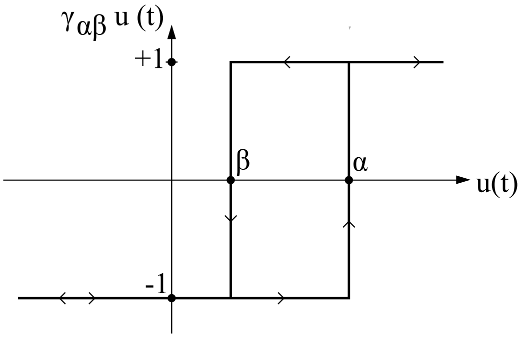

Figure 2.2: A basic operator of the Preisach model, called hysteron.

Since this thesis will describe hysteresis in a magnetic context, the input value is the magnetic field strength H and the output value the magnetic flux density B. Therefore, the Preisach plane T_{max}, see Fig. 2.5, is defined by the triangle

$$T_{max} := \{(\alpha, \beta) : \alpha \geq \beta, \alpha \leq H_{max}, \beta \geq -H_{max}\}. \tag{2.1}$$

The value H_{max} corresponds to the magnetic field strength which is needed to achieve a fully saturated material. The magnetic flux density of a saturated material is B_{max}.

The Preisach model is then described as

$$B(t) = \hat{\Gamma}[H(t)] = \iint_{T_{max}} \mu(\alpha,\beta)\gamma_{\alpha\beta}[H(t)]\,d\alpha d\beta, \tag{2.2}$$

where the specific material is considered in the Preisach function $\mu(\alpha, \beta)$. The operator $\hat{\Gamma}$ is used for the concise notation of the Preisach hysteresis operator.

Since the SPM is a time-variant system, an initial condition has to be defined. Usually, the SPM is initialised in the negative saturation. Therefore, the initial input and output signals are $H(t_0) = -H_{max}$ and $B(t_0) = -B_{max}$, which represent the negative saturation. Hence, all hysterons are initially set to the 'off' state. A subsequent increasing input signal $H(t)$, with $\frac{d}{dt}H(t) > 0$, will set all hysterons with $\alpha \leq H(t)$ into the positive state. In the Preisach plane this process is reflected by a horizontal line, which moves from the bottom to the top. A descending input signal, with $\frac{d}{dt}H(t) < 0$, is reflected analogously by a vertical line moving from the right to the left. Input signals with $\frac{d}{dt}H(t) = 0$ do not change the state of the SPM. For input values greater than H_{max} or smaller than $-H_{max}$ the hysteresis phenomenon is neglected by the model.
Further, considering all hysterons in the current state, the Preisach plane can be divided into two sets, one set $S_+(t)$ with all hysterons in the 'on' state and the counter set $S_-(t)$ in the 'off' state. The interface dividing these two sets is called staircase line and is defined by the minima m_k and the maxima M_k in the history of the input signal. Mayergoyz shows that the output value of a rate-independent SPM only depends on the extrema of the input signal [1, p. 11][5, p.27].
The initial state is not considered as extrema. However, the current state of the input signal $H(t)$ is considered as maximum and as minimum. Therefore, increasing signals result in an equal number of minima and maxima. As shown in Fig. 2.3, there is one minimum less than there are maxima for decreasing signals. To distinguish between the actual input signal and the sequence of the extrema of the input signal, the latter is called input sequence. Due to the rate-independence of the SPM, the input sequence can result from different input signals.

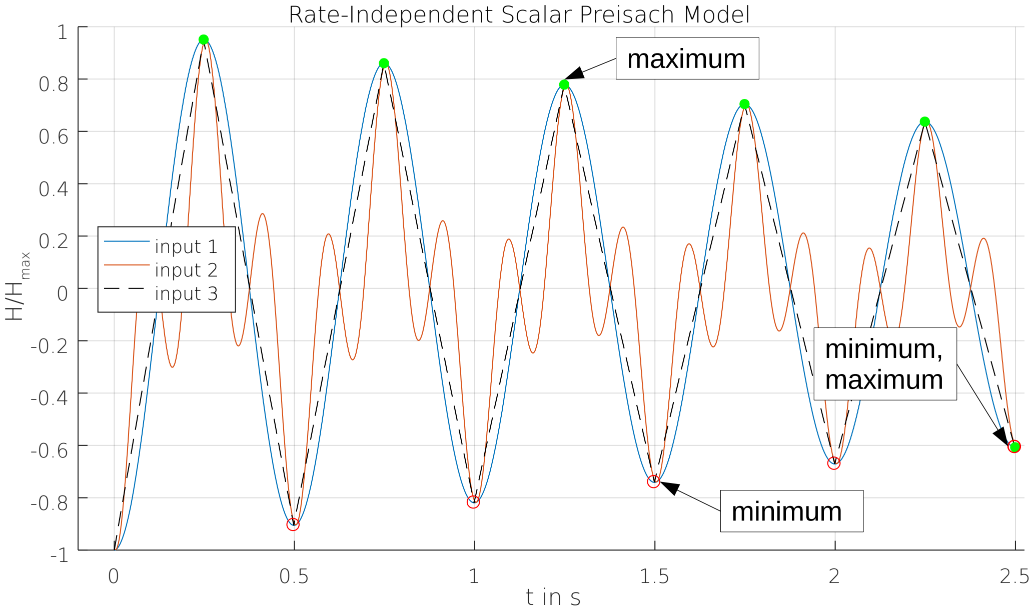

Figure 2.3: For a rate-independent SPM the signal form between two extrema does not matter. All input signals result in the same output of a SPM.

An arbitrary state of the SPM with the corresponding staircase line and the sets $S_+(t)$ and $S_-(t)$ is shown in Fig. 2.4.

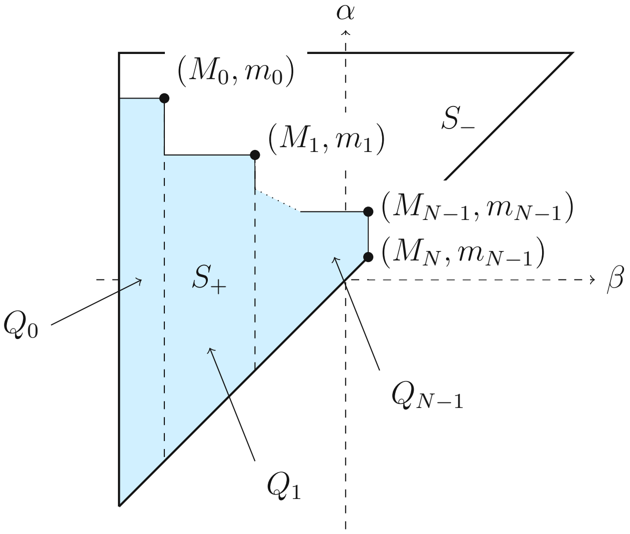

Figure 2.4: Staircase line in the Preisach plane with the extrema (M_i, m_i).

With the sets $S_+(t)$ and $S_-(t)$, (2.2) can be rewritten as

$$B(t) = \iint_{S_+(t)} \mu(\alpha,\beta)\; d\alpha d\beta - \iint_{S_-(t)} \mu(\alpha,\beta)\; d\alpha d\beta \tag{2.3}$$

$$= -\iint_{T_{max}} \mu(\alpha,\beta)\; d\alpha d\beta + 2\iint_{S_+(t)} \mu(\alpha,\beta)\; d\alpha d\beta. \tag{2.4}$$

Assuming the positive or the negative state for all hysterons results in the output value of positive or negative saturation of the the SPM, respectively. Therefore, the simplification

$$B(t) = -B_{max} + 2\iint_{S_+(t)} \mu(\alpha,\beta)\; d\alpha d\beta \tag{2.5}$$

can be used. Moreover, the set $S_+(t)$ can be divided into a sum of N trapezoids $Q_k(t)$, see Fig. 2.4. Consequently, the output value can be calculated as

$$B(t) = -B_{max} + 2\sum_{k=0}^{N-1} \iint_{Q_k(t)} \mu(\alpha,\beta)\; d\alpha d\beta. \tag{2.6}$$

The integration

$$E(\alpha,\beta) = 2\iint_{T(\alpha,\beta)} \mu(\alpha,\beta)\; d\alpha d\beta \tag{2.7}$$

of the Preisach function $\mu(\alpha,\beta)$ over a triangle $T(\alpha,\beta)$, as shown in Fig. 2.5, yields the Everett function (EF).

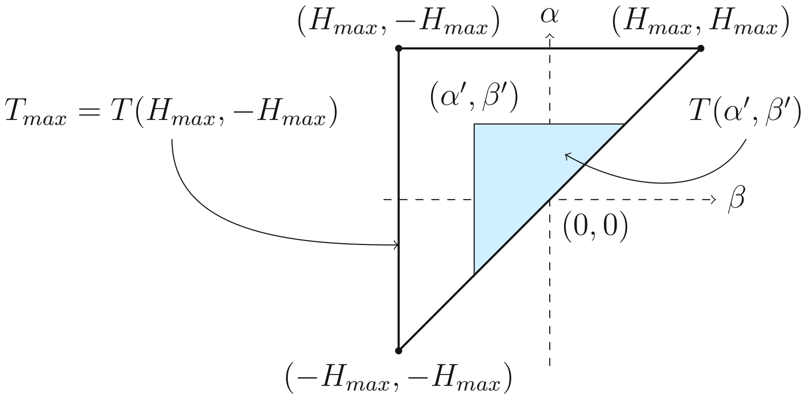

Figure 2.5: Triangle $T(\alpha', \beta')$ in the Preisach plane.

The maximum value of the EF is located at the point $(H_{max}, -H_{max})$ and the corresponding function value is $2B_{max}$. Additionally, the EF is symmetric along $\alpha = -\beta$ in most cases, i.e. $\mu(\alpha, \beta) = \mu(-\beta, -\alpha)$. Different EFs are discussed in Section 2.2. Further, each trapezoid Q_k can be calculated by a difference of the triangles $T(M_k, m_{k-1})$ and $T(M_k, m_k)$

$$B(t) = -B_{max} + 2 \iint_{Q_0} \mu \, d\alpha d\beta + 2 \sum_{k=1}^{N-1} \Big[\iint_{T(M_k, m_{k-1})} \mu \, d\alpha d\beta - \iint_{T(M_k, m_k)} \mu \, d\alpha d\beta \Big]. \tag{2.8}$$

This approach is valid for increasing and decreasing signals equally, since $T(\alpha, \beta) = 0$ for all $\alpha \leq \beta$. Moreover, to handle the first trapezoid Q_0 smoothly, a virtual minimum $m_{-1} = -H_{max}$ can be considered. With this approach, no special treatment for Q_0 is necessary. With the consideration of (2.7)

$$B(t) = -B_{max} + \sum_{k=0}^{N-1} \Big[E(M_k, m_{k-1}) - E(M_k, m_k) \Big] \tag{2.9}$$

represents the final equation for the calculation of the output value of the SPM. The value N is equivalent to the number of minima and therefore equivalent to the number of corners in the staircase line.

The Preisach model proposed by [1] does not consider input values H exceeding the saturation values $\pm H_{max}$. Therefore, these cases have to be handled in a feasible numerical scheme.

Pre-computing the Everett Function For a good performance, all necessary values of (2.7) should be pre-computed and stored. This approach is especially relevant for discretised EFs in Section 2.4.

Cumulative Sum Another increase in terms of the performance can be achieved by storing the subtotals of the sum in (2.9). This approach avoids recalculation of previously calculated results and is particularly useful when the input varies in a limited range without wiping out all previous extrema [6].

2.2 Everett Functions

The EF reflects the physical behaviour of a certain material. An analytic interpretation of the EF can either be based on a set of measured values for second-order reversal curves [1, p. 18] or on a parameter-identification problem fitting the major loop. The major loop is the sequence of input-output pairs of the SPM, which is adjacent to the saturation points $(-H_{max}, -B_{max})$ and (H_{max}, B_{max}). Fig. 2.6 illustrates the major loop. Additionally, Fig. 2.6 depicts the initial magnetisation curve and some minor loops.

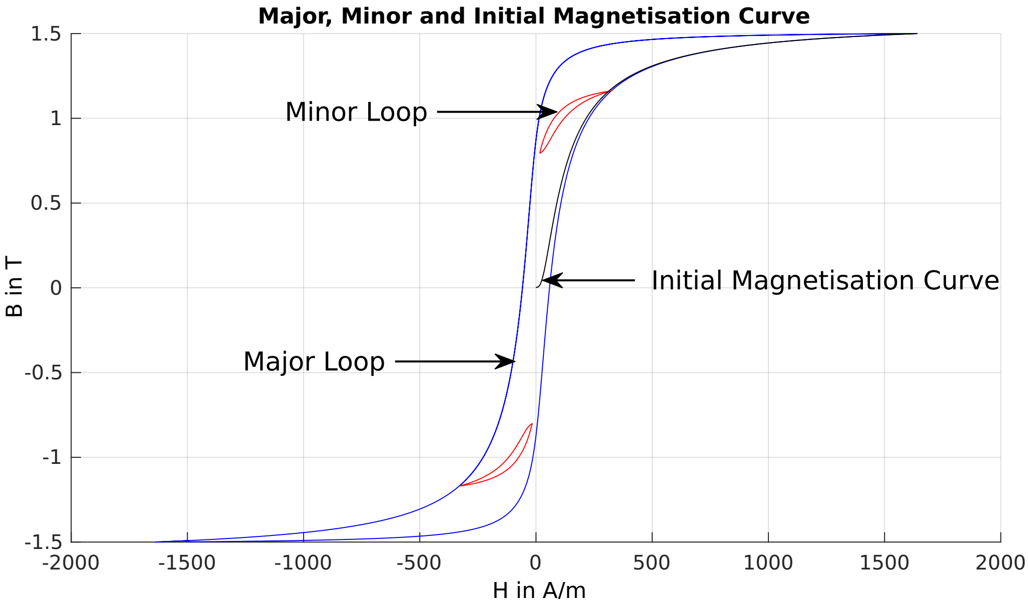

Figure 2.6: Major loop, minor loop and the initial magnetisation curve of a material.

For different materials different material-parameters for the EFs have to be found. As mentioned before, the straight-forward approach is to fit the parameters of an analytic function, so that the resulting major loop approximates the material sufficiently.
Experiments with EFs haven shown that for common industrial materials

- the gradient of the EF in the direction towards the point $(H_{max}, -H_{max})$

  $$\nabla E(\alpha, \beta) \cdot \big((-H_{max} - \beta)\mathbf{e}_\alpha + (H_{max} - \alpha)\mathbf{e}_\beta\big) > 0 \tag{2.10}$$

  has to be positive for all α, β in the Preisach plane,
- all values of the EF at the line $\alpha = \beta$ have to be zero and
- the EF is symmetrical along the line $\alpha = -\beta$.

As illustrated in Fig. 2.7, a EF which is not symmetrical along the line $\alpha = -\beta$ has different absolute values for the negative remanence $|B_{r,neg}|$ and positive remanence $|B_{r,pos}|$. Analogously, the absolute value of the negative and positive coercivity are not equal. Further, the demagnetisation approach described in Section 2.6 does not result in an output value $B_{demag} = 0$ but in an output value $B_{demag} = \frac{1}{2}(B_{r,pos} + B_{r,neg})$.
Fig. 2.8 illustrates the initial magnetisation curves and major loops of two EFs which violate the positive gradient requirement (2.10). The maximum of the output value does not result from the maximum of the input signal. In some cases the output signal B of the according SPM is decreasing although the input signal H is increasing.

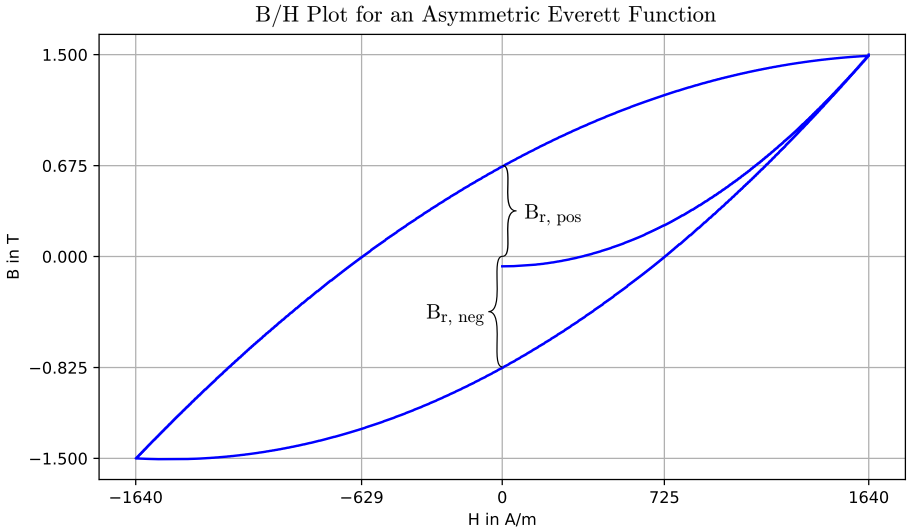

Figure 2.7: Initial curve and major loop of SPM with an asymmetric EF. The positive and negative remanence are different.

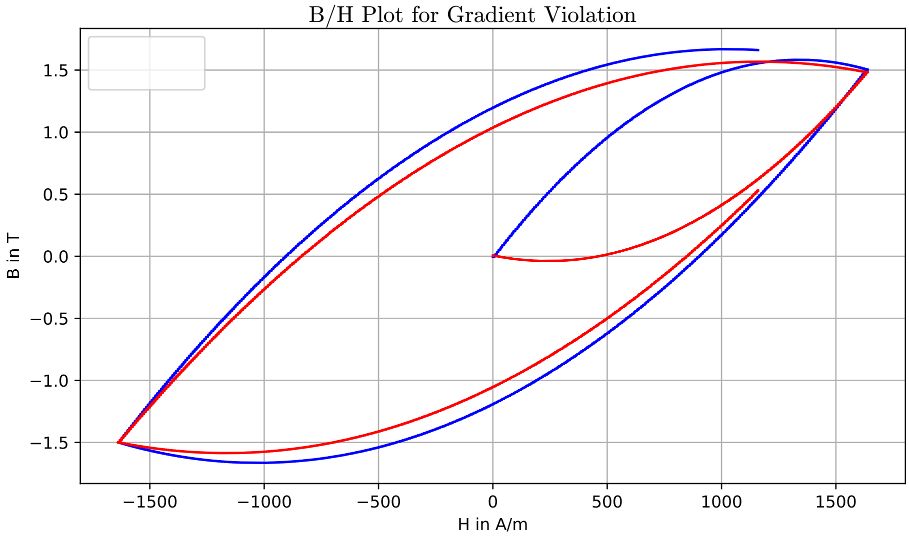

Figure 2.8: Initial curve and major loop of two SPMs with two parabolic EFs which both violate the gradient requirement (2.10) for industrial materials.

2.2.1 Everett Functions for the Verification Scheme

The verification scheme shown in Fig. 1.1 requires the possibility of a model reduction. The full Preisach model should then be equal to a linear or a nonlinear model. Since the material relation of a SPM is reflected by the EF, special EFs are defined in this section.

Bilinear Everett Function For a SPM that should have the same behaviour as a linear material, the bilinear EF

$$E(\alpha,\beta) = B_{max}\left(\frac{\alpha}{H_{max}} - \frac{\beta}{H_{max}}\right). \tag{2.11}$$

fulfils is considered for bounded input values. The corresponding Preisach model will behave equivalently to a model using the linear material relation $B = \mu_0\mu_r H = \frac{B_{max}}{H_{max}}H$, where μ_0 and μ_R are the permeability of vacuum and the relative permeability, respectively.

Parabolic Everett Function Another EF is based on a polynomial

$$E(\alpha,\beta) = a\alpha^2 + b\beta^2 + c\alpha\beta + d\alpha + e\beta \tag{2.12}$$

with fitting coefficients $a, b, \ldots, e$ and $\alpha, \beta \in [-H_{max}, H_{max}]$. The coefficients have to be defined so that a meaningful hysteresis will be generated. With the root points defined in Table 1 and the according coefficients, the previously defined requirements for EFs are fulfilled for all $r \in (\frac{1}{2}, \frac{3}{2})$. If the value $r = 1$ is used, the parabolic EF is equivalent to the bilinear EF.

α	β	$E(\alpha,\beta)$
0	0	0
H_{max}	H_{max}	0
$-H_{max}$	$-H_{max}$	0
H_{max}	$-H_{max}$	$2B_{max}$
0	H_{max}	$r\ B_{max}$
H_{max}	0	$r\ B_{max}$

$$a = \frac{B_{max}}{H_{max}^2}(1-r)$$
$$b = \frac{B_{max}}{H_{max}^2}(1-r)$$
$$c = \frac{B_{max}}{H_{max}^2}(2r-2)$$
$$d = \frac{B_{max}}{H_{max}}(2r-1)$$
$$e = \frac{B_{max}}{H_{max}}(1-2r)$$

Table 1: Used root points (left) and calculation of the coefficients (right) with the variable r .

The limits for r can be derived by the requirement of the EF that the minima have to be located at the line $\alpha = \beta$ and the maximum is located at $(H_{max}, -H_{max})$. Fig. 2.9 depicts the parabolic EF with marked root points. In the displayed case, the parameter r is set to $r = 0.6$.

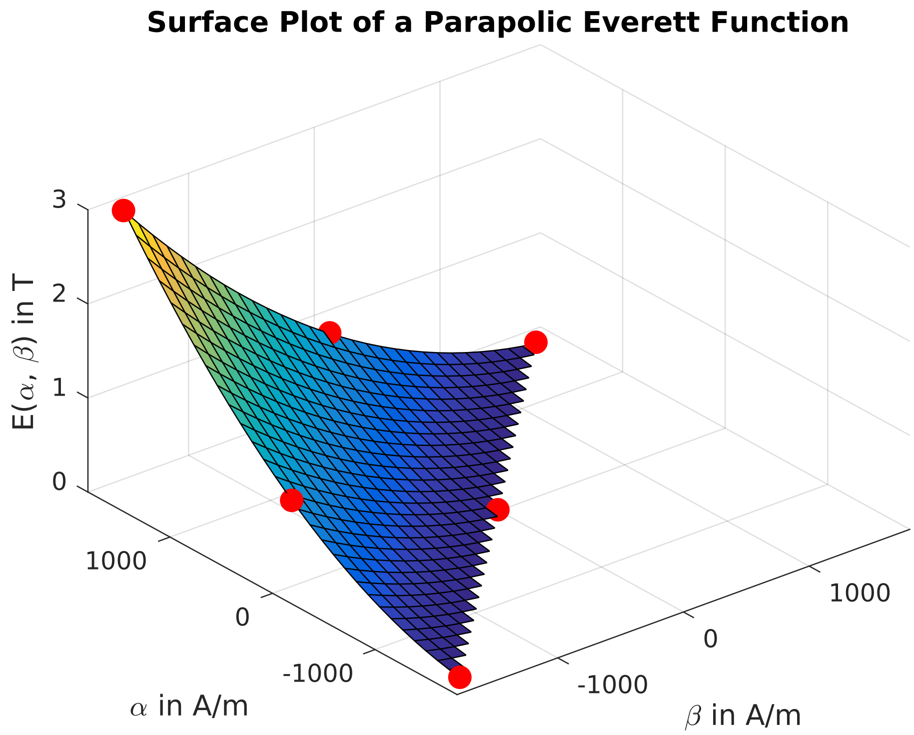

Figure 2.9: EF based on a paraboloid $N_A = 30$, $H_{max} = 1640 A/m$, $B_{max} = 1.5T$ and $r = 0.6$ with marked root points.

This EF does not necessarily reflect an existing material and is therefore useful for development only.

Everett Function based on a Magnetisation Curve A EF can be derived from a known magnetisation curve

$$[(H_i, B_i)], \tag{2.13}$$

which could for instance be the initial magnetisation curve of a ferromagnetic material. This procedure is based on (2.22) which describes the generation of an EF without hysteresis on the base of another EF. With the discrete function $B(H_i) = B_i$ representing the magnetisation curve, the EF is calculated by

$$E(\alpha, \beta) = B(\alpha) - B(\beta). \tag{2.14}$$

The python example Section D shows an example for the generation of an EF based on an initial magnetisation curve. The example compares the direct usage of magnetisation curve with an interpolated usage of the same magnetisation curve.

2.2.2 Everett Functions for Industrial Materials

Everett Function based on the Arctangent Function The EF

$$E(\alpha, \beta) = \left(arctan(a\alpha) - arctan(a\beta)\right)^b + \left(arctan(c\alpha)^3 - arctan(c\beta)^3\right)^d, \tag{2.15}$$

suggested by [7] with the parameters $a = 0.0196483$, $b = 2.95329554$, $c = 0.02211744$ and $d = 1.04359946$, is an approximation for the material M400-50A, which is used for electrical devices. Fig. 2.10 shows a surface plot of this EF.

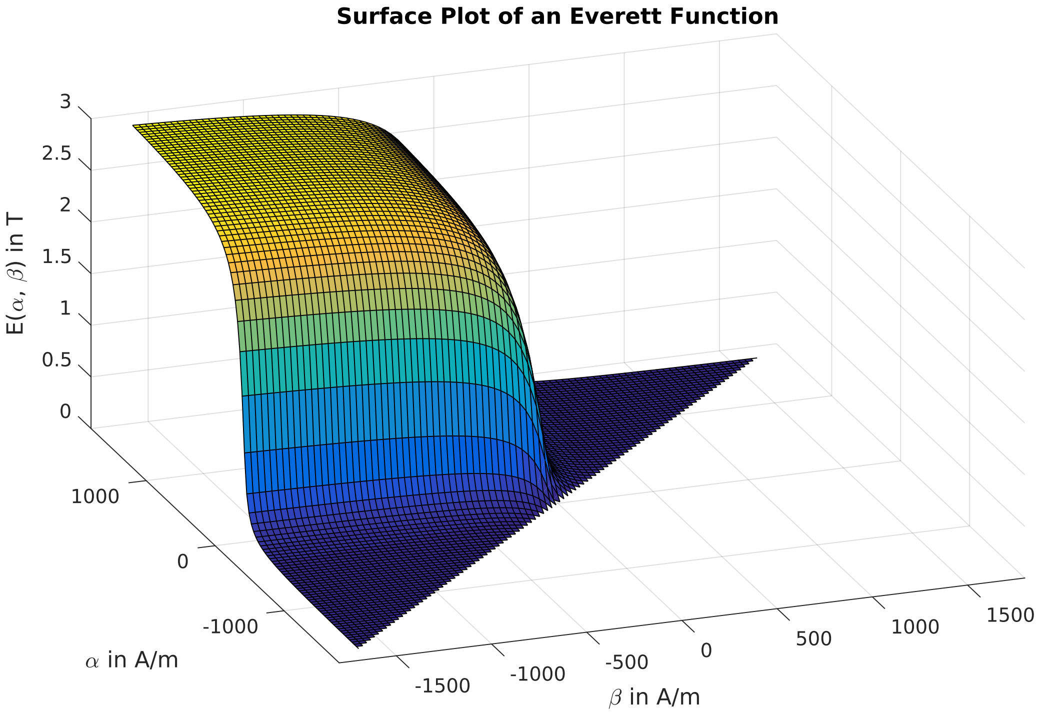

Figure 2.10: EF based on the arctangent function with $N_A = 101$, $H_{max} = 1640$A/m and $B_{max} = 1.5$T.

Everett Function based on the Lorentzian Preisach Function The EF

$$\begin{aligned}E(\alpha,\beta) =&K_1 b^2 arctan\Big(\frac{\beta+a}{b}\Big)\Big(arctan\Big(\frac{\beta-a}{b}\Big) - arctan\Big(\frac{\alpha-a}{b}\Big)\Big)\\ &+ K_2 e\Big(arctan\Big(\frac{\beta}{e}\Big) - arctan\Big(\frac{\alpha}{e}\Big)\Big) + f(\beta-\alpha)\\ &- \int_{\alpha}^{\beta} \frac{K_1 b^3 arctan(\frac{\xi+a}{b})}{\xi^2 - 2a\xi + a^2 + b^2}\, d\xi\end{aligned} \tag{2.16}$$

is derived from the Lorentzian Preisach function and can be found for instance in [7]. The corresponding parameters in Table 2 have been obtained by a least square fitting of the major loop for two different frequencies. The used material is M400-50A. The evaluation of the analytic function of the Lorentzian EF is time-consuming. Therefore, the Everett matrix should be pre-computed.

	10 Hz	50 Hz
a	$-5.65895187 \cdot 10^{1}$	$-8.18773707 \cdot 10^{1}$
b	$3.52032590 \cdot 10^{1}$	$4.13538892 \cdot 10^{1}$
K_1	$1.72599749 \cdot 10^{-2}$	$2.00442033 \cdot 10^{-2}$
K_2	$2.07211005 \cdot 10^{-1}$	$2.49345353 \cdot 10^{-1}$
e	$1.32612003 \cdot 10^{2}$	$1.33306276 \cdot 10^{2}$
f	$3.48025117 \cdot 10^{-3}$	$5.57513398 \cdot 10^{-3}$

Table 2: Parameters for the Lorentzian EF for two frequencies [7].

2.3 Derivation of Non-Hysteresis Everett Functions

A non-hysteresis behaviour of a material means that the history of a arbitrary input sequence does not affect the resulting output value. The generation of a non-hysteresis EF is needed for the verification scheme in Fig. 1.1. With this step, it is possible to verify simulations using the Preisach model against nonlinear models without hysteresis.

Considering a non-hysteresis input-output relation, the input sequence $H_{in,1} = [-H_{max}, H_2, H_1]$, with $H_2 > H_1$, would result in the same output value $B(H_1)$ as the input sequence $H_{in,2} = [-H_{max}, H_1]$. Fig. 2.11 illustrates the Preisach planes for the described input sequences. The blue areas outline all hysterons in the positive state.
The resulting output value B using (2.9) yields

$$B(H_1) = -B_{max} + E(H_2, -H_{max}) - E(H_2, H_1) \tag{2.17}$$

for the first input sequence $H_{in,1}$ and

$$B(H_1) = -B_{max} + E(H_1, -H_{max}) - E(H_1, H_1) \tag{2.18}$$

for the second input sequence $H_{in,2}$. With the requirement for EF that $E(H, H) = 0$ for all independent $H \in [-H_{max}, H_{max}]$, (2.18) can be rewritten as

$$B(H_1) = -B_{max} + E(H_1, -H_{max}). \tag{2.19}$$

Since the output B of the SPM should be equivalent to the nonlinear relation $B(H) = \mu(H)H$, (2.19) yields

$$E(H, -H_{max}) = B_{max} + \mu(H)H \\ = B_{max} + B(H) \tag{2.20}$$

for all $H \in [-H_{max}, H_{max}]$.
Using (2.20), (2.17) is equivalent to

$$B(H_1) = -B_{max} + B_{max} + B(H_2) - E(H_2, H_1) \tag{2.21}$$

and further yields

$$E(\alpha, \beta) = B(\alpha) - B(\beta), \tag{2.22}$$

which defines the values of the entire EF. The function $B(H)$ has to fulfil $B(H_{max}) = B_{max}$ and $B(-H_{max}) = -B_{max}$. The function could for instance be based on the initial magnetisation curve of a material.

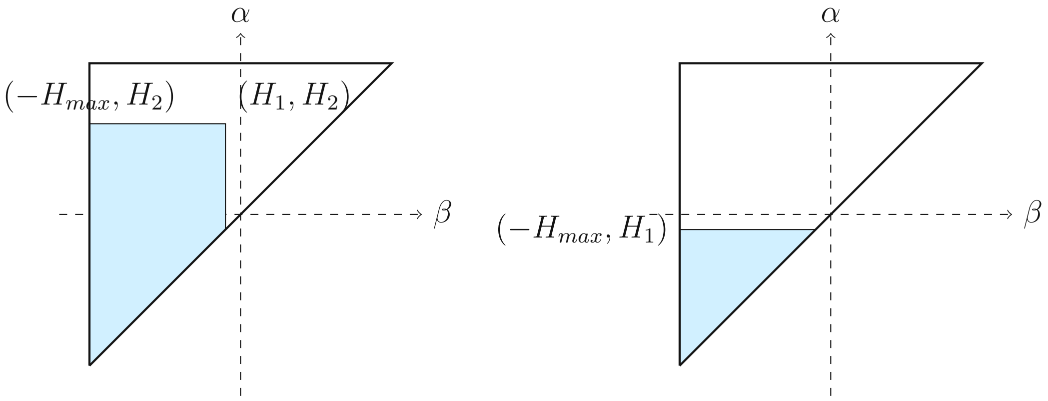

Figure 2.11: Two different input sequences in the Preisach plane with the same final input H_1 but with a different history.

2.4 Discretisation of the Preisach Plane T_{max}

One reason for the discretisation of the Preisach plane T_{max} (2.1) is that the evaluation of the analytic function might be time-demanding. A second reason is that the discretisation can be interpreted as an approximated consideration of the Barkhausen effect [8, p. 424]. Another reason is that by applying the discretisation to the Preisach plane, a computation time speed-up for the calculation of the SPM can be achieved. With the discretisation, the number of possible input values H turns out to be finite. This fact allows to speed up the SPM by reducing the number of values to be checked for finding the necessary minima and maxima. However, the discretisation results in a loss in accuracy. Additionally, the discretisation allows a worst-case assumption for the required memory for a SPM and for the required memory for the pre-computation of the values of an EF.

In the following, different discretisation schemes will be presented. The fundamental idea for the different approaches is that in areas where the gradient (2.10) of the EF has higher values, more grid points in the Preisach plane will yield a higher resolution of the Preisach model. For the discretisation of the Preisach plane, the α-axis and the β-axis are discretised in the same way. Since the discretisation of an axis means a discretisation of the input value, the different discretisation schemes are examined as discretisation of the input value H.
A comparison of the different discretisation schemes is shown in Fig. 2.17, which depicts the resulting

output value of a SPM after demagnetisation.

2.4.1 Linear Discretisation

The straight-forward approach for a discretisation of the input values is to subdivide the input range $[-H_{max}, H_{max}]$ in N_A parts evenly. This results in a constant step size of

$$\Delta H = \frac{2H_{max}}{N_A}, \tag{2.23}$$

which yields the discrete input value

$$H_{D,lin}(H) = H - (H \% \Delta H), \tag{2.24}$$

where $\%$ represents the modulo operator. Additionally, this approach allows a fast computation of indices, which are needed to access the values stored in a two-dimensional Everett matrix $E \in \mathbb{R}^{N_A \times N_A}$. The index for a maximum $M \in [-H_{max}, H_{max}]$ is calculated by

$$r = \left\lceil \frac{H_{max} - M}{\Delta H} \right\rceil \tag{2.25}$$

and analogously

$$c = \left\lfloor \frac{H_{max} + m}{\Delta H} \right\rfloor \tag{2.26}$$

for a minimum $m \in [-H_{max}, H_{max}]$. Thereby, the operators $\lceil \cdot \rceil$ and $\lfloor \cdot \rfloor$ for the ceiling and the floor operation are used.

This discretisation is useful for smooth EF, where the gradient (2.10) is not expected to have high values.

2.4.2 Polynomial Discretisation

In fact, the linear discretisation is a special case of a polynomial discretisation with $p = 1$. Considering the linear discretisation function $H_{D,lin}$,

$$H_{D,poly}(H) = H_{max} \left| \frac{H_{D,lin}(H)}{H_{max}} \right|^p \frac{H}{|H|} \tag{2.27}$$

describes a polynomial discretisation function.

2.4.3 Sine-Cosine Discretisation

The analysis of different material hysteresis shows that the highest values in the gradient (2.10) are to be expected close to the origin of the Preisach plane. Hence, a higher density of discrete input values in that region will induce smaller output step sizes. This will result in smoother and more precise output sequences. The discretisation will generate the highest density around the point $(-H_0, H_0)$. The discretisation function

$$H_{D,sin-cos}(H) = \begin{cases} (H_{max} - H_0) sin\left(\frac{H_{D,lin}(H) - H_{max}}{H_{max} - H_0} \frac{\pi}{2}\right) + H_{max} & H \geq H_0 \\ (H_0 + H_{max}) cos\left(\frac{H_{D,lin}(H) - H_0}{H_0 + H_{max}} \frac{\pi}{2}\right) - H_{max} & H \leq H_0 \end{cases} \tag{2.28}$$

is based on a sine and a cosine, which are linked continuously and monotonically . The value H_0 has to be in the interval $[-H_{max}, H_{max}]$.

2.4.4 Adaptive Discretisation

An adaptive discretisation uses information of the EF to estimate a distribution of points in the interval $[-H_{max}, H_{max}]$, which is denser in areas with high gradients (2.10) of the EF. A straight-forward approach is to derive the information from the major hysteresis loop. The functions

$$f_n(H), f_p(H) : [-H_{max}, H_{max}] \rightarrow [-B_{max}, B_{max}] \tag{2.29}$$

represent the negative and the positive branch of the major loop. Hence, the function

$$f_{pn}(H) = \frac{H_{max}}{2B_{max}}\big(f_p(H) + f_n(H)\big) \tag{2.30}$$

yields an easy-to-implement approximation of the scaled initial magnetisation curve. Further, the function

$$H_{D,adaptive}(H) = f_{pn}(H_D(H)) \tag{2.31}$$

can be used as discretisation function. Thereby the adaptive discretisation function $H_{D,adaptive}$ uses a different discretisation function H_D in the first step. This function H_D could for instance be the linear discretisation function (2.24) or the sin-cos discretisation (2.28). Since the major loop differs for different materials, this discretisation varies according to the material.

Fig. 2.12 illustrates the step size between two discrete values of all described discretisation algorithms. For the linear version, the step size is constant. For the other versions, the step size gets smaller, as H gets closer to the point where the EF varies the most.

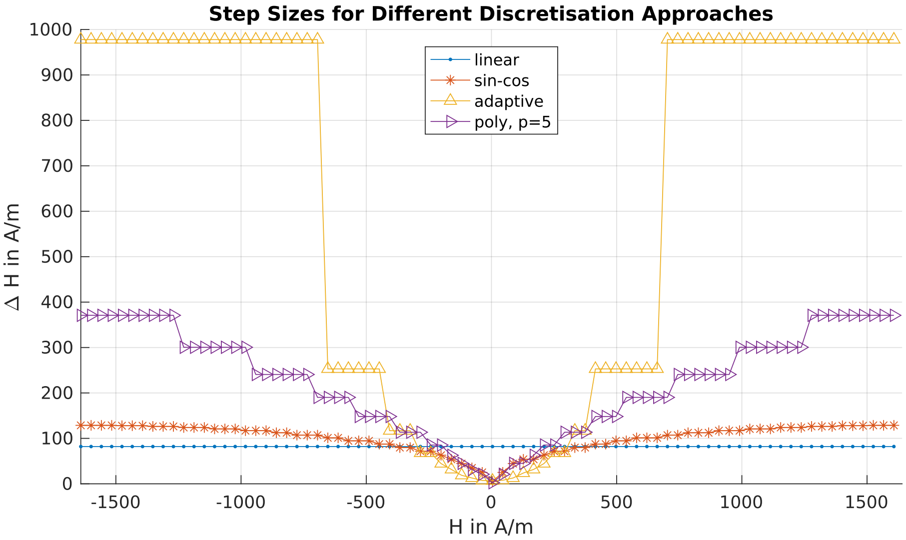

Figure 2.12: Step sizes for different discretisation approaches.

2.5 Hysteretic Energy Losses

The magnetic losses in ferromagnetic materials are called hysteretic energy losses [1, p. 44]. A variation in the input signal switches the according hysterons in the Preisach plane. Figure 2.13 shows the switched hysterons Ω_H of an arbitrary input signal variation. The according hysteretic losses can be calculated by

$$Q = \iint_{\Omega_H} \mu(\alpha, \beta)(\alpha - \beta)\, d\alpha\, d\beta \tag{2.32}$$

and respect the material via its Preisach function $\mu(\alpha, \beta)$.

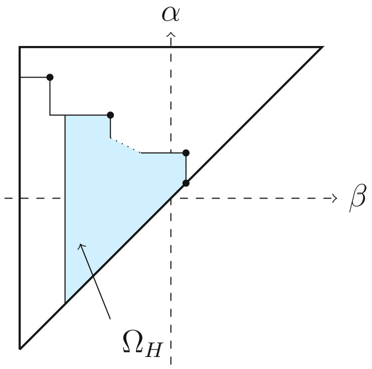

Figure 2.13: Staircase line in the Preisach plane with highlighted set Ω_H where the sate of some hysterons has changed.

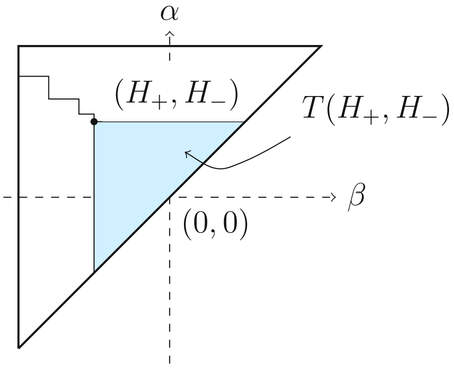

Figure 2.14: Triangle $T(H_+, H_-)$ in the Preisach plane.

An input sequence increasing from a value H_- up to the value H_+, which results in a triangular set, is shown in Fig. 2.14. The according energy loss, based on (2.32), yields

$$Q(H_+, H_-) = \iint_{T(H_+,H_-)} \mu(\alpha, \beta)(\alpha - \beta)\, d\alpha d\beta. \tag{2.33}$$

Under consideration of the EF in (2.7) this equation simplifies to

$$Q(H_+, H_-) = (H_+ - H_-)E(H_+, H_-) - \int_{H_-}^{H_+} E(H_+, \beta)\, d\beta - \int_{H_-}^{H_+} E(\alpha, H_-)\, d\alpha. \tag{2.34}$$

Finally, the hysteretic energy losses for an input variation are given by calculating the difference of

$$Q(t) = Q(M_N, m_N) + \sum_{k=1}^{N} Q(M_{N-k}, m_{N-k}) - Q(M_{N-k}, m_{N-k-1}), \tag{2.35}$$

before and after the input variation where N represents the number of minima [1, p. 55].

2.6 Demagnetisation

The demagnetisation process of a ferromagnetic material is an essential requirement to set the material in a defined state before starting an experiment.
In general, magnetised material can be demagnetised in three different ways: by exposing it to mechanical stress, to high temperatures or to alternating and decreasing magnetic fields [8].
Since it is not possible to apply the first two approaches to the Preisach model, an alternating and decreasing input signal is used.

2.6.1 Discrete Demagnetisation

Considering the fact that only past minima and maxima influence the state of the Preisach model, the input signal can be reduced to minima m_k and maxima M_k. This input sequence is then resulting in minima and maxima forming the staircase line in the Preisach plane. Due to the discretised EF, all minima and maxima are discrete values. Moreover, the best solution - in terms of remaining magnetisation - for demagnetising a discrete EF can be achieved by using all values in the diagonal of the Preisach plane ($\alpha = -\beta$) as staircase line. To this end, the minimal input sequence is of length N_A resulting in

$$N_{corner} = \left\lfloor \frac{N_A}{2} \right\rfloor \tag{2.36}$$

corners. For the linear discretisation of the Preisach plane T_{max} with a constant step size ΔH,

$$\begin{aligned} H_{demag} = [-H_{max}, & H_{max} - \Delta H, -H_{max} + \Delta H, \\ & H_{max} - 2\Delta H, -H_{max} + 2\Delta H, \\ & \ldots, \Delta H, -\Delta H, 0] \end{aligned} \tag{2.37}$$

forms the input sequence for demagnetisation. In fact, the sequence is valid for all discretisation schemes, if ΔH is interpreted as the local step size.

2.6.2 Continuous Demagnetisation

For an improvement of the remaining magnetisation, a finer demagnetisation can be performed. To achieve this, an arbitrary decreasing alternating continuous input signal is applied to the model. Further, the output value is calculated by using the analytic or the interpolated EF, see Section 2.10.1. After the demagnetisation, the model can be used as a discretised model again, since the intermediate output values are stored in the cumulative sum.

2.6.3 Perfect Demagnetisation

An issue with the formulation for the calculation of the output value of the SPM in (2.9) is that in order to initialise a magnetic material in its demagnetised state, with $B = 0$ and $H = 0$, an infinite number of minima m_k and maxima M_k is needed [6]. The previously described approaches use an finite number of minima and maxima and approximate the demagnetised state, which is not just inaccurate but also costly in terms of computation time and memory demand. A solution for this issue is to use the value

$$H_{max,in}(t) = \max_{t' \in [0,t]} |H(t')|, \tag{2.38}$$

which reflects the maximum of all applied input values. Further, the adaption of (2.9) for the calculation of the output value B of the SPM

$$\begin{aligned} B(t) = & - B_{max} + \frac{1}{2}\big(E(H_{max}, -H_{max}) - E(H_{max,in}, -H_{max,in})\big) \\ & + \sum_{k=0}^{N-1} \Big[E(M_k, m_{k-1}) - E(M_k, m_k)\Big], \end{aligned} \tag{2.39}$$

$$= -\frac{1}{2}E(H_{max,in}, -H_{max,in}) + \sum_{k=0}^{N-1} \Big[E(M_k, m_{k-1}) - E(M_k, m_k)\Big] \tag{2.40}$$

where $m_{-1} = -H_{max,in}$, is used. With this approach, the magnetisation is identically zero in the initial state ($H(t_0) = 0$ and $H_{max,in}(t_0) = 0$). For the input signal displayed in Fig. 2.15 the value $H_{max,in}$ is 1000A/m. The corresponding Preisach plane T_{max} with a saturation value $H_{max} = 1640$A/m is shown in Fig. 2.16. Additionally, the remaining part of the perfect demagnetisation is highlighted in red.

The downside of the perfect demagnetisation is that the value $H_{max,in}$ has to be recalculated in every step. Additionally, the approach is only feasible for symmetrically discretised Preisach planes.

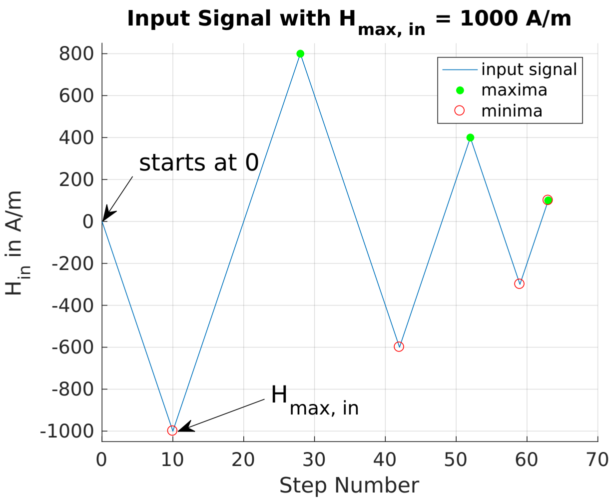

Figure 2.15: Input signal with $H_{max,in} = 1000A/m$.

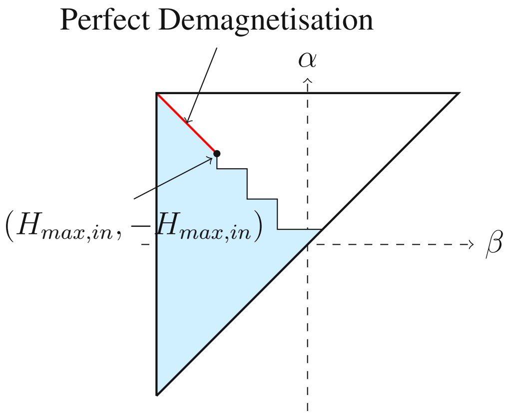

Figure 2.16: Staircase line in the Preisach plane with perfect demagnetisation.

2.7 State of Demagnetisation as Quality Measure

The measured absolute output value of the SPM after applying a discrete demagnetisation sequence for the different discretisation schemes is illustrated in Fig. 2.17. Since the ideal state of demagnetisation would be $B_{demag} = 0$, a lower output value reflects a better accuracy of the model when the same discretisation level N_A is compared. Moreover, Fig. 2.17 shows that the lowest output values after the demagnetisation process are achieved by using the adaptive discretisation, see Section 2.4.4.

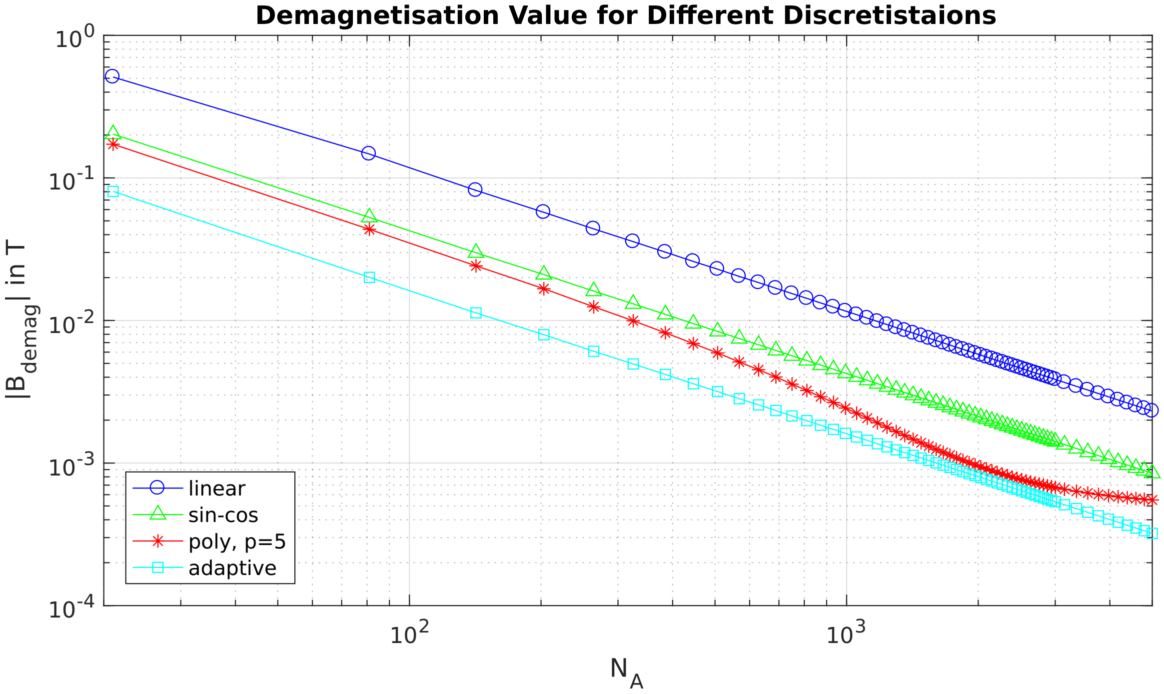

Figure 2.17: Output value $|B_{demag}|$ after the discrete demagnetisation process for different discretisation schemes in respect to the number N_A of discretisation points in one axis.

The state of discrete demagnetisation indicates the worst case in terms of memory. For an ideally demagnetised material, an infinitely long input sequence is needed. Since this case is not feasible, a trade-off between accuracy, memory demand and computation time has to be found.

2.8 Derivation of the Initial Magnetisation Curve

For the comparison with a nonlinear model the initial magnetisation curve $B_{KL}(H)$ of a material is needed. Since the initial state of the material is demagnetised, the maximal input value (2.38) $H_{max,in} = 0$. For the calculation of the initial magnetisation curve, the magnetic field strength H is consequently increased. Therefore, the maximal input $H_{max,in}$ always equals the current magnetic field strength H. Under consideration of (2.40), the value

$$B_{KL}(H) = -\frac{1}{2}E(H,-H) + E(H,-H) - E(H,H) \tag{2.41a}$$

$$= \frac{1}{2}E(H,-H) \tag{2.41b}$$

represents the magnetic flux density on the initial magnetisation curve resulting from the magnetic field strength H.

2.9 Material Parameters

For the simulation of magnetic hysteresis behaviour, the material relation between the magnetic flux density B and the magnetic field strength H is of interest. The material relation is defined by the magnetic permeability or the differential permeability.

2.9.1 Magnetic Permeability μ

In a ferromagnetic material with its material relation

$$\mu = \frac{B}{H}, \tag{2.42}$$

the permeability μ is not defined in the case of remanence, since $H = 0$. In this case, the relation $B = \mu H$ does not hold, although B is well defined as output of the Preisach model. Therefore, the absolute permeability μ cannot be used for solving electromagnetic field problems, which take into account hysteresis phenomenon.

The permeability μ for an input signal, which generates an initial magnetisation curve followed by the major loop is shown in Fig. 2.18. Since $H = 0$ at some points, the permeability μ is not defined there. An interesting point to mention is that the permeability can be negative, which is unique for hysteresis behaviour.

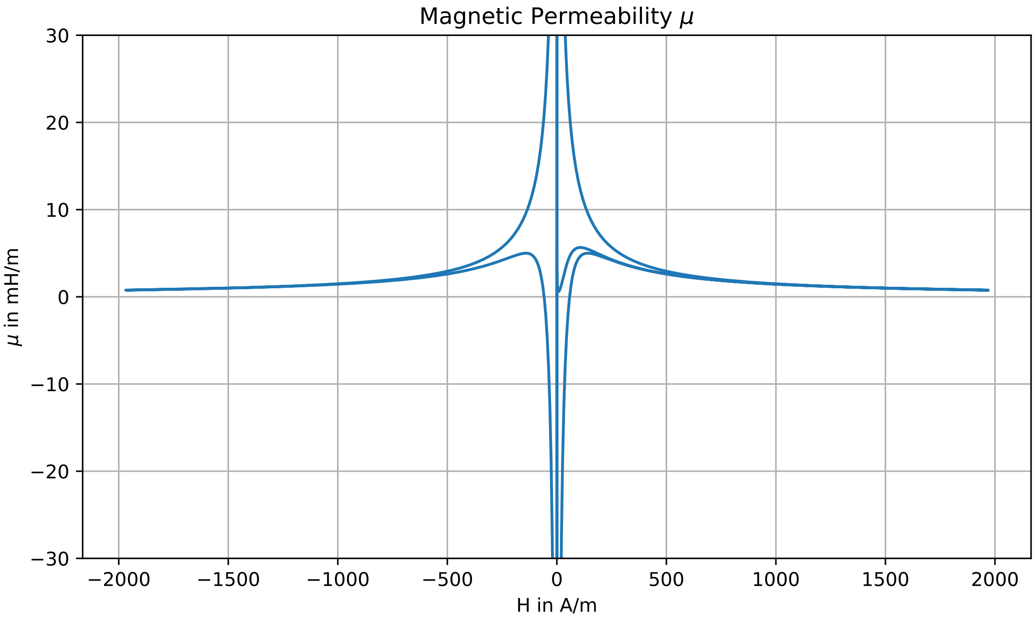

Figure 2.18: Magnetic permeability μ for an initial magnetisation curve followed by the major loop. It is not defined for zero-crossings of H and is zero when of B vanishes.

2.9.2 Magnetic Differential Permeability μ^{Δ}

The advantage of the differential permeability $\mu^{\partial} = \frac{\partial B}{\partial H}$ is that it is defined in any case. The differential permeability can be approximated by

$$\mu^{\partial} \approx \mu^{\Delta} = \frac{B^{k+1} - B^{k}}{H^{k+1} - H^{k}}. \tag{2.43}$$

which uses a stored input-output pair (H^k, B^k), which is different from the current input-output pair (H^{k+1}, B^{k+1}). However, the approach is inaccurate, especially when

$$|H^{k+1} - H^{k}| > \Delta H \tag{2.44}$$

holds. Thereby, ΔH describes the current local step size, which might be different for $H^{k+1} > H^k$ and $H^{k+1} < H^k$.

For a more accurate approximation of the differential permeability μ^{Δ}, this local step size can be considered, yielding

$$\mu^{\Delta} = \frac{B^{k+1} - B(H^{k+1} \pm \Delta H)}{\Delta H}. \tag{2.45}$$

For decreasing input sequences the minus and for increasing the plus symbol apply.

The approximation of the differential magnetic permeability μ^{Δ} shown in Fig. 2.18 is formed by an input signal, which generates the initial magnetisation curve followed by the major loop. The differential permeability is always greater than zero.

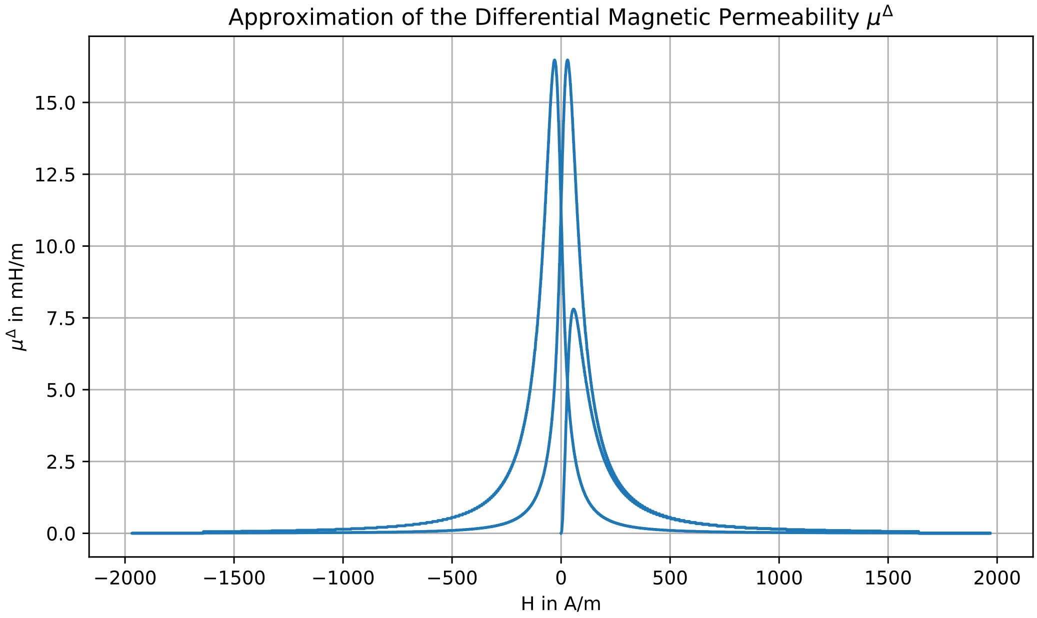

Figure 2.19: Approximation of the differential magnetic permeability μ^Δ for an initial magnetisation curve followed by the major loop. It is always greater than zero.

2.10 Optimising the Computational Costs

In this section, two methods are shown which reduce the computational costs of the SPM tremendously. Both approaches are based on the discretised Preisach plane T_{max}, see Section 2.4. The first approach interpolates values of the EF based on the pre-computed root points of the discretised Preisach plane. The second approach calculates an output value B_D which is based on the discretised inputs value $H_D(H)$ and approximates the output value B in a post-processing step.

2.10.1 Efficient Evaluation of the Everett Function

The combination of the discrete evaluation of the EF with an interpolation deals with the downside of the loss in accuracy. In order to compute an interpolation, stored discrete values are used. Like illustrated in Fig. 2.20, four points are used in general. This leads to a bilinear interpolation. However, for points in areas where only three adjacent values are available, a linear interpolation is taken into account.

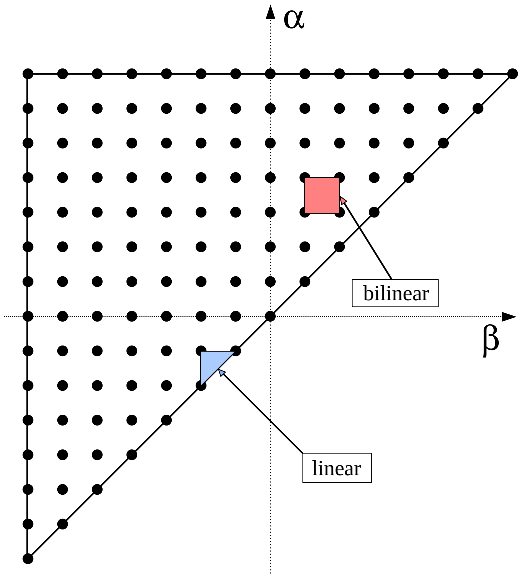

Figure 2.20: Interpolation types within the discretised Preisach plane T_{max}.

The bilinear interpolation

$$E(\alpha, \beta) = a\alpha + b\beta + c\,\alpha\beta + d \tag{2.46}$$

with (a, b, c, d) as unknown coefficients and the linear interpolation

$$E(\alpha, \beta) = a\alpha + b\beta + c, \tag{2.47}$$

with (a, b, c) as unknown coefficients, describe the equations for the approximation of the EF. For the identification of the coefficients, a 4×4 or a 3×3 matrix has to be inverted. Since the implementation should be efficient, a normalised version is used.
The normalised input values are

$$\alpha' = \frac{\alpha - \alpha_D}{\Delta H} \in [0, 1] \text{ and } \beta' = \frac{\beta - \beta_D}{\Delta H} \in [0, 1], \tag{2.48}$$

where $\alpha_D = H_D(\alpha)$ and $\beta_D = H_D(\beta)$ are discretised values, see Section 2.4, and ΔH is the according step size. With the normalised input values and the coefficients

$$a = E(\alpha_D + \Delta H, \beta_D) - E(\alpha_D, \beta_D) \tag{2.49a}$$
$$b = E(\alpha_D, \beta_D + \Delta H) - E(\alpha_D, \beta_D) \tag{2.49b}$$
$$c = E(\alpha_D, \beta_D) - E(\alpha_D + \Delta H, \beta_D) - E(\alpha_D, \beta_D + \Delta H) + E(\alpha_D + \Delta H, \beta_D + \Delta H) \tag{2.49c}$$
$$d = E(\alpha_D, \beta_D), \tag{2.49d}$$

the bilinear interpolation is

$$E(\alpha, \beta) = a\alpha' + b\beta' + c\,\alpha'\beta' + d, \tag{2.50}$$

in case of four adjacent points. If only three adjacent points are available, the linear interpolation

$$E(\alpha, \beta) = a\alpha' + b\beta' + c \tag{2.51}$$

with the coefficients

$$
\begin{aligned}
a =& E(\alpha_D + \Delta H, \beta_D + \Delta H) - E(\alpha_D, \beta_D + \Delta H) && \text{(2.52a)}\\
b =& E(\alpha_D, \beta_D + \Delta H) - E(\alpha_D, \beta_D) && \text{(2.52b)}\\
c =& E(\alpha_D, \beta_D), && \text{(2.52c)}
\end{aligned}
$$

is applied.

The benefit of the normalised interpolation is that no matrix inversion has to be done. Consequently, the evaluation of the interpolated EF instead of the analytic EF decreases the computational costs without a huge loss in accuracy.

2.10.2 Interpolation of Resulting B-Value

A SPM with a discrete EF generates a discrete output value B_D. This value corresponds to a discrete input value H_D, which is the discrete value of the input value H. With the introduced approximation of the differential permeability μ^{Δ}, an interpolated B value

$$B(H) = B_D + \mu^{\Delta}(H - H_D) \tag{2.53}$$

can be computed.

Interpolated Turns The interpolated value B is based on the current approximation of the differential permeability μ^{Δ}. In the case that the input sequence changes from increasing to decreasing (or vice versa), the differential permeability jumps.
This process is sketched in Fig. 2.21. Starting from point `A`, the interpolation works fine until `B` is reached. At this point, the input signal changes from a decreasing to an increasing input signal, causing the differential permeability to jump. Further, the interpolated value jumps from the old (decreasing) branch to point `C` on the future (increasing) branch. The analogous issue appears at point `D` with a change from an increasing to a decreasing input sequence. The issue of the interpolated turns, shown in Fig. 2.21, is exaggerated by using a small number of discretisation steps N_A.

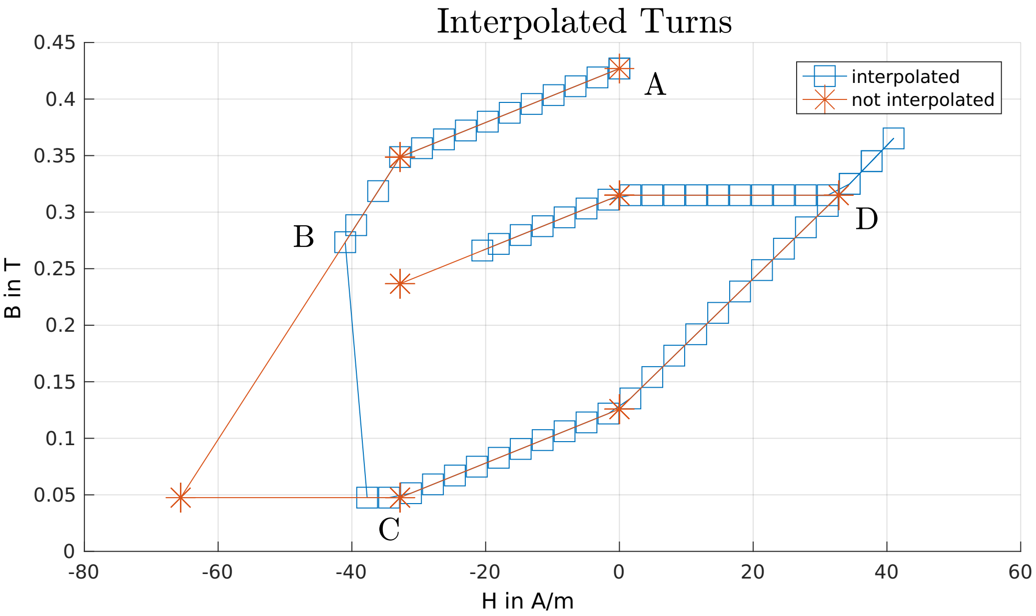

Figure 2.21: The jumping output value when the grade of the input changes.

2.11 Inverse Mode of the Preisach Model

For the inverse mode of the scalar Preisach model (iSPM), an input value $\tilde{H}$ has to be found so that the output value of the SPM B' fits the known value B.
Finding the optimal H can be delegated to a search algorithm. However, probing a specific H value directly would influence the history of the model. Hence, the model has to be copied in each iteration, which is memory- and time-demanding.
The error $|B - B'|$ can be used as a quality measure. Further, this measure can be used as stop criteria for the search algorithm.

2.12 Benchmarking the Forward Mode of the Preisach Model

To find an objective measure for the quality of an implemented Preisach model, a benchmark has to be defined. To this end, a standardised input sequence is specified. The constant step size of the input sequence is set to

$$H_{step} = \frac{H_{max}}{N_{steps} - 1}, \tag{2.54}$$

where N_{steps} defines the number of equally-spaced steps.
The material is demagnetised with an alternating input sequence, whose amplitude decreases by H_{step} in each period. Afterwards, the input sequence is increased to the maximum value of the model H_{max}. Finally, the major hysteresis loop is calculated.
Hence, the input sequence consists of 4 subsequences

- the demagnetisation sequence

$$\begin{aligned} H_{demag} = [-H_{max}, H_{max}, &- H_{max} + H_{step}, H_{max} - H_{step}, \\ &- H_{max} + 2H_{step}, H_{max} - 2H_{step}, \\ &\dots, -H_{step}, H_{step}, 0], \end{aligned} \tag{2.55}$$

  which includes the reset to a defined initial state - negative saturation - in the beginning,

- the initial magnetisation curve

$$H_{initMag} = [H_{step}, 2H_{step}, 3H_{step}, \dots, H_{max}] \tag{2.56}$$

- the decreasing part of the major loop

$$H_{major,dec} = [H_{max}, H_{max} - H_{step}, H_{max} - 2H_{step}, \dots, -H_{max}] \tag{2.57}$$

  and finally

- the increasing part of the major loop

$$H_{major,inc} = [-H_{max}, -H_{max} + H_{step}, -H_{max} + 2H_{step}, \dots, H_{max}]. \tag{2.58}$$

A model under test has to compute the magnetic flux density B, the permeability μ, and the differential permeability μ^{Δ} in every instant.
The value B_{demag} after the demagnetisation indicates a measure for the quality of the model, whereas the running time t_{sim} indicates a measure for the computational costs. An estimation of the memory complexity is done in Section 2.15.
The optimal solution for B_{demag} would be zero, however this would require an infinitesimal step size H_{step}. Hence, the number of steps is defined as $N_{steps} = 5,001$, which results in approximately

$7N_{steps} \approx 35,000$ input values. The EF for the benchmark is based on arctangent functions, see Section 2.2.2.

With the slowest model as reference model, a speed-up measure $\frac{t_{ref}}{t_{sim}}$ is introduced. The first and slowest model is the straight-forward implementation of the classical SPM suggested by Mayergoyz [1, p. 32]. The other implementations are results of different iterations in the development cycle. The differences are based on

- different search algorithms to find a discrete value,
- different search algorithms to find minima and maxima and
- using or not using the cumulative sum.

Besides showing the calculated speed-up, Table 3 summarises the differences. The implementations from number one to eight calculate the interpolated output value, see Section 2.10.2, in a post-processing step. The last implementation (number eight) achieves a speed-up of about 175. The SPM which is based on the optimisation approach which interpolates the EF directly results in a speed-up of about 14, see Section 2.10.1.

#	Discretisation Type	Approach to Calculate B	Search Algorithm to Find Min/Max	Speed-Up
1.	linear	standard	linear	1
2.	sin-cos	standard	linear	1.3
3.	linear	standard	linear	3.9
4.	sin-cos	standard	linear	5.4
5.	sin-cos	cumulative sum	linear	17.4
6.	adaptive	cumulative sum	linear	42.9
7.	adaptive	cumulative sum	binary	77.4
8.	adaptive	cumulative sum	binary	174.7
interp.	adaptive			14.06

Table 3: Speed-up of different implementations of SPMs.

The measured running times with respect to the number of discretisation steps N_A are depicted in Fig. 2.22. The calculated running time does not include the pre-computation of the EF values. To this end, Fig. 2.22 shows that the latest implementation is the fastest implementation regardless of the number of discretisation steps.

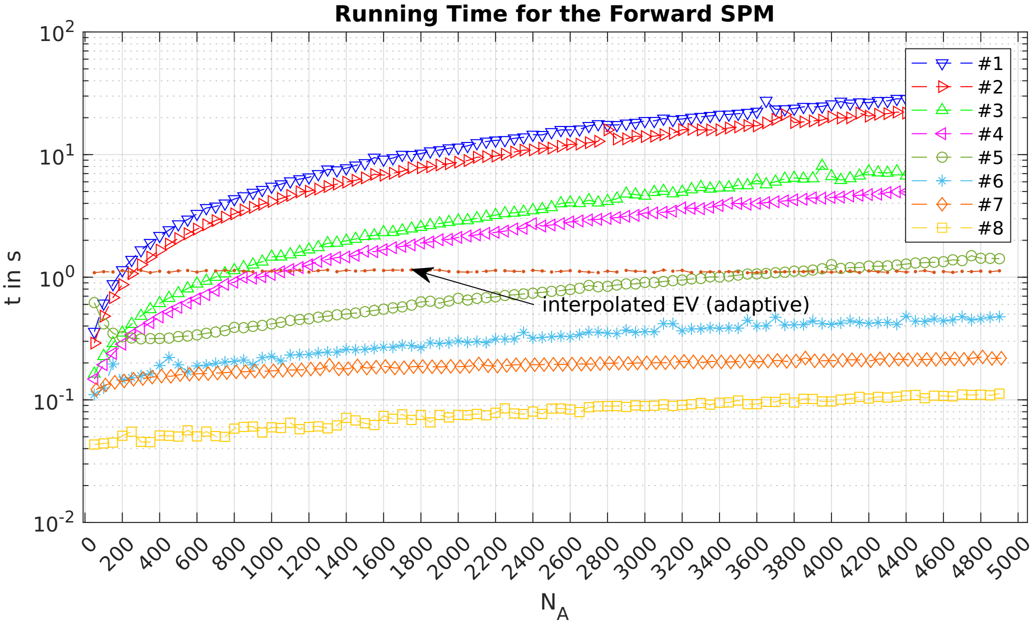

Figure 2.22: Running times of different different implementations of the SPM.

The value B_{demag} after the demagnetisation sequence (2.55) depends solely on the used discretisation scheme for the Preisach plane T_{max}. Therefore, the result does not differ for implementations of different development cycles. Fig. 2.23 illustrates the value after the defined demagnetisation sequence for the different discretisation schemes. Additionally to the values resulting from the post-processing interpolation of the output values, the value resulting from an interpolated EF is shown. The step size ΔH in the nonlinear discretisation approaches is not constant. Hence, the step size of the input sequence might get greater than the local step size of the discretisation approaches. Consequently, this issue causes the resulting value B_{demag} to increase again. Decreasing the number of steps N_{steps} of the input sequence would result in peaks located at lower discretisation levels N_A. For SPMs which are based on interpolated EFs, see Section 2.10.1, the number of discretisation steps N_A does not significantly influence the output value B_{demag} after the demagnetisation sequence (2.55). However, the selected discretisation scheme does have an influence. The according output values are summarised in Table 4.

Discretisation Scheme	B_{demag} in mT
linear	1.376
sin-cos	0.277
poly	-2.479
adaptive	1.439

Table 4: Output value after applying the demagnetisation sequence to a SPM with an interpolated EF.

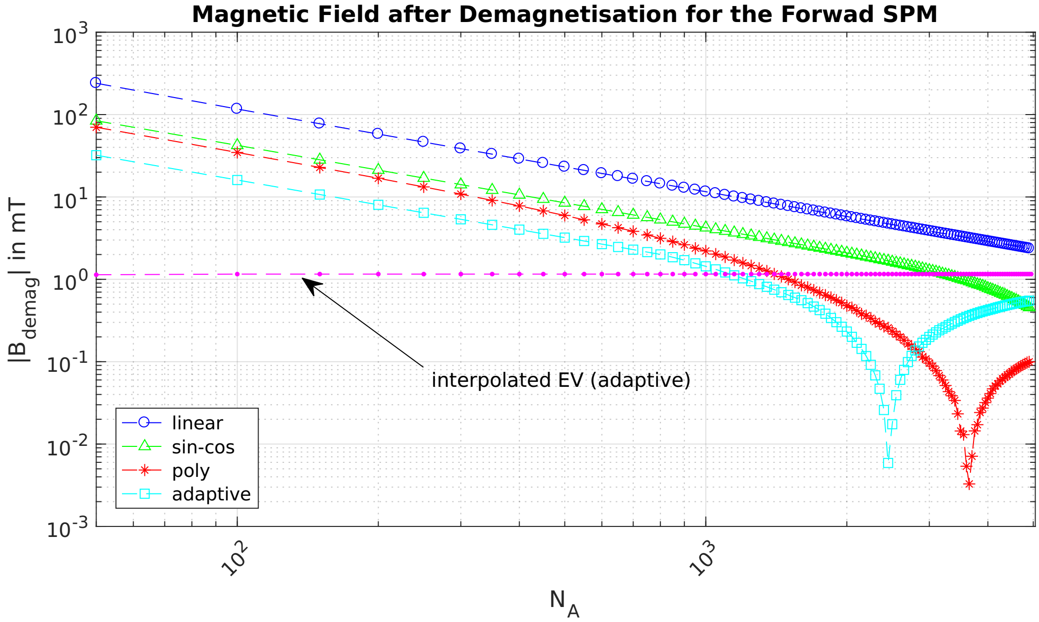

Figure 2.23: Output values B_{demag} for different discretisation schemes.

2.13 Benchmarking the Inverse Mode of the Preisach Model

Analogously to the benchmark for the forward Preisach model, see Section 2.12, the benchmark for the iSPM shall allow a fair comparison of various implementations. Consequently, a step size

$$B_{step} = \frac{B_{max}}{N_{steps} - 1} \tag{2.59}$$

is selected and the sequence

$$\begin{aligned} B_i = [\quad & -B_{max}, B_{max}, -B_{max} + B_{step}, B_{max} - B_{step}, \ldots, -B_{step}, B_{step}, 0, \\ & B_{step}, 2B_{step}, \ldots, B_{max} - B_{step}, B_{max}, \\ & B_{max} - B_{step} \ldots, -B_{max} + B_{step}, -B_{max}, \\ & -B_{max} + B_{step} \ldots, B_{max} - B_{step}, B_{max} \quad] \end{aligned} \tag{2.60}$$

is defined. With $N_{steps} = 1,001$, the number of steps in the input sequence is approximately $7N_{steps} \approx 7,000$. The reduced number of steps compared to the benchmark for the forward mode of the SPM takes into account that the iSPM is more time-demanding. Analogously to the comparison of the forward model,

- different discretisation schemes for the Preisach plane,
- different approaches for the calculation of the output value,
- different search algorithms for the discretisation of an input value,
- different search algorithms for finding minima and maxima and
- different search algorithms for fitting the input value

are compared in terms of accuracy and computational costs. The computation times for applying the input sequence to different implementations are shown in Table 5. Beside that, the calculated speed up is shown. Compared to the maximal speed-up of the forward SPM, the maximal speed-up of 32.23 in the iSPM is smaller. The iSPM, which is based on a interpolated EF, see Section 2.10.1, achieves a speed-up of 15.68 which is approximately 2 times slower than the iSPM which uses the post-processing interpolation.

#	Discretisation Type	Search Alg. to Find $\tilde{H}$	Approach to Calculate B	Search Algorithm to Find Min/Max	Speed-Up
1.	linear	linear	standard	linear	1
2.	sin-cos	linear	standard	linear	0.5
3.	linear	binary	standard	linear	5.5
4.	sin-cos	binary	standard	linear	5.4
5.	sin-cos	binary	cumulative sum	linear	19.5
6.	adaptive	binary	cumulative sum	linear	30.15
7.	adaptive	binary	cumulative sum	binary	32.23
interp.	adaptive				15.68

Table 5: Speed-up of different implementations of the iSPM.

The calculated running times, displayed in Fig. 2.24, outline the results presented in Table 5. The last implementation of the iSPM is the fastest. The output value B_{demag} after applying th demagnetisation sequence is illustrated in Fig. 2.25 for four different discretisation schemes.

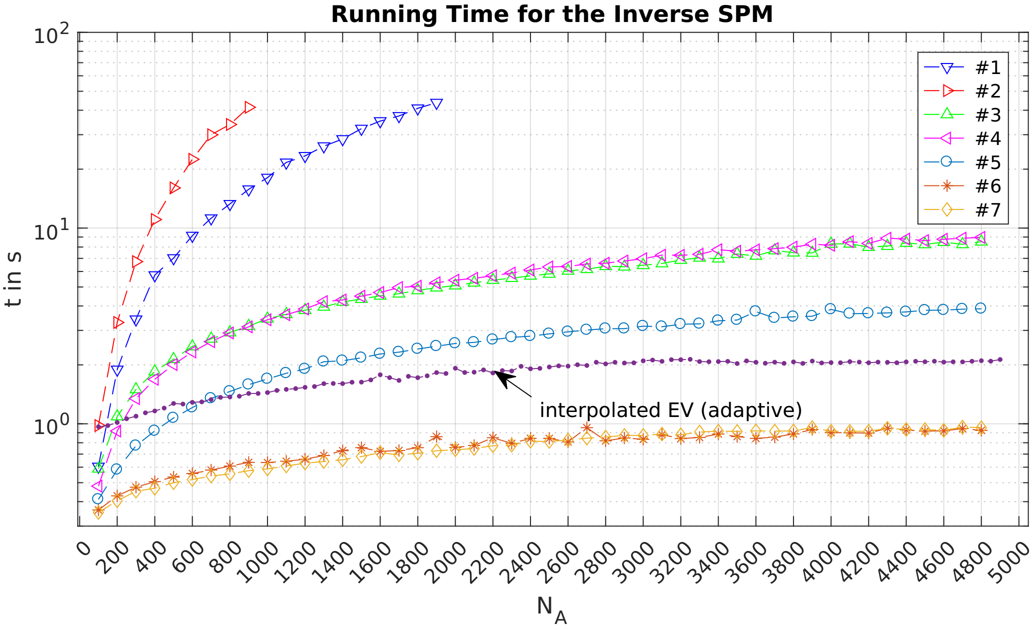

Figure 2.24: Running times of different implementations of the iSPM.

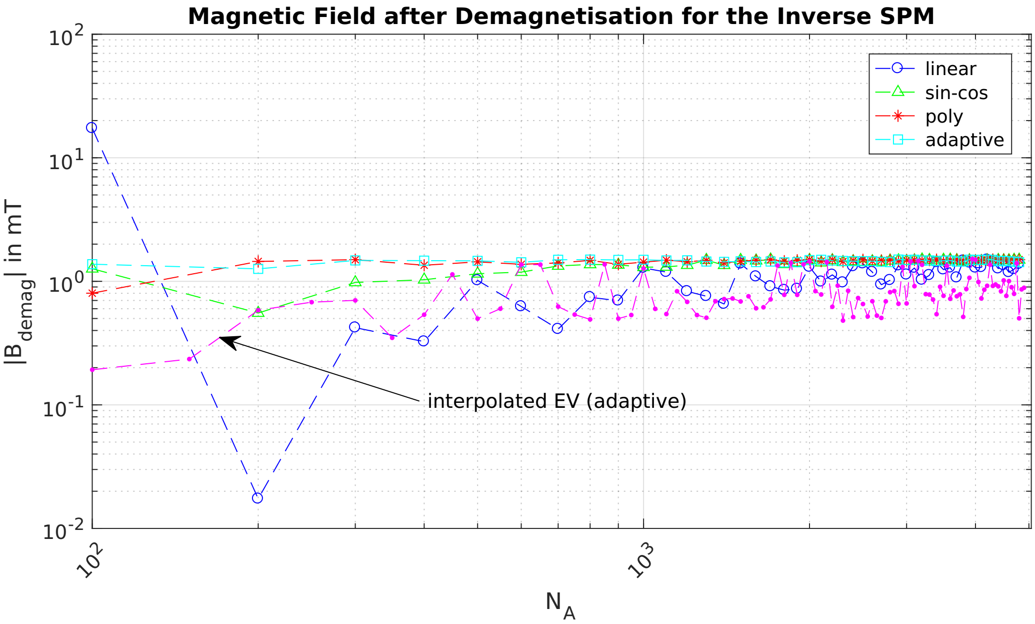

Figure 2.25: Demagnetisation values of the iSPM with different discretisation schemes.

2.14 Energy-Based Verification

To verify the accuracy of the implemented model, a nonlinear reference model is used. For a nonlinear relation between the scalar magnetic field strength H and the scalar magnetic flux density B, the energy density w in the current state is calculated according to

$$w = \int_0^{B(t)} H(B)\, dB \tag{2.61a}$$

$$= B(t)H(t) - \int_0^{H(t)} B(H)\, dH. \tag{2.61b}$$

The transformation in the second step is particularly useful, since the output value of the Preisach model is the flux density B. The graphical interpretation of (2.61a) is illustrated in Fig. 2.26.

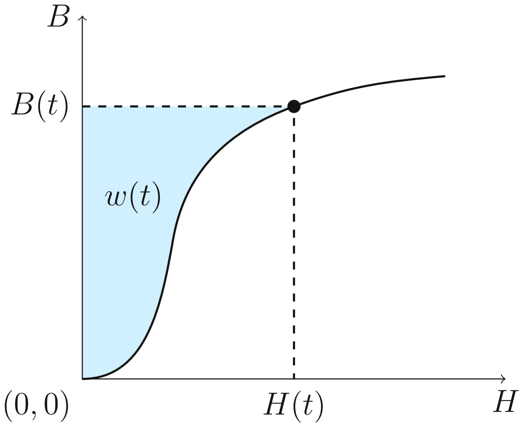

Figure 2.26: Graphical interpretation of the magnetic energy $w(t)$ for nonlinear material relations.

For all verification simulations, the number of discretisation steps for the EF is set to $N_A = 501$. The maximum values for input and output are set to $H_{max} = 1640$A/m and $B_{max} = 1.5$T, respectively. For the verification, the SPM is perfectly demagnetised according to Section 2.6.3. Further, an input sequence of length 125 is used, which results in the initial magnetisation curve followed by the major loop.

Verification without Hysteresis In the first step, a SPM with a bilinear EF, see Section 2.2.1, is verified by a linear model. The energy density of a linear model with a material relation $B = \mu_0\mu_r H = \mu H$ is simply

$$w_{lin}(t) = \frac{B(t)^2}{2\mu}. \tag{2.62}$$

In the second step, a Preisach model without hysteresis , see Section 2.3, is verified by a nonlinear model. The energy density (2.61a) for the nonlinear model is based on the initial magnetisation curve of the SPM.

Verification with Hysteresis Finally, a SPM with hysteresis is verified against a nonlinear model. Since the energy density cannot be compared directly, an energy-based measure

$$\tilde{w} = \frac{BH}{2} \tag{2.63}$$

is used. The comparison is only valid as long as the input sequence is increasing.

In each step of the input sequence the relative error

$$\varepsilon_* = \left|\frac{w_* - w_{ref}}{w_{ref}}\right| 100\% \tag{2.64}$$

is calculated. Thereby, w_* stands either for the energy density function w or the energy-based density function $\tilde{w}$. The reference value w_{ref} is the energy density of either a linear or a nonlinear model.

The resulting relative errors are displayed in Fig. 2.27. The maximum relative error is 2.48% and occurs at the verification against the nonlinear model.

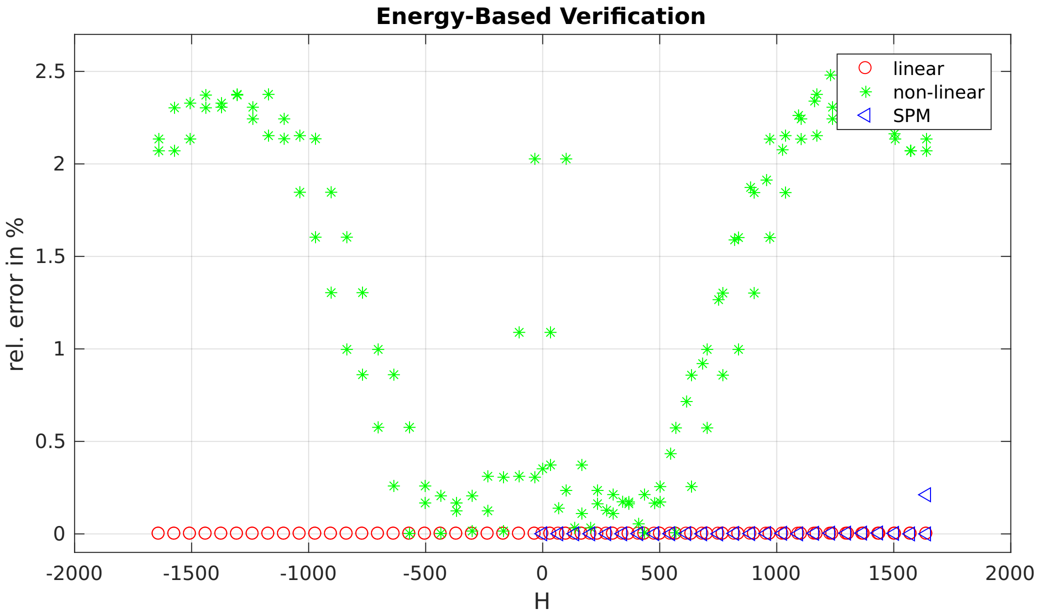

Figure 2.27: Energy and energy-based verification in case of linearity, nonlinearity and hysteresis.

2.15 Estimation of the Complexity

Memory Complexity - Everett Function The number of values needed to be stored for the discrete EF is

$$N_{EV} = \frac{N_A^2 + N_A}{2}, \tag{2.65}$$

which is known as Gauss' sum formula.

Memory Complexity As described in Section 2.6, the highest demand for memory is in the case of discrete demagnetisation, see Section 2.6.1. For a worst-case estimation the number of minima and maxima are considered. Moreover, the cumulative sum, see Section 2.1, stores the subtotals as third value.

Using (2.36) for the number of corners N_{corner} and (2.65) for the number of pre-computed values stored in the Everett matrix N_{EV},

$$N_{total} = N_{EV} + 3N_{corner} \tag{2.66}$$

$$= \frac{N_A^2 + N_A}{2} + 3\left\lfloor \frac{N_A}{2} \right\rfloor \approx \frac{N_A^2 + 4N_A}{2} \tag{2.67}$$

represents a worst-case estimation for the number of values needed to be saved. Consequently, the memory demand is of complexity class $\mathcal{O}(N_A^2)$.

Execution Time Complexity The highest execution time is to be expected in the discretely demagnetised state. It is the state of the most values stored in the cumulative sum. For an update of the model, each element in the cumulative sum has to be checked for whipe-out. Since the cumulative sum is sorted, adequate search algorithms can be applied. The chosen algorithm is the binary search algorithm with the complexity class $\mathcal{O}(\log N_A)$. This complexity class indicates the time complexity class of the Preisach model directly.

2.16 Verification of the Scalar Preisach Model using Netgen/NGSolve

To verify the SPM using Netgen/NGSolve [2], a boundary value problem (BVP) has to be defined, which has a magnetic field pointing into a single direction. A geometry and the according BVP are presented in Section 6. A current I_0 is impressed into a coil, which will result in a magnetic field in a ferromagnetic ring. The magnetic flux density $\mathbf{B}$ is mainly oriented in the direction of the ring.

3 Vector Preisach Model

3.1 Theoretical Description

Modelling vector hysteresis is mainly done using the Stoner-Wohlfart model. This model is based on particles which have a certain equivalent in physics. However, the vector Preisach model (VPM) is becoming more and more popular since it is considered to be mathematically more accurate [1, p. 141].

The ideal VPM is a superposition of an infinite number of scalar Preisach models (SPMs). The SPMs are distributed on the surface of a unit sphere. Hence, each of these SPMs is connected to a direction vector $\mathbf{e}_R$ of length $|\mathbf{e}_R| = 1$. For a vector input signal $\mathbf{H}$, each projection on the according direction $H_R = \mathbf{H} \cdot \mathbf{e}_R$ affects the corresponding SPM. Further, each SPM results in a scalar output value B_R. An integration over the surface of a unit sphere yields the output

$$\mathbf{B}(t) = \int_{\theta=0}^{\pi} \int_{\varphi=0}^{2\pi} \mathbf{e}_R B_R \, d\varphi \, d\theta \tag{3.1}$$

of the VPM. The definition of the SPM (2.2) leads to

$$\begin{aligned}
\mathbf{B}(t) &= \int_{\theta=0}^{\pi} \int_{\varphi=0}^{2\pi} \mathbf{e}_R \hat{\Gamma}[\mathbf{H}(t) \cdot \mathbf{e}_R] d\varphi d\theta && \text{(3.2a)}\\
&= \int_{\theta=0}^{\pi} \int_{\varphi=0}^{2\pi} \mathbf{e}_R \iint_{T_{max}} \mu(\alpha, \beta) \gamma_{\alpha,\beta}[\mathbf{H}(t) \cdot \mathbf{e}_R] \, d\alpha d\beta d\varphi d\theta && \text{(3.2b)}
\end{aligned}$$

for the ideal VPM. Moreover, the adaptions (2.9) or (2.40) are used for the SPM.

Since an infinite number of SPMs is not feasible, a finite number of SPMs has to be used. For each SPM, with its direction vector $\mathbf{e}_{R,i}$, a scalar magnetic flux density B_i is assigned. The scalar magnetic flux density is based on the scalar magnetic field strength $H_i = \mathbf{H} \cdot \mathbf{e}_{R,i}$. Hence, the approximate magnetic flux density

$$\begin{aligned}
\mathbf{B} &\approx \sum_{i=0}^{N-1} w_i B_i \mathbf{e}_{R,i} && \text{(3.3a)}\\
&= \sum_{i=0}^{N-1} w_i \hat{\Gamma}[\mathbf{H} \cdot \mathbf{e}_{R,i}] \mathbf{e}_{R,i} && \text{(3.3b)}
\end{aligned}$$

of the VPM with the corresponding weights w_i can be calculated. The weights are defined by the distribution function, which distributes the SPMs over the surface of the unit sphere. For a homogeneous distribution, the weights are $w_i = 1/N$, however a homogeneous distribution is in general impossible. Therefore, an approximative distribution function, see Section 3.3, has to be used.

3.2 Adaption of the Everett Function for the Vector Preisach Model

The Everett function (EF) $E(\alpha, \beta)$ for a SPM has to be adapted for the VPM [1, p. 172]. The adaption of the EF differs based on the dimension of the VPM. This thesis only deals with the three-dimensional VPM. Nevertheless, the two-dimensional case is mentioned for the sake of completeness.

Three-Dimensional Adaption For a three-dimensional distribution of SPMs, the adaption

$$P(\alpha, \lambda\alpha) = \frac{1}{2\pi\alpha} \frac{d}{d\alpha} [\alpha^2 E(\alpha, \lambda\alpha)] \tag{3.4}$$

with $\lambda = \beta/\alpha$ has to be applied [1, p. 179]. If the scalar EF is symmetrical along the line $\alpha = -\beta$, the adaption P for three dimensions will be symmetrical too. This property can be used for $\alpha = 0$, which yields an undefined case in (3.4). For an EF without hysteresis phenomenon, see Section 2.3, and for an according nonlinear function $B(\alpha)$, the three-dimensional adaption is defined as

$$P(\alpha, \lambda\alpha) = \frac{1}{2\pi\alpha}\frac{d}{d\alpha}[\alpha^2\big(B(\lambda\alpha) - B(\alpha)\big)] \tag{3.5}$$

$$= \frac{1}{2\pi}\Big(2B(\lambda\alpha) - 2B(\alpha) + \alpha\frac{d}{d\alpha}B(\lambda\alpha) - \alpha\frac{d}{d\alpha}B(\alpha)\Big). \tag{3.6}$$

Two-Dimensional Adaption For a two-dimensional distribution of the SPMs the adaption

$$P(\alpha, \lambda\alpha) = \frac{1}{\pi}\int_0^\alpha \frac{E(s, \lambda s) + s\frac{d}{ds}E(s, \lambda s)}{\sqrt{\alpha^2 - s^2}}\, ds \tag{3.7}$$

has to be applied [1, p. 177].

3.3 Point Distributions on Sphere Surfaces

The problem to be solved is to find a uniform distribution of points on the surface of a unit sphere. In this section, different methods to distribute points on the surface of a unit sphere are presented. A measure for the quality is introduced and the according results for the described distributions are shown in Table 6.

3.3.1 Calculation of Weights

The discrete integration over the surface of a unit sphere (3.3a) requires a weight w_i for each integration point. If the weights are not defined by the distribution function, a method for the calculation of the weights has to be found. A simple approach is to use the equation

$$w_i' = \sum_{j=0}^{N-1} \|\mathbf{r}_i - \mathbf{r}_j\| \tag{3.8}$$

for the non-normalised coefficients. Thereby, the vectors $\mathbf{r}_i$ and $\mathbf{r}_j$ describe the position vector of two different integration points. Further, the normalised weights are calculated by

$$w_i = \frac{w_i'}{\sum_{j=0}^{N-1} w_j'}. \tag{3.9}$$

The sum of the normalised weights $\sum_i w_i$ equals one.

3.3.2 Common Spherical Coordinates

The straight-forward approach to distribute points on a sphere surface is to use the common spherical coordinates. The common spherical coordinates are defined by

$$\begin{pmatrix} x \\ y \\ z \end{pmatrix} = \begin{pmatrix} r\ cos(\varphi) sin(\theta) \\ r\ sin(\varphi) sin(\theta) \\ r\ cos(\theta) \end{pmatrix} \tag{3.10}$$

with $r \in \mathbb{R}_0^+$, $\varphi \in [0, 2\pi)$ and $\theta \in [0, \pi]$. For the distribution on the surface of a unit sphere the radius r is set to one. The problem with this distribution is that the number of points in each latitude

θ is constant. Therefore, the density of points increases when θ approaches the poles $\theta_{pole} = \{0, \pi\}$. Fig. 3.1 depicts the common spherical coordinates distribution in an isometric view. Moreover, the output of the applied test pattern, described in Section 3.4, is shown. It shows that for a VPM based on common spherical coordinates the absolute value of the output changes for input values with a constant absolute value but different orientations. Therefore, common spherical coordinates are not usable for VPMs.

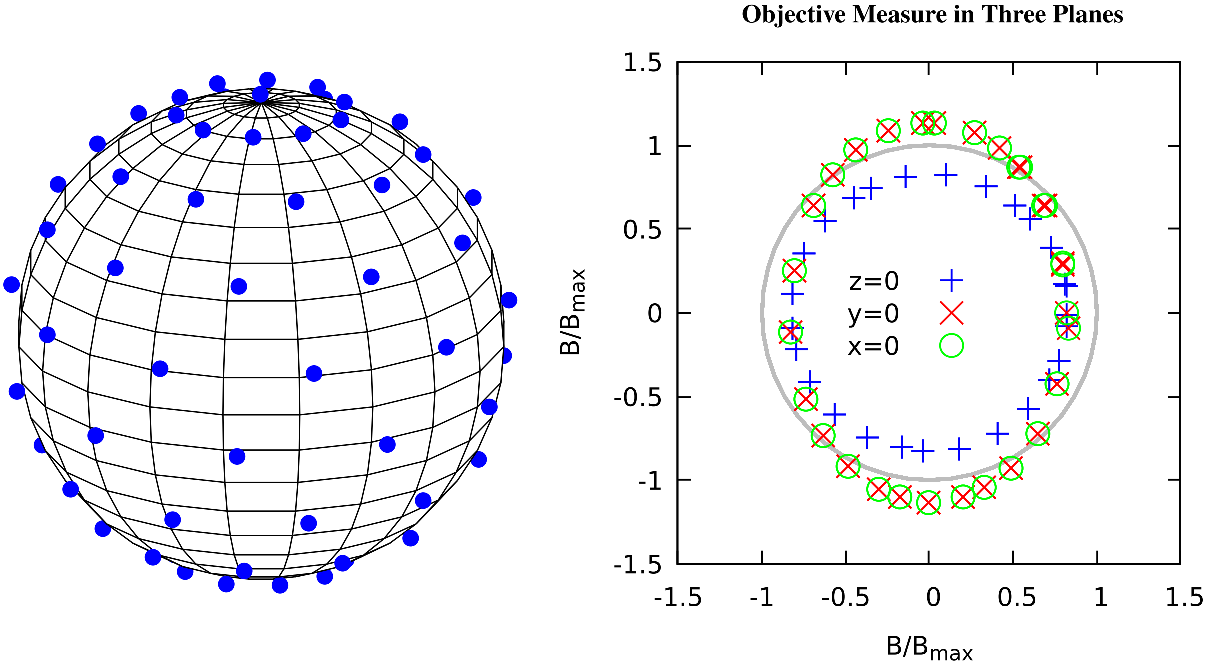

Figure 3.1: Distribution based on common spherical coordinates with $N = 82$. Isometric view (left). Output after applying the test pattern (right). The grey circle serves as reference.

3.3.3 Advanced Spherical Coordinates

The advanced spherical coordinates [9] deal with the issue of the common spherical coordinates by adapting the number of points

$$N_{\varphi,i} = \lfloor 1/2 + \sqrt{3} N_\theta sin(\theta_i) \rfloor \tag{3.11}$$

at each equally spaced polar angle $\theta_i \in [0, \pi]$. The parameter N_θ defines the total number of polar angles. The azimuthal angles $\varphi_i \in [0, 2\pi)$ are equally spaced too. Fig. 3.2 illustrates the advanced spherical coordinates distribution in an isometric view. Moreover, the output of the applied test pattern, described in Section 3.4, is shown.

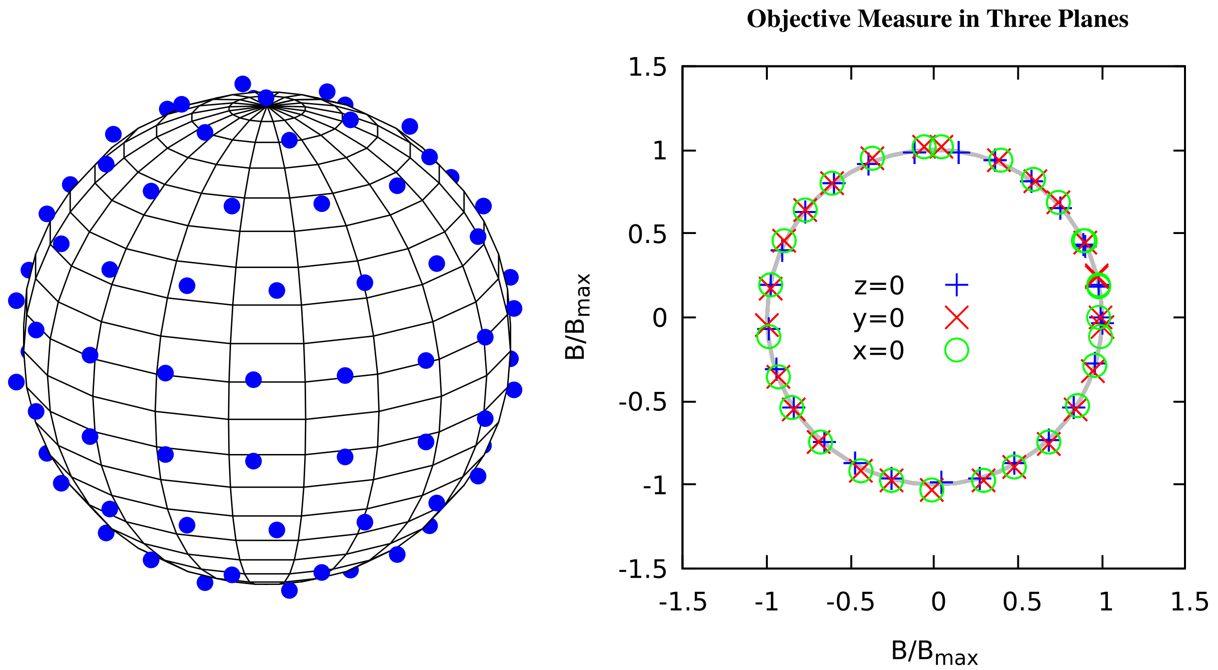

Figure 3.2: Advanced spherical coordinates with $N = 100$. Isometric view (left). Output after applying the test pattern (right). The grey circle serves as reference.

3.3.4 Gauss-Legendre Sphere Quadrature

The general idea of the Gauss-Legendre spherical coordinates [10] is based on the one-dimensional Gauss-Legendre quadrature. The Gauss-Legendre quadrature approximates

$$I(f) = \int_{-1}^{1} f(x)\, dx \tag{3.12}$$

by a weighted sum

$$I(f) \approx \sum_{i=0}^{N-1} w_i\ f(q_i). \tag{3.13}$$

To this base, the function f is evaluated on a set of N nodes q_i and the weights w_i are used. The nodes q_i are the roots of the Legendre polynomials of order N. The Legendre polynomials are defined by the Rodrigues formula [11]

$$P_N(q) = \frac{1}{2^N N!} \frac{d^N}{dq^N} \left((q^2 - 1)^N \right) \tag{3.14}$$

and the weights w_i are based on the derivation

$$P'_N(q_i) = \left. \frac{dP_N(q)}{dq} \right|_{q=q_i} = \frac{1}{2^N N!} \frac{d^{N+1}}{dq^{N+1}} \left((q^2 - 1)^N \right) \tag{3.15}$$

of (3.14). Consequently, the weights are calculated by

$$w_i = \frac{2}{\left(1 - q_i^2\right) \left(P'_N(q_i)\right)^2}. \tag{3.16}$$

Applying this idea to the integral over the surface of a unit sphere

$$I_{SPH}(f) = \int_0^{\pi} \int_0^{2\pi} f(\theta, \varphi)\ sin(\theta)\ d\varphi d\theta \tag{3.17}$$

results in a nested sum with a number of N_θ polar angles and $N_{\varphi,i}$ azimuthal angles, which is calculated by (3.11). Further, the angles $\theta_i \in [0, \pi]$ are defined as transformed nodes q_i and each angle $\varphi_j \in [0, 2\pi]$ is a transformed node q_j. Further,

$$I_{SPH} \approx \sum_{i=1}^{N_\theta} w_i \sum_{j=1}^{N_{\varphi,i}} w_j\ f(\theta_i, \varphi_j) \tag{3.18}$$

represents the approximation of the spherical integral using the expanded Gauss-Legendre quadrature. The described coordinate distribution is shown in Fig. 3.3 as isometric view. The picture shows that the point density is higher at the interval boundaries. Moreover, the output of the applied test pattern, described in Section 3.4, is shown.

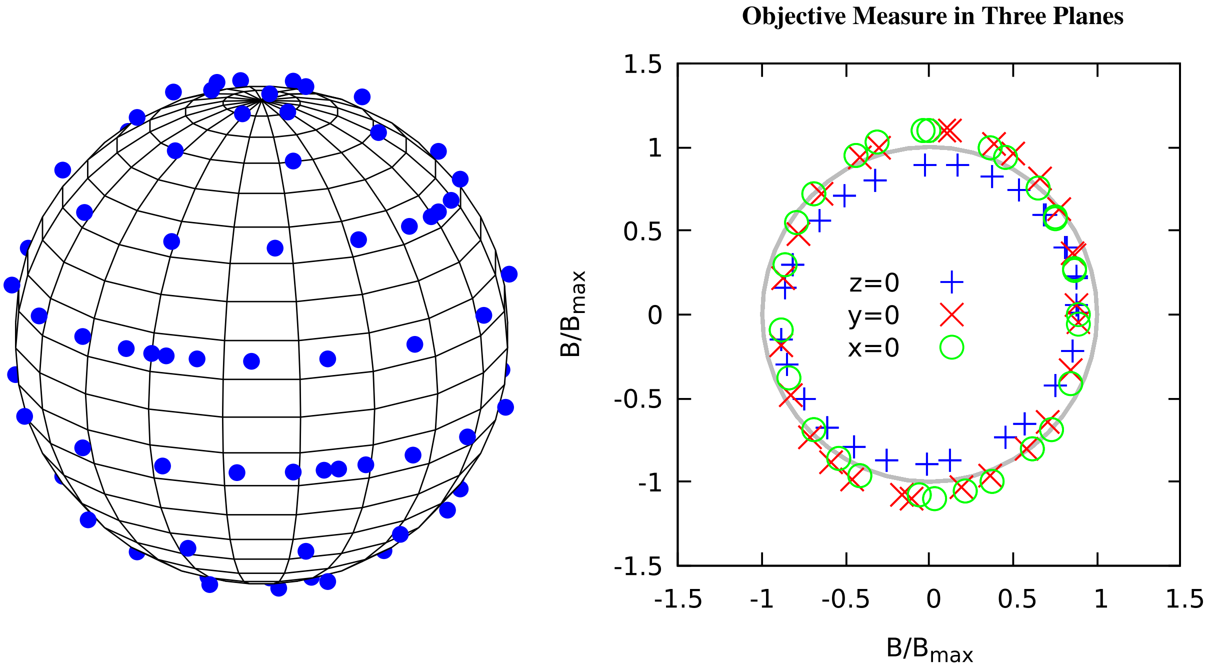

Figure 3.3: Gauss-Legendre spherical coordinates with $N = 90$. Isometric view (left). Output after applying the test pattern (right). The grey circle serves as reference.

3.3.5 Combination of Gauss-Legendre and Advanced Spherical Coordinates

This section describes a combination of the advanced spherical coordinates and the Gauss-Legendre spherical coordinates. Therefore, the polar angles θ_i are defined by the scaled nodes $q_i \in$ of the Gauss-Legendre quadrature. Moreover, the number of azimuthal angles φ_j is based on (3.11), but are distributed evenly. Fig. 3.4 presents the isometric view and the output based on the test pattern, described in Section 3.4.

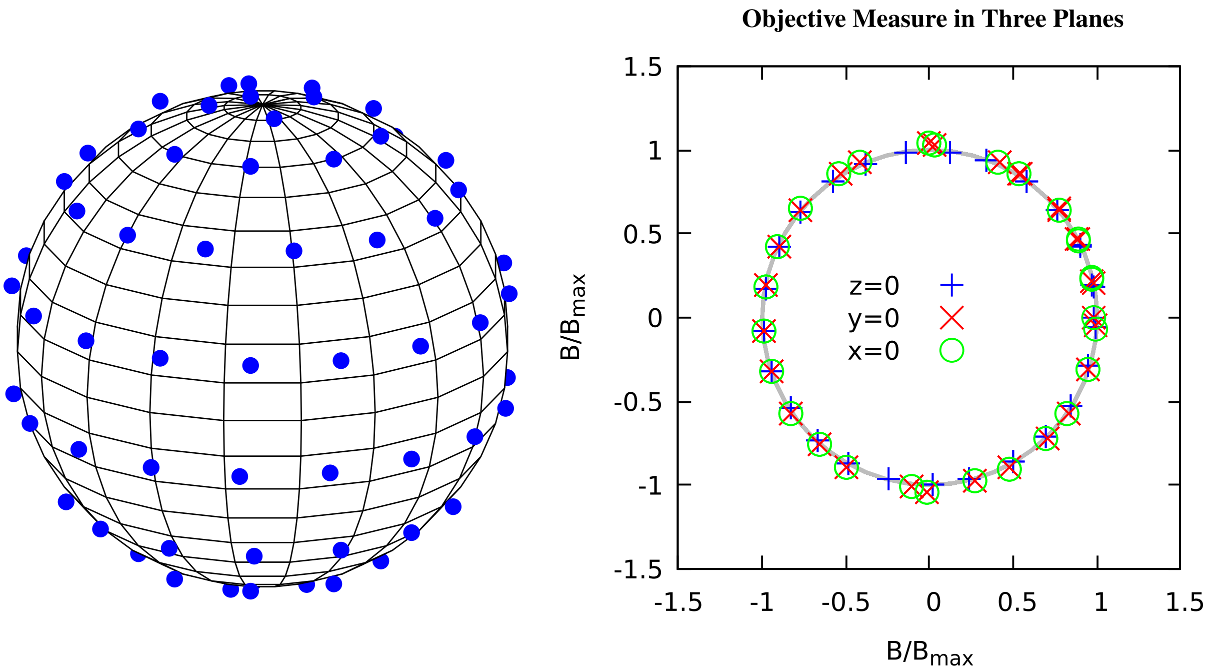

Figure 3.4: Coordinates based on the combination of Gauss-Legendre spherical coordinates and advanced polar coordinates with $N = 90$. Isometric view (left). Output after applying the test pattern (right). The grey circle serves as reference.

3.3.6 Lebedev Spherical Coordinates

The Lebedev quadrature is an approximation to the surface integral of a function over a sphere. The values for the position vectors and the according weights are tabulated up to order 131 [12]. Fig. 3.5 shows the Lebedev spherical coordinates distribution in an isometric view. Moreover, the output of the applied test pattern, described in Section 3.4, is shown.

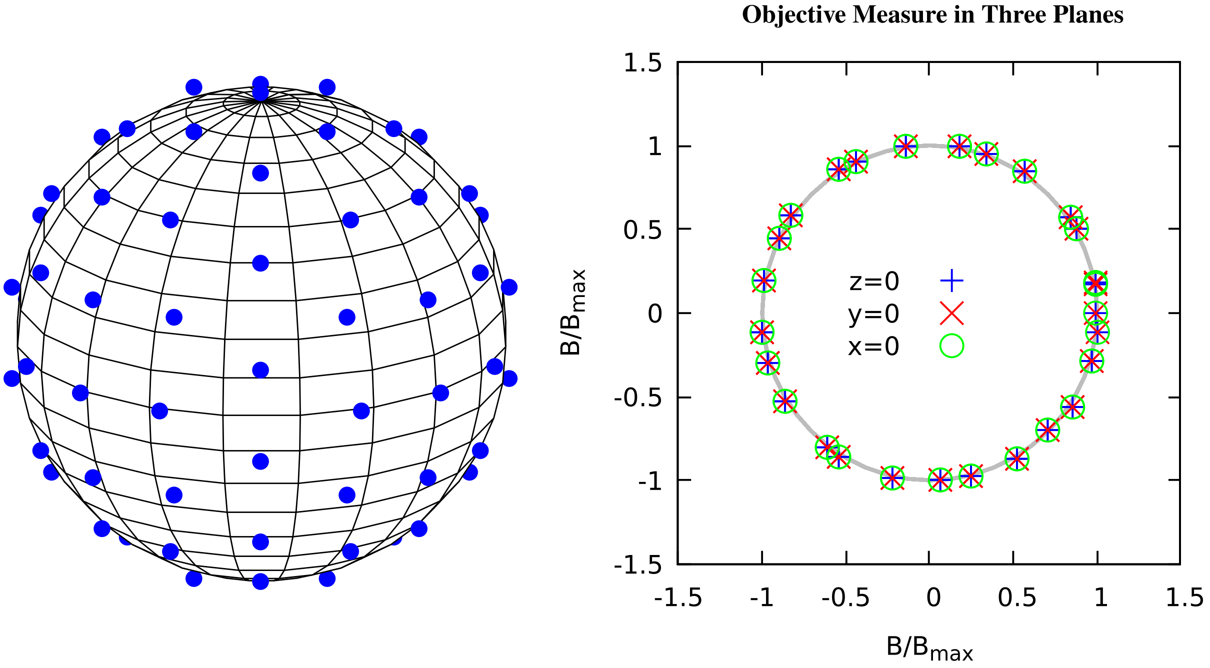

Figure 3.5: Coordinates based on the Lebedev angular quadrature with $N = 86$. Isometric view (left). Output after applying test pattern (right). The grey circle serves as reference.

3.4 Evaluation of the Accuracy of the Point Distributions

To evaluate the quality of a point distribution, a sequence of input values $\mathbf{H} = H_{max}\mathbf{e}_H$ with a constant absolute value H_{max} is implied to a VPM using one of the point distributions in Section 3.3. Starting from a demagnetised model, the orientation of the vector is rotated in one of the basic planes ($z = 0, y = 0, x = 0$) in N_{rot} steps. For each discrete orientation $\mathbf{e}_{R,i}$, the resulting output value $\mathbf{B}_i$ of the VPM is stored. After rotating in one plane, the VPM gets demagnetised again. In the next step, the procedure is repeated for another plane.

The magnetic flux density B_{max} of the saturated material serves as reference value. The difference $\alpha_i = |\mathbf{B}_i| - B_{max}$ between each output value and the reference should be as small as possible. Moreover, the value $B_{i,x/y/n} = \mathbf{n} \cdot \mathbf{B}_i$, with $\mathbf{n}$ as the vector of the rotation axis, should vanish.

Consequently, the measures

$$m_x = \sum_{i=0}^{N_{rot}-1} \left(\sqrt{B_{i,y}^2 + B_{i,z}^2} - B_{max}\right)^2 + |B_{i,x}|, \tag{3.19}$$

$$m_y = \sum_{i=0}^{N_{rot}-1} \left(\sqrt{B_{i,x}^2 + B_{i,z}^2} - B_{max}\right)^2 + |B_{i,y}| \text{ and} \tag{3.20}$$

$$m_z = \sum_{i=0}^{N_{rot}-1} \left(\sqrt{B_{i,x}^2 + B_{i,y}^2} - B_{max}\right)^2 + |B_{i,z}| \tag{3.21}$$

for the $x = 0$, the $y = 0$ and the $z = 0$ plane can be introduced, respectively. On the one hand, the measures consider variation of the absolute value and on the other take into account that the output vector $\mathbf{B}_i$ has to be oriented in the according plane. As an overall measure for all planes, the sum

$$m = m_x + m_y + m_z \tag{3.22}$$

is used. The measure m indicates a better distribution, as the value m gets small.

Table 6 presents the quality measure for all introduced distributions. The last three distributions are reduced to half spheres. This reduction is based on the proposition that the point distribution exhibits one plane of symmetry and an integration over the surface of a unit sphere in (3.1) can be reduced to an integration over a half sphere [1, p. 151]. For the measurement an EF based on the arctangent, see Section 2.2.2, with $N_A = 601$ discretisation steps of the Preisach plane is used. The discretisation of the Preisach plane follows the adaptive discretisation algorithm, see Section 2.4.4. The number of rotational steps is $N_{rot} = 5000$.

The Lebedev distribution and the advanced spherical coordinates are the most accurate point distributions used for a VPM.

Spherical Coordinates	N	m_x	m_y	m_z	m
Common	82	339.3	121.8	121.8	583
Advanced	100	0.2	1.8	1.8	3.9
Gauss-Legendre	90	139.8	59.4	51.3	250.6
Gauss-Legendre Advanced	90	0.4	3.1	3.1	6.6
Lebedev	86	1.3	1.3	1.3	4.0
Half Sphere Advanced	61	0.9	1.1	1.6	3.7
Half S. Gauss-Legendre Advanced	55	0.3	1.7	1.6	3.6
Half S. Lebedev	43	1.3	1.3	1.3	4.0

Table 6: Accuracy of different distributions with respect to the numerical experiment.

3.5 Calculation of the Material Relations

This sections derives the tensor-valued permeability $\overline{\overline{\mu}}$ which yields the material relation $\mathbf{B} = \overline{\overline{\mu}}\mathbf{H}$. Moreover, the formula for the approximation of the tensor-valued differential permeability $\overline{\overline{\mu}}^{\Delta}$ is shown. The double bar denotes that the values are tensors.

In the ideal VPM (3.1), the calculated output value $\mathbf{B}$ results from an input value $\mathbf{H}$ and is computed by a superposition of an infinite number of SPMs. The SPMs are distributed on a unit sphere surface, see Section 3.3. Thus, each SPM is connected with an orientation $\mathbf{e}_R$, an input value $H_R = \mathbf{H}\cdot\mathbf{e}_R$ and a resulting output value B_R. Accordingly, the permeability

$$\mu_R = \frac{B_R}{H_R} \tag{3.23}$$

can be calculated, see Section 2.9.1, in a post-processing step. The calculation of the permeability $\overline{\overline{\mu}}$ in a VPM is based on the scalar permeability values μ_R [13].

Starting from the definition of the VPM (3.1), the magnetic flux density

$$\mathbf{B} = \overline{\overline{\mu}}\mathbf{H} = \oint_\Gamma \mathbf{e}_R B_R \, d\Gamma \tag{3.24}$$

can be calculated. Considering the permeability of the SPM (3.23), the vector output $\mathbf{B}$ in (3.24) can be calculated as

$$\overline{\overline{\mu}}\mathbf{H} = \oint_\Gamma \mu_R \mathbf{e}_R H_R \, d\Gamma \tag{3.25}$$

$$= \oint_\Gamma \mu_R \mathbf{e}_R (\mathbf{e}_R^T \mathbf{H}) \, d\Gamma \tag{3.26}$$

$$= \oint_\Gamma \mu_R \mathbf{e}_R \mathbf{e}_R^T \, d\Gamma \; \mathbf{H}, \tag{3.27}$$

where the projected input value $H_R = \mathbf{e}_R \cdot \mathbf{H} = \mathbf{e}_R^T\mathbf{H}$ is used. Finally, the permeability of a VPM is defined as

$$\overline{\overline{\mu}} = \oint_\Gamma \mu_R \mathbf{e}_R \mathbf{e}_R^T \, d\Gamma. \tag{3.28}$$

However, the permeability μ_R of the SPMs is not defined in every case, see Section 2.9.1. Therefore, the differential permeability μ_R^Δ is used for electromagnetic simulations. The calculation of the tensor-valued differential permeability $\overline{\overline{\mu}}^{\Delta}$ is done analogously to (3.28) and yields

$$\overline{\overline{\mu}}^{\Delta} = \oint_\Gamma \mu_R^\Delta \mathbf{e}_R \mathbf{e}_R^T \, d\Gamma. \tag{3.29}$$

Taking into account the discrete distribution of the SPMs, the integrals in (3.28) and (3.29) are transformed into the weighted sums

$$\overline{\overline{\mu}} = \sum_{i=0}^{N-1} w_i \; \mu_{R,i} \; \mathbf{e}_{R,i}\mathbf{e}_{R,i}^T \quad \text{and} \quad \overline{\overline{\mu}}^{\Delta} = \sum_{i=0}^{N-1} w_i \; \mu_{R,i}^\Delta \; \mathbf{e}_{R,i}\mathbf{e}_{R,i}^T, \tag{3.30}$$

where N denotes the number of SPMs, w_i are the weights defined by the point distribution and $\mathbf{e}_{R,i}$ are the direction vectors. Fig. 3.6 shows the used nomenclature and convention for spherical coordinates with $r \in \mathbb{R}_0^+, \varphi \in [0, 2\pi)$ and $\theta \in [0, \pi]$.

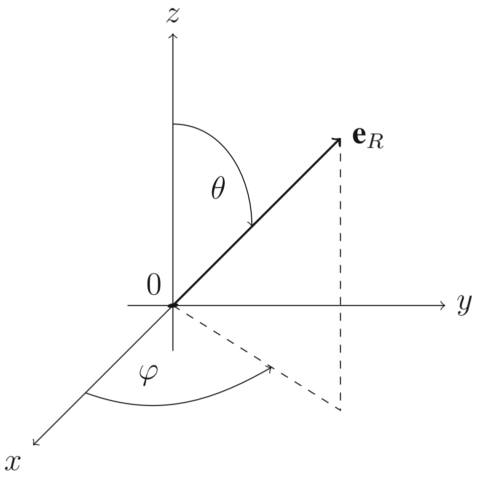

Figure 3.6: Nomenclature for spherical coordinates.

For a three-dimensional VPM, the unit vector $\mathbf{e}_R$ is based on spherical coordinates and is defined by

$$\begin{aligned} \mathbf{e}_R^T &= (x, y, z) && (3.31a) \\ &= \big(cos(\varphi)sin(\theta), sin(\varphi)sin(\theta), cos(\theta)\big). && (3.31b) \end{aligned}$$

Therefore, the multiplication in (3.28) and (3.29) results in

$$\begin{aligned} \mathbf{e}_R\mathbf{e}_R^T &= \begin{pmatrix} x^2 & xy & xz \\ xy & y^2 & yz \\ xz & yz & z^2 \end{pmatrix} && (3.32a) \\ &= \begin{pmatrix} cos^2(\varphi)sin^2(\varphi) & cos(\varphi)sin(\varphi)sin^2(\theta) & cos(\varphi)sin(\theta)cos(\theta) \\ cos(\varphi)sin(\varphi)sin^2(\theta) & sin^2(\varphi)sin^2(\theta) & sin(\varphi)sin(\theta)cos(\theta) \\ cos(\varphi)sin(\theta)cos(\theta) & sin(\varphi)sin(\theta)cos(\theta) & cos^2(\theta) \end{pmatrix}. && (3.32b) \end{aligned}$$

Analogously,

$$\mathbf{e}_r\mathbf{e}_r^T = \begin{pmatrix} x^2 & xy \\ xy & y^2 \end{pmatrix} = \begin{pmatrix} cos^2(\varphi) & sin(\varphi)cos(\varphi) \\ sin(\varphi)cos(\varphi) & sin^2(\varphi) \end{pmatrix}. \qquad (3.33)$$

represents the required term for a two-dimensional VPM with the polar coordinates $\mathbf{e}_r^T = \big(cos(\varphi), sin(\varphi)\big) = (x, y)$.

3.6 Energy-Based Verification

The energy-based verification uses an orthogonal cube with the dimensions $[W, L, H] = [1, 1, 1]$ which is created by Netgen/NGSolve [2]. Further, a coefficient function (CF) is introduced, which will represent the input CF **H** for five different models. The five models are

- a nonlinear model using a CF, which will be used as reference model,
- a single scalar Preisach operator,
- a single vector Preisach operator,
- a scalar CF based on SPMs and

- a vector CF based on VPMs.

For each model the output value is compared to the reference model. The comparison of the different models is valid as long as the input CF is varying in one component and is equal for the whole region.

For the models using a CF, the energy in the cube is calculated by

$$W_H = \int_\Omega w \; d\Omega, \tag{3.34}$$

where, w is the energy-based functional

$$w = \frac{1}{2}\mathbf{B} \cdot \mathbf{H}. \tag{3.35}$$

For the models based on single operators,

$$W_H = w \; V = w, \tag{3.36}$$

where $V = 1$ is the volume of the unit cube, is used.

Verification without Hysteresis Based on Section 2.3, the EF can be adapted to result in a Preisach model without hysteresis phenomenon. For the calculation of the relative error

$$\varepsilon = \left| \frac{W_{H,*} - W_{H,NL}}{W_{H,NL}} \right| 100\% \tag{3.37}$$

the energy $W_{H,NL}$ of the nonlinear model is used as reference.

The calculated error ε for the tested models without hysteresis phenomenon is shown in Fig. 3.7. The errors of the CF-based solutions are identical with the solutions based on single operators. Therefore, the implemented CFs are implemented correctly. The maximal error of the scalar models is 2.55% and 2.56% for the vector models. The input sequence starts from 0 and increases to the positive saturation $H_{max} = 1640$A/m. Further, it decreases to the negative saturation and increases to the positive saturation again. The total number of equidistant steps is 100. The used distribution is based on the advanced spherical coordinates with $N_{dist} = 100$.

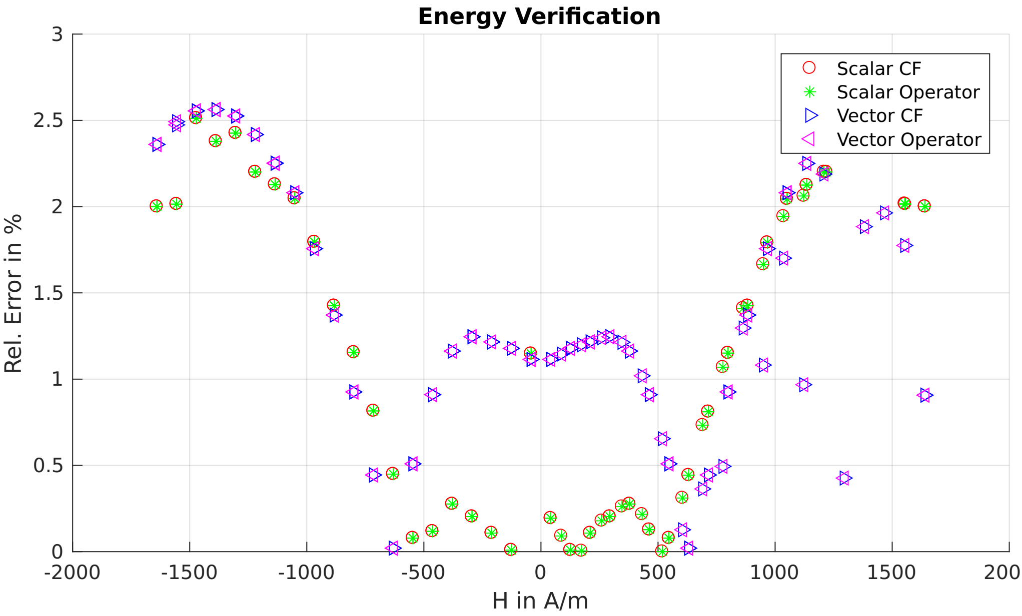

Figure 3.7: Relative error of various Preisach operators without hysteresis.

Verification with Hysteresis For the comparison of Preisach models with hysteresis, the energy-based functional (3.36) is considered. The relative error

$$\varepsilon = \left| \frac{W_{H,*} - W_{H,SPM}}{W_{H,SPM}} \right| 100\% \tag{3.38}$$

for both VPMs is calculated in every simulation step. The energy $W_{H,SPM}$ of the single scalar Preisach operator is used as reference.
For the experiment, the material is demagnetised first. The x-component of the input sequence forms the initial magnetisation curve followed by the major loop. The number of SPMs for the VPMs is 230 and the distribution is based on advanced spherical coordinates.

The calculated relative error of the experiment is depicted in Fig. 3.8. The maximum overall error is 0.88%.

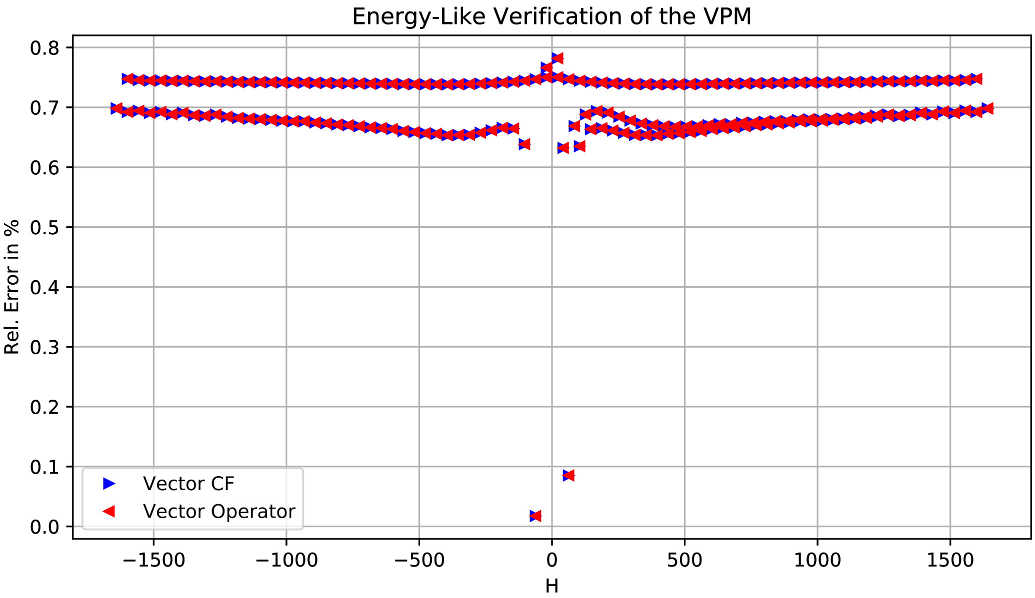

Figure 3.8: Relative error of various Preisach operators based on the energy-based functional.

3.7 Estimation of the Complexity

Memory Complexity Analogously to the SPM, the worst-case in terms of required memory occurs in the discrete demagnetised state, see Section 2.6.1. The superposition of N_{SPM} discrete demagnetised SPMs, which are using the cumulative sum, requires

$$N_{total} = N_{EV} + 3N_{corner}\, N_{SPM} \tag{3.39}$$

values to be stored. This equation is only valid for homogeneous materials, since the EF is the same for all SPMs.

Execution Time Complexity Since the VPM is a superposition of N_{SPM} SPMs,

$$t_{sim} = N_{SPM}\, t_{scalar} \tag{3.40}$$

is a worst-case execution time estimation for the VPM. Thereby, t_{scalar} represents the execution time of a SPM for an input sequence of the same length. Consequently, the complexity class of the VPM $\mathcal{O}(n \log n)$ is the same as the complexity class of the SPM.

4 Biot-Savart Field

The Biot-Savart field is essential for simulations of electromagnetic field problems. In simulations using the finite element method (FEM), known current densities can be prescribed in domains or can be considered analytically by the known magnetic field. The latter approach has the advantage that the corresponding region does not need to be modelled by finite elements.
The Biot-Savart law

$$\mathbf{H}(\mathbf{r}) = \frac{1}{4\pi} \int_{\Omega} \mathbf{J}(\mathbf{r}') \times \frac{\mathbf{r} - \mathbf{r}'}{|\mathbf{r} - \mathbf{r}'|^3} \, d\Omega \tag{4.1}$$

allows to calculate the magnetic field strength $\mathbf{H}$ of an arbitrary current density $\mathbf{J}$. Moreover, the Biot-Savart field of a finite filamentary current

$$\mathbf{H}(P) = \frac{I}{4\pi|\mathbf{v}|}\big(\sin(\alpha_2) - \sin(\alpha_1)\big)\mathbf{e}_H \tag{4.2}$$

with the parameters shown in Fig. 4.1, can be calculated. Thereby, $|\mathbf{v}|$ is the smallest distance between the filamentary current and point P and $\mathbf{e}_H = \frac{\mathbf{v}}{|\mathbf{v}|} \times \mathbf{e}_I$ with $\mathbf{e}_I$ representing the direction vector pointing in the direction of the current [14].

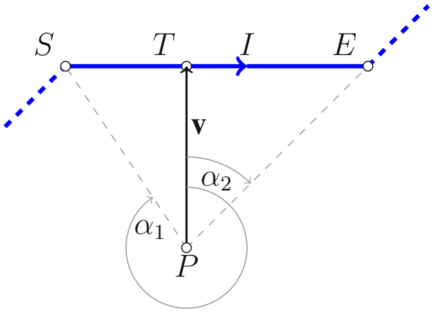

Figure 4.1: Notation of variables for a segment of a filamentary current in the Biot-Savart law.

The segment of the filamentary current is defined by its start point S and its end point E. The unit vector $\mathbf{e}_I = \frac{\mathbf{E}-\mathbf{S}}{|\mathbf{E}-\mathbf{S}|}$ points in the direction of the filamentary current. Point P prescribes an arbitrary point in the region of interest.

Further, point T denotes the point on the line g of the filamentary current ($g : S + k\mathbf{e}_I, k \in \mathbb{R}$) with the smallest distance between the line g and point P. Moreover, the absolute value $|\mathbf{v}|$ of the vector $\mathbf{v} = T - P$ indicates the smallest distance between point P and the line g.
By using the property of the vector cross product $|\mathbf{a} \times \mathbf{b}| = |\mathbf{a}||\mathbf{b}| \sin(\alpha)$, the required angles

$$\alpha_1 = \arcsin\left(\frac{|(S-P) \times \mathbf{v}|}{|\mathbf{v}||S-P|}\right) \text{ and } \alpha_2 = \arcsin\left(\frac{|(E-P) \times \mathbf{v}|}{|\mathbf{v}||E-P|}\right) \tag{4.3}$$

can be calculated. In the case that $\Big((S-P) \times \mathbf{v}\Big) \cdot \Big((E-P) \times \mathbf{v}\Big) < 0$, which means that the angles are not considered consistently, the angle $\alpha_2 = 2\pi - \alpha_2$ has to be adapted.

Moreover, the superposition of connected finite filamentary currents allows the construction of more complex structures. For instance a coil or a rectangular loop can be composed. Fig. 4.2 displays the calculated Biot-Savart field of a coil with five windings. The total number of segments is $N_{seg} = 35$, the length of the coil is 0.5m and the radius is 0.2m. Nevertheless, the calculation of the superposition is time-demanding.

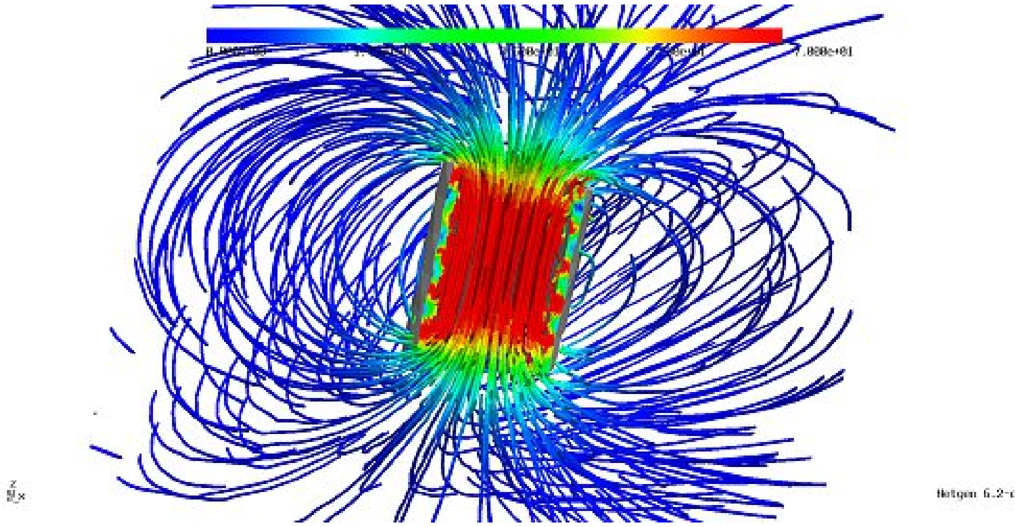

Figure 4.2: Calculated Biot-Savart field for a coil with 5 windings, coloured by $|\mathbf{H}|$.

It is worth mentioning that in most FEM-simulations with electromagnetic excitation, considered by modelled coils in the finite element mesh, the current density in the according domain rotates only around a single axis. For instance a coil directed in z-direction would be modelled as $\mathbf{J} = \frac{J_0}{\sqrt{x^2+y^2}}(-y\mathbf{e}_x + x\mathbf{e}_y)$. This does not reflect the actual physical current density, since the current flows in conductor windings with a slope. Consequently, the magnetic field is not rotationally symmetric. Additionally, stray fields within the coil are not reflected properly. The present approach using the Biot-Savart field respects these issues accurately.

5 Infinite Sheet - Fixed-Point Method

In this section, the fixed-point method with nonlinear material relations is examined for solving boundary value problems (BVPs). Since this section focuses on the fixed-point method, a minimal geometry is used. The problem is illustrated in Fig. 5.1 and consists of two attached cuboids. The solution represents the static magnetic field in an infinite sheet. The material relation in the first domain Ω_{lin} is linear, the other one Ω_{Fe} is nonlinear. The dimensions of the three-dimensional model are $(W \times L \times H) = (1 \times 2 \times 1)$. A Cartesian coordinate system is assumed with the origin in the centre of the cuboid. The considered region $\Omega = \Omega_{lin} \cup \Omega_{Fe}$ does not include currents.

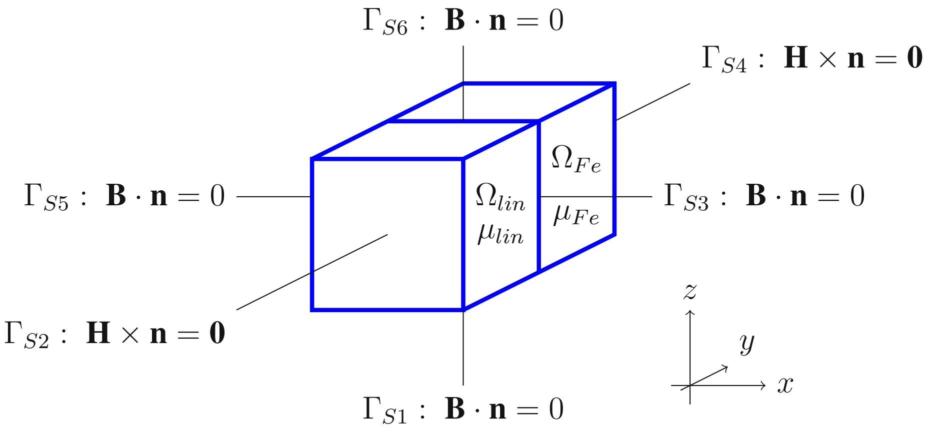

Figure 5.1: BVP of an infinite sheet with boundary conditions.

The Maxwell equations of the static magnetic field are

$$\nabla \times \mathbf{H} = \mathbf{0} \tag{5.1a}$$
$$\nabla \cdot \mathbf{B} = 0. \tag{5.1b}$$

Therefore, the magnetic scalar potential Φ can be introduced by

$$\mathbf{H} = -\nabla\Phi, \tag{5.2}$$

which fulfils $\nabla \times \mathbf{H} = -\nabla \times \nabla\Phi \equiv \mathbf{0}$ identically. The linear permeability μ_{lin} in Ω_{lin} and the nonlinear permeability μ_{FR} in Ω_{Fe} can be combined to a global permeability

$$\mu(\Phi(\mathbf{x})) = \begin{cases} \mu_{lin}, & \mathbf{x} \in \Omega_{lin} \\ \mu_{Fe}(\Phi), & \mathbf{x} \in \Omega_{Fe} \end{cases}. \tag{5.3}$$

Combined with the material relation $\mathbf{B} = \mu(\Phi)\mathbf{H}$, the BVP

$$-\nabla \cdot \Big(\mu(\Phi)\nabla\Phi\Big) = 0 \qquad \text{in } \Omega \tag{5.4a}$$
$$-\mathbf{n} \cdot \mu\nabla\Phi = 0 \qquad \text{on } \Gamma_{S1} \cup \Gamma_{S3} \cup \Gamma_{S5} \cup \Gamma_{S6} \tag{5.4b}$$
$$\Phi = \Phi_0 \qquad \text{on } \Gamma_{S2} \cup \Gamma_{S4} \tag{5.4c}$$

is derived. An excitation of the problem is considered using boundary conditions. With the homogeneous Neumann boundary conditions on $\Gamma_{S1} \cup \Gamma_{S3} \cup \Gamma_{S5} \cup \Gamma_{S6}$, the problem describes an infinite sheet. Dirichlet boundary conditions

$$\mathbf{n} \times \mathbf{H} = \mathbf{0} \qquad \text{on } \Gamma_{S2} \cup \Gamma_{S4} \tag{5.5}$$

at the front Γ_{S2} and at the back Γ_{S4} are considered. An exciting magnetic field $\mathbf{H}_0 = H_0\mathbf{e}_y$ is prescribed by

$$\Phi_0 = c(y) = -yH_0. \tag{5.6}$$

5.1 Weak Formulation

To obtain the weak formulation

$$-\int_\Omega \nabla \cdot (\mu \nabla \Phi)\, v \, d\Omega = 0, \tag{5.7}$$

the boundary value problem (5.4a) is multiplied by a scalar test function v and is integrated over Ω. With the vector identity

$$\nabla \cdot (v\mu\nabla\Phi) \equiv v\nabla \cdot (\mu\nabla\Phi) + \mu\nabla\Phi \cdot \nabla v \tag{5.8}$$

the weak formulation can be written as

$$\int_\Omega \mu\nabla\Phi \cdot \nabla v - \nabla \cdot (v\mu\nabla\Phi)\, d\Omega = 0. \tag{5.9}$$

Using the Gauss' theorem and the required homogeneous test function on Dirichlet boundaries, the equation transforms to

$$\int_\Omega \mu\nabla\Phi \cdot \nabla v \, d\Omega = \int_{\Gamma_N} \mathbf{n} \cdot (v\mu\nabla\Phi)\, d\Gamma. \tag{5.10}$$

The weak formulation

$$\int_\Omega \mu\nabla\Phi \cdot \nabla v \, d\Omega = 0 \tag{5.11}$$

is derived by taking the homogeneous Neumann boundary conditions into account.

5.2 3D Fixed-Point Method

To solve the nonlinear material relation, the iterative fixed-point method is used [15], [16]. For the fixed-point method, the constant fixed-point permeability μ_{FP} is introduced to compute the magnetic scalar potential Φ in the $(n+1)$-th iteration instance. Considering the fixed-point method, the BVP results in

$$\int_{\Omega_{lin}} \mu_{lin}\nabla\Phi \cdot \nabla v \, d\Omega = 0 \qquad \text{in } \Omega_{lin} \tag{5.12a}$$

$$\int_{\Omega_{Fe}} \mu_{FP}\nabla\Phi \cdot \nabla v \, d\Omega = -\int_{\Omega_{Fe}} \left(\mu_{FP} - \mu(\mathbf{H}^{(n)})\right)\mathbf{H}^{(n)} \cdot \nabla v \, d\Omega \qquad \text{in } \Omega_{Fe} \tag{5.12b}$$

$$-\mathbf{n} \cdot \mu\nabla\Phi = 0 \qquad \text{on } \Gamma_{S1} \cup \Gamma_{S3} \cup \Gamma_{S5} \cup \Gamma_{S6} \tag{5.12c}$$

$$\Phi = -yH_0 \qquad \text{on } \Gamma_{S2} \cup \Gamma_{S4} \tag{5.12d}$$

with the known solution $\mathbf{H}^{(n)} = -\nabla\Phi^{(n)}$.

5.3 1D Fixed-Point Method

Since the field problem is symmetrical in two directions, a problem reduction to one dimension can be applied. Fig. 5.2 illustrates the reduced model with the used hat functions as approach and trial functions and the numeration of the nodes and the elements.

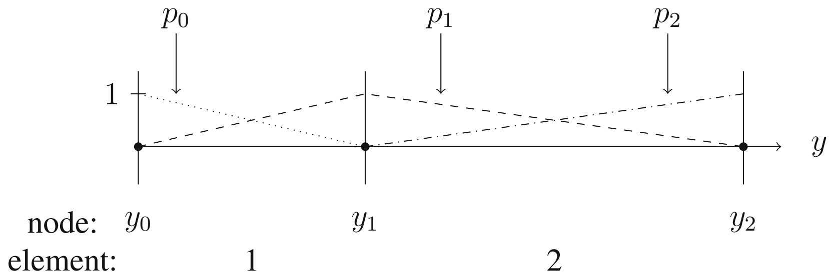

Figure 5.2: Reduced finite element model of the infinite sheet with hat functions p_i.

The reduction of the scalar potential (5.2) to one dimension yields

$$\Phi = \Phi(y) \tag{5.13}$$

the weak formulation of the scalar BVP

$$\int_{y_0}^{y_2} \mu(\Phi)\partial_y\Phi\partial_y v \; dy = 0. \tag{5.14}$$

The weak formulation with the fixed-point method the weak formulation (5.12) becomes

$$\int_{y_0}^{y_1} \mu_{lin}\partial_y\Phi\partial_y v \; dy = 0 \qquad \text{in } [y_0, y_1] \tag{5.15a}$$

$$\int_{y_1}^{y_2} \mu_{FP}\partial_y\Phi\partial_y v \; dy = -\int_{y_1}^{y_2} \big(\mu_{FP} - \mu(H^{(n)})\big)H^{(n)} \; v \; dy \qquad \text{in } [y_1, y_2] \tag{5.15b}$$

$$\Phi = -yH_0 \qquad \text{on } y_0, y_2. \tag{5.15c}$$

The Galerkin method [17, p. 45]is used. The approximative solution $\Phi_h \approx \Phi$ is written as

$$\Phi_h = \sum_{j=0}^{2} \Phi_j \; p_j(y). \tag{5.16}$$

To assembly the finite element matrix

$$\sum_{j=0}^{2} \int_{y_0}^{y_2} \mu(y)\partial_y p_j(y)\partial_y p_i(y) \; dy = -\int_{y_1}^{y_2} \big(\mu_{FP} - \mu_{Fe}(H^{(n)})\big)H^{(n)}p_i(y) \; dy. \tag{5.17}$$

is computed, where the permeability

$$\mu(y) = \begin{cases} \mu_{lin} & , y_0 \le y \le y_1 \\ \mu_{FP} & , y_1 < y \le y_2 \end{cases} \tag{5.18}$$

and the known magnetic field strength $H^{(n)} = -\frac{u_2^{(n)} - u_1^{(n)}}{y_2 - y_1}$ are used. The equation system

$$S\mathbf{u} = \mathbf{f} \tag{5.19}$$

is obtained with

$$S = \begin{pmatrix} S_{00} & S_{01} & S_{02} \\ S_{10} & S_{11} & S_{12} \\ S_{20} & S_{21} & S_{22} \end{pmatrix}, \qquad \mathbf{u} = \begin{pmatrix} \Phi_0 \\ \Phi_1 \\ \Phi_2 \end{pmatrix} \text{ and } \qquad \mathbf{f} = \begin{pmatrix} f_0 \\ f_1 \\ f_2 \end{pmatrix} \tag{5.20}$$

as stiffness matrix, solution and load vector, respectively.

Due to the Dirichlet boundary values at y_0 and y_2, the equation system (5.19) is reduced. This reduction is equivalent to setting the according matrix and vector elements

$$S_{00} = S_{22} = 1, \tag{5.21a}$$

$$S_{01} = S_{02} = S_{20} = S_{21} = 0, \tag{5.21b}$$

$$f_0 = u_0, \tag{5.21c}$$

$$f_2 = u_2. \tag{5.21d}$$

The assembling of the stiffness matrix S and the load vector **f** yields

$$S_{10} = \int_{y_0}^{y_1} \mu_{lin} \partial_y p_1(y) \partial_y p_0(y) \, dy = -\frac{\mu_{lin}}{y_1 - y_0} \tag{5.22}$$

$$S_{11} = \int_{y_0}^{y_1} \mu_{lin} \partial_y p_1(y) \partial_y p_1(y) \, dy + \int_{y_1}^{y_2} \mu_{FP} \partial_y p_1(y) \partial_y p_1(y) \, dy = \frac{\mu_{lin}}{y_1 - y_0} + \frac{\mu_{FP}}{y_2 - y_1} \tag{5.23}$$

$$S_{12} = \int_{y_1}^{y_2} \mu_{FP} \partial_y p_1(y) \partial_y p_2(y) \, dy = -\frac{\mu_{FP}}{y_2 - y_1} \tag{5.24}$$

$$f_1 = -\int_{y_1}^{y_2} \big(\mu_{FP} - \mu(\Phi^{(n)})\big)\big(H^{(n)}\big) \partial_y p_1(y) \, dy = \big(\mu_{FP} - \mu(\Phi^{(n)})\big) H^{(n)} \tag{5.25}$$

with the element wise constant permeabilities μ_{lin} and μ_{FP}. Finally, the equation

$$u_1 = \frac{1}{S_{11}} \Big(f_1 - S_{10} u_0 - S_{12} u_2 \Big) \tag{5.26}$$

has to be solved for the only unknown value u_1.

5.4 Comparison of the One and the Three Dimensional Simulation

In this section the described three dimensional and one dimensional problem are simulated and compared. The one dimensional problem is simulated using MATLAB with the single unknown node. The three dimensional problem is simulated using Netgen/NGSolve [2] with the minimum of two hexahedra.

The permeability of the linear domain is $\mu_{lin} = 1000\mu_0$ with $\mu_0 := 4 \cdot 10^{-7}\pi$ as the permeability of vacuum. The nonlinear permeability of the other domain is defined by the magnetisation curve in Table 7.

H in A/m	0	1000	2000
B in T	0	$1000\mu_{lin}$	1.5

Table 7: Values for the magnetisation curve.

The fixed-point permeability μ_{FP} is set to one of the three values $\{\frac{1}{1900}, \frac{1}{1300}, \frac{1}{2500}\}\frac{Vs}{Am}$ and the results are compared. For an error estimation the L_2-norm of the solution

$$\|\Phi_h\|_2 = \sqrt{\int_\Omega \Phi_h \cdot \Phi_h d\Omega} \tag{5.27}$$

and the L_2-norm of the change in the solution $e = \|\Phi_h - \Phi_h^{(n)}\|_2$ is used. The comparison of the Φ values along the y-axis in the three dimensional model with the Φ values of the one dimensional model, yields a measure. In particular, the Φ value at the domain transition is considered, which has to be equivalent.

For this test procedure, a set of independent simulations is done, wherein the value of the Dirichlet boundary condition is changed from $\Phi_0 = 1\text{A}$ to $\Phi_0 = 2000\text{A}$ in 100 equally spaced steps. The magnetisation curve is defined in such a way that for resulting H values less then 1000A/m both domains have equal permeabilities. Consequently, the resulting Φ value at the material interface should be zero.

For resulting H values greater than 1000A/m in the nonlinear area, the relative error

$$\varepsilon = \left| \frac{\Phi(0)_{1D} - \Phi(0,0,0)_{3D}}{\Phi(0)_{1D}} \right| 100\% \tag{5.28}$$

between the 3D solution and the 1D solution is calculated. The calculated relative error for boundary values $\Phi_0 > 1000\text{A}$ is shown in Fig. 5.3. The maximal relative error is 1.55%. The relative error for boundary values $\Phi_0 < 1000\text{A}$ is neglect-able for all used fixed-point permeabilities.

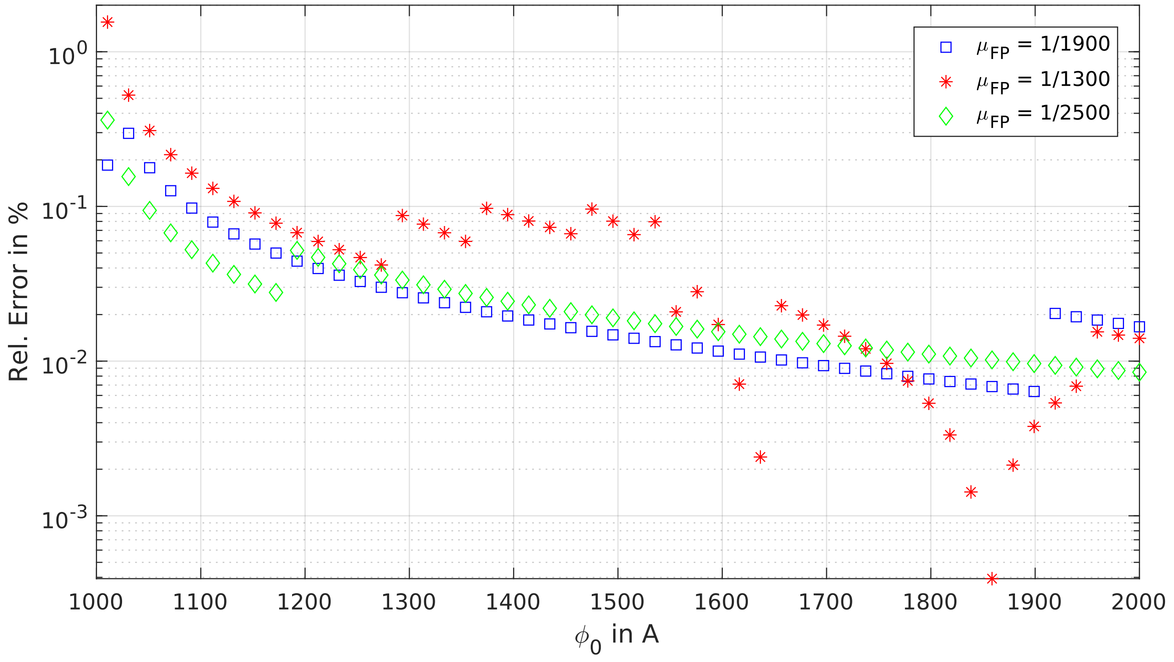

Figure 5.3: Relative error (5.28) between 3D- and 1D-model.

5.5 Variation of μ_{FP} for Three Different Magnetisation Curves

The robustness of the fixed-point method can be measured by changing

- the number of finite elements (h refinement),
- the order of the used finite element space (p refinement) or

- the value of the fixed-point permeability μ_{FP}.

Since changing the value of the fixed-point permeability μ_{FP} is the most relevant one, further investigations are carried out in this section.
For the simulation, the described BVP in Section 5.1 is solved for 20 equally spaced values of Φ_0 in the interval of $[0, 2000]$A. The value of $\mu_{FP,r} = \frac{\mu_{FP}}{\mu_0}$ is varied in 1000 equally spaced steps in the interval $\mu_{FP,r} \in [423, 10k]$. The number of finite elements is 100 in the nonlinear area and 1 in the linear area.
The robustness of the fixed-point method is examined for three different magnetisation curves. The magnetisation curves are defined as shown in Table 8, where $B_{end} \in \{1.5, 2000\mu_{lin}, 3.5265\}$T and $\mu_{lin} = 1000\mu_0$. In detail, one magnetisation curve is concave, one is linear and one is convex.

H in A/m	0	1000	2000
B in T	0	$1000\mu_{lin}$	B_{end}

Table 8: Values for the magnetisation curve.

The total number of needed iterations is considered as objective measure. Fig. 5.4 shows the simulation results. The number of iterations is the lowest for a fixed-point permeability $\mu_{FP,r} = 1000$, which is equivalent to the first grade of the polygonal magnetisation curve. Further, the simulation does not converge for fixed-point permeabilities $\mu_{FP,r} \leq 423$.

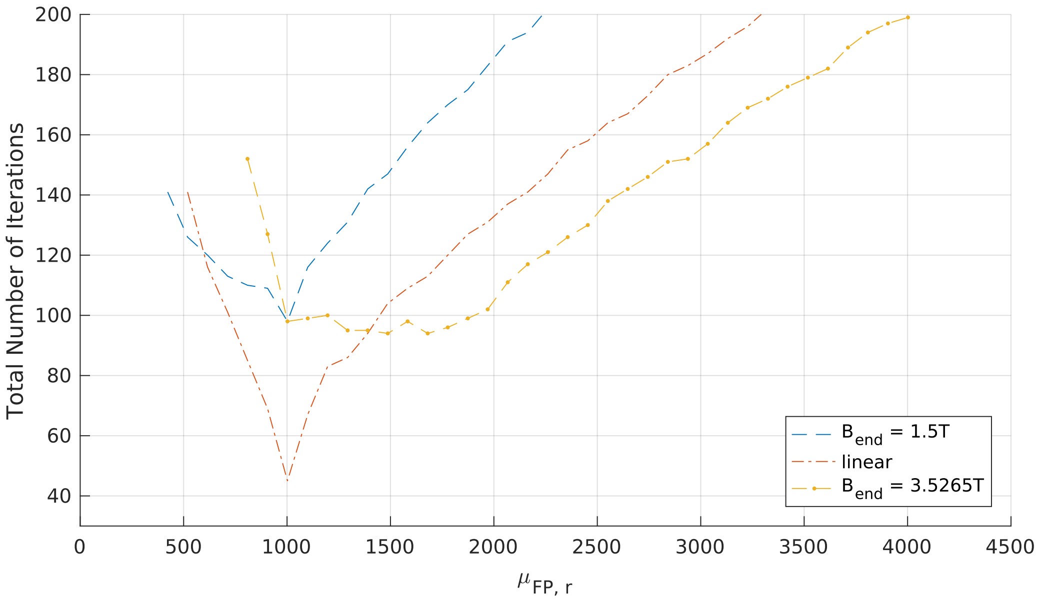

Figure 5.4: Total number of iterations with respect to the used $\mu_{FP,r}$.

5.6 Hysteresis and the Preisach Model

In the present simulations the BVP is solved using a vector Preisach model (VPM) instead of a magnetisation curve. Moreover, different fixed-point permeabilities $\overline{\overline{\mu}}^{\Delta}_{FP}$ are compared. Since the permeability of the VPM is matrix shaped, the fixed-point permeability

$$\overline{\overline{\mu}}^{\Delta}_{FP} = \begin{pmatrix} \mu^{\Delta}_{FP} & 0 & 0 \\ 0 & \mu^{\Delta}_{FP} & 0 \\ 0 & 0 & \mu^{\Delta}_{FP} \end{pmatrix} \tag{5.29}$$

has to be matrix shaped too.
First, the boundary conditions of the BVP in (5.4a) are selected in such a way that the initial magnetisation curve followed by the by the major loop is traced in 120 steps.
Since the permeability $\overline{\overline{\mu}}$ is not defined for $\mathbf{H} = \mathbf{0}$,see Section 2.9.1, the differential permeability $\overline{\overline{\mu}}^{\Delta}$ (3.30) has to be considered. Therefore, the differential BVP

$$\int_{\Omega_{lin}} \mu_{lin} \nabla\Phi^{\Delta} \cdot \nabla v \; d\Omega = 0 \qquad \text{in } \Omega_{lin} \tag{5.30a}$$

$$\int_{\Omega_{Fe}} (\overline{\overline{\mu}}^{\Delta}_{FP} \nabla\Phi^{\Delta}) \cdot \nabla v \; d\Omega = \int_{\Omega_{Fe}} (\overline{\overline{\mu}}^{\Delta}_{FP} - \overline{\overline{\mu}}^{\Delta}(\Phi))\mathbf{H}^{\Delta,(n)} \cdot \nabla v \; d\Omega \qquad \text{in } \Omega_{Fe} \tag{5.30b}$$

$$-\mathbf{n} \cdot \overline{\overline{\mu}}^{\Delta} \nabla\Phi^{\Delta} = 0 \qquad \text{on } \Gamma_{S1} \cup \Gamma_{S3} \cup \Gamma_{S5} \cup \Gamma_{S6} \tag{5.30c}$$

$$\Phi^{\Delta} = -y H_0^{\Delta} \qquad \text{on } \Gamma_{S2} \cup \Gamma_{S4} \tag{5.30d}$$

is derived, where the differential permeability $\overline{\overline{\mu}}^{\Delta}$ of the VPM, the differential scalar potential $\Phi^{\Delta} = \Phi^{(n+1)} - \Phi^{(n)}$ and the differential boundary value $H_0^{\Delta} = H_0^{(n+1)} - H_0^{(n)}$ are used. For the fixed-point method the magnetic field strength of the previous iteration $\mathbf{H}^{(n)}$ is used. The optimal value of the differential fixed-point permeability

$$\mu^{\Delta}_{FP,opt} = \frac{1}{2}(\mu^{\Delta}_{max} + \mu^{\Delta}_{min}) \tag{5.31}$$

is determined by the minimal and the maximal appearing slope in the initial magnetisation curve [15], [16].
For each tested fixed-point value $\overline{\overline{\mu}}^{\Delta}_{FP}$, the number of needed iterations is examined. The simulation results in Fig. 5.5 show that the proposed optimal value for $\overline{\overline{\mu}}^{\Delta}_{FP}$ is not optimal in terms of required iterations. However, it yields a robust algorithm. The minimal number of iterations is 257 and occurs at $\mu^{\Delta}_{FP} = 2450 \frac{Vs}{Am}$, the number of required iterations for $\mu^{\Delta}_{FP,opt}$ is 427.

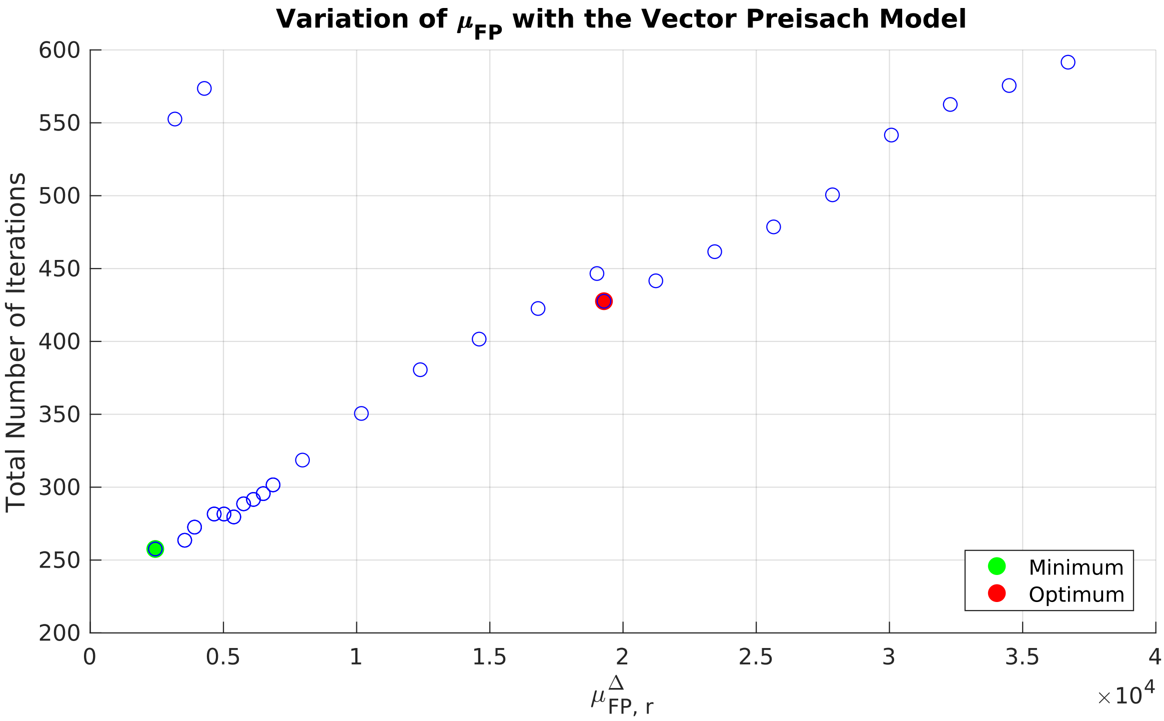

Figure 5.5: Total number of iterations with respect to the used μ^{Δ}_{FP} using the VPM.

5.7 Energy-Based Verification

To verify the model, the verification scheme shown in Fig. 1.1 is applied. The base of the verification is the linear model with a permeability $\mu_{Fe} = \frac{1.5}{1640} \frac{Vs}{Am}$. The permeability $\mu_{lin} = \mu_0$ in the first cube is the permeability of vacuum. For the verification scheme, the mean value of the magnetic energy over one period T in the iron core

$$W_H = \frac{1}{2T} \int_0^T \int_{\Omega_{Fe}} \mathbf{B} \cdot \mathbf{H} \, d\Omega \, dt \tag{5.32}$$

is used. The boundary values

$$\Phi_2^\Delta = \Phi_0 \Big(\sin\big(\omega t\big) - \sin\big(\omega(t - \Delta t)\big) \Big) \quad \text{on } \Gamma_{S2} \tag{5.33a}$$

$$\Phi_4^\Delta = -\Phi_2^\Delta \quad \text{on } \Gamma_{S4} \tag{5.33b}$$

with different amplitudes Φ_0 are applied for the BVP in (5.30). Further, the relative error

$$\varepsilon = \left| \frac{W_H - W_{H,ref}}{W_{H,ref}} \right| 100\% \tag{5.34}$$

is calculated. The reference value $W_{H,ref}$ is the linear model in the first step and the nonlinear model in the second step. Since the orientation of the magnetic field is only in one direction, a comparison with the scalar Preisach model (SPM) in the third step is valid. The results in Table 9 present the simulation outcomes of the applied verification scheme for different excitation amplitudes Φ_0. The maximal error is 1.04% and occurs for saturated materials.

Verification Step	Φ_0 in kA	W_H in W	ε in %
linear	200	68.923	ref.
differential linear	200	68.923	0
diff. lin. / nonlin.	200	68.923	0
diff. lin. / SPM	200	68.923	0
diff. lin. / VPM	200	68.923	0
diff. nonlin.	200	11.777	ref.
diff. nonlin. / SPM	200	11.699	0.66
diff. nonlin. / VPM	200	11.716	0.52
diff. SPM	200	9.797	ref.
diff. VPM	200	9.802	0.05
diff. nonlin.	400	49.190	ref.
diff. nonlin. / SPM	400	48.657	1.04
diff. nonlin. / VPM	400	48.950	0.49
diff. SPM	400	41.452	ref.
diff. VPM	400	41.364	0.21
diff. nonlin.	50	1.363	ref.
diff. nonlin. / SPM	50	1.355	0.59
diff. nonlin. / VPM	50	1.357	0.44
diff. SPM	50	1.186	ref.
diff. VPM	50	1.178	0.67

Table 9: Verification steps for the infinite plane. Abbreviations according to Fig. 1.1.

6 Ring Core

The ring core, as displayed in Fig. 6.1, displays an application of the scalar Preisach model (SPM). Since the magnetic flux in the ferromagnetic material is mainly oriented in the direction of the ring, the SPM can be used.

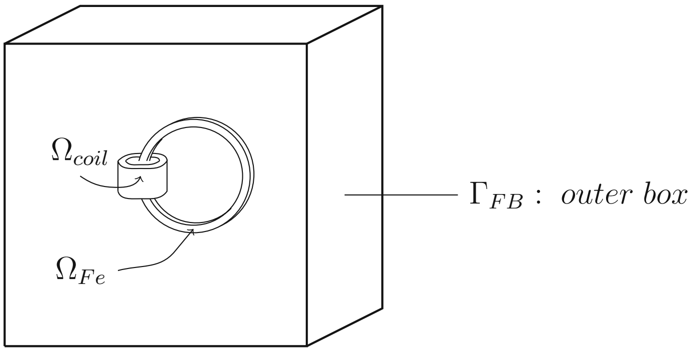

Figure 6.1: A ring core with a cylindrical coil.

The dimensions of the outer box are $W = 3$, $L = 2$ and $H = 3$. The ferromagnetic cores cross-section is 0.2 in width and is 0.1 in height. The inner radius of the core is 0.4. The coils centre is located at the point $(x, y, z) = (-0.45, 0, 0)$. Further, the coils inner radius is 0.15 and the outer radius is 0.25. The height of the coil is 0.2. The outer box defines the far boundary Γ_{FB}. The problem area $\Omega = \Omega_0 \cup \Omega_{coil} \cup \Omega_{Fe}$ consists of air, the coil and the ferromagnetic iron core.

6.1 Boundary Value Problem

Using the equations of the static magnetic field,

$$\nabla \times \mathbf{H} = \mathbf{J}_0 \tag{6.1a}$$
$$\nabla \cdot \mathbf{B} = 0, \tag{6.1b}$$

a magnetic vector potential

$$\mathbf{B} = \nabla \times \mathbf{A} \tag{6.2}$$

can be introduced. This potential fulfils Gauss's law for magnetism (6.1b) identically. The relation between the magnetic flux density and the magnetic field strength

$$\mathbf{B} = \mu \mathbf{H} \tag{6.3}$$

is defined by the permeability μ or its inverse ν. Inserting (6.2) into Ampere's law (6.1a) and considering (6.3) yields

$$\nabla \times (\nu \nabla \times \mathbf{A}) = \mathbf{J}_0, \tag{6.4}$$

where $\mathbf{J}_0$ describes the impressed current density in the coil. The current density $\mathbf{J}_0$ can be described as

$$\mathbf{J}_0 = \frac{1}{\sqrt{y^2 + (-0.45 - x)^2}} \big(y\mathbf{e}_x - (0.45 + x)\mathbf{e}_y \big). \tag{6.5}$$

For an ideal magnetic conductor ($\mu_r \to \infty$) the magnetic field in the ring would be oriented in the direction of the ring

$$\mathbf{e}_{sig} = \frac{1}{\sqrt{x^2 + z^2}}(-z\mathbf{e}_x + x\mathbf{e}_z). \tag{6.6}$$

This orientation $\mathbf{e}_{sig}$ can be used to generate a scalar input value for an inverse mode of the scalar Preisach model (iSPM) as $B_{sig} = \mathbf{B} \cdot \mathbf{e}_{sig}$ yielding the ferromagnetic material relation $\nu(\mathbf{A})$. To this end, the boundary value problem (BVP) for the given geometry in Fig. 6.1 is given by

$$\begin{aligned}
\nabla \times (\nu_0 \nabla \times \mathbf{A}) &= \mathbf{J}_0 && \text{in } \Omega_{coil} && (6.7a)\\
\nabla \times \big(\nu(\mathbf{A}) \nabla \times \mathbf{A}\big) &= \mathbf{0} && \text{in } \Omega_{Fe} && (6.7b)\\
\nabla \times (\nu_0 \nabla \times \mathbf{A}) &= \mathbf{0} && \text{in } \Omega_0 && (6.7c)\\
\mathbf{A} \times \mathbf{n} &= \mathbf{0} && \text{on } \Gamma_{FB}. && (6.7d)
\end{aligned}$$

6.1.1 Weak Formulation with the Vector Potential A

For the weak formulation

$$\int_\Omega \nabla \times (\nu \nabla \times \mathbf{A}) \cdot \mathbf{v} \, d\Omega = \int_{\Omega_{coil}} \mathbf{J}_0 \cdot \mathbf{v} \, d\Omega, \tag{6.8}$$

equation (6.7a) is first multiplied by a vectorial test function $\mathbf{v}$ and then integrated over the domain Ω. The vector identity

$$\nabla \cdot \big(\nu(\nabla \times \mathbf{A}) \times \mathbf{v}\big) \equiv \big(\nabla \times (\nu \nabla \times \mathbf{A})\big) \cdot \mathbf{v} - (\nu \nabla \times \mathbf{A}) \cdot (\nabla \times \mathbf{v}) \tag{6.9}$$

allows to rewrite the integrand as

$$\int_\Omega \nabla \cdot \big(\nu(\nabla \times \mathbf{A}) \times \mathbf{v}\big) + \nu \nabla \times \mathbf{A} \cdot \nabla \times \mathbf{v} \, d\Omega = \int_{\Omega_{coil}} \mathbf{J}_0 \cdot \mathbf{v} \, d\Omega. \tag{6.10}$$

Considering Gauss' theorem leads to

$$\int_\Omega \nu \nabla \times \mathbf{A} \cdot \nabla \times \mathbf{v} \, d\Omega = \int_{\Omega_{coil}} \mathbf{J}_0 \cdot \mathbf{v} \, d\Omega - \int_\Gamma \mathbf{n} \cdot \big(\nu(\nabla \times \mathbf{A}) \times \mathbf{v}\big) \, d\Gamma. \tag{6.11}$$

With the permutation of the triple product $\mathbf{a} \cdot (\mathbf{b} \times \mathbf{c}) = \mathbf{c} \cdot (\mathbf{a} \times \mathbf{b})$ this yields

$$\int_\Omega \nu \nabla \times \mathbf{A} \cdot \nabla \times \mathbf{v} \, d\Omega = \int_{\Omega_{coil}} \mathbf{J}_0 \cdot \mathbf{v} \, d\Omega - \int_\Gamma \mathbf{v} \cdot \big(\mathbf{n} \times \nu(\nabla \times \mathbf{A})\big) \, d\Gamma. \tag{6.12}$$

Since the test function $\mathbf{v}$ vanishes at Dirichlet boundaries Γ_D and no Neumann boundaries occur,

$$\int_\Omega \nu \nabla \times \mathbf{A} \cdot \nabla \times \mathbf{v} \, d\Omega = \int_{\Omega_{coil}} \mathbf{J}_0 \cdot \mathbf{v} \, d\Omega \tag{6.13}$$

represents, in combination with the boundary condition in (6.7d), the weak formulation of the BVP with the magnetic vector potential $\mathbf{A}$.

For the sake of uniqueness an additional regularisation term

$$\int_\Omega \nu \nabla \times \mathbf{A} \cdot \nabla \times \mathbf{v} \, d\Omega + \varepsilon \int_\Omega \mathbf{A} \cdot \mathbf{v} \, d\Omega = \int_{\Omega_{coil}} \mathbf{J}_0 \cdot \mathbf{v} \, d\Omega, \tag{6.14}$$

with a $\varepsilon > 0$, has to be added [17, p. 74].

6.2 Differential Approach

In ferromagnetic materials the permeability μ is not defined properly for all cases. Especially in case of the magnetic remanence ($B = B_R, H = 0$) the permeability is not defined. Analogously, its inverse ν is not defined for the magnetic coercivity ($H = H_C, B = 0$). Therefore, the differential weak formulation

$$\partial_t \int_\Omega \underbrace{\nu \nabla \times \mathbf{A}}_{\mathbf{H}} \cdot \nabla \times \mathbf{v} \, d\Omega + \varepsilon \partial_t \int_\Omega \mathbf{A} \cdot \mathbf{v} \, d\Omega = \partial_t \int_{\Omega_{coil}} \mathbf{J}_0 \cdot \mathbf{v} \, d\Omega \tag{6.15a}$$

$$\int_\Omega \underbrace{\frac{\partial \mathbf{H}}{\partial \mathbf{B}}}_{\nu^\partial \approx \nu^\Delta} \frac{\partial \mathbf{B}}{\partial t} \cdot \nabla \times \mathbf{v} \, d\Omega + \varepsilon \partial_t \int_\Omega \mathbf{A} \cdot \mathbf{v} \, d\Omega = \partial_t \int_{\Omega_{coil}} \mathbf{J}_0 \cdot \mathbf{v} \, d\Omega \tag{6.15b}$$

is derived, by carrying out the time derivative. Using the differential magnetic reluctivity ν^Δ, the differential vector potential $\mathbf{A}^{\Delta,(n+1)} = \frac{1}{\Delta t}\left(\mathbf{A}^{(n+1)} - \mathbf{A}^{(n)}\right)$ and the differential excitation $\mathbf{J}_0^{\Delta,(n+1)} = \frac{1}{\Delta t}\left(\mathbf{J}_0^{(n+1)} - \mathbf{J}_0^{(n)}\right)$ in the $(n+1)$-th time instance leads to

$$\int_\Omega \nu^\Delta \nabla \times \mathbf{A}^{\Delta,(n+1)} \cdot \nabla \times \mathbf{v} \, d\Omega + \varepsilon \int_\Omega \mathbf{A}^{\Delta,(n+1)} \cdot \mathbf{v} \, d\Omega = \int_{\Omega_{coil}} \mathbf{J}_0^{\Delta,(n+1)} \cdot \mathbf{v} \, d\Omega. \tag{6.16}$$

The differential magnetic reluctivity is defined in every case.

6.3 Fixed-Point Method

To solve the nonlinear problem (6.16) the fixed-point method

$$\int_{\Omega_{coil}} \nu_0 \nabla \times \mathbf{A}^\Delta \cdot \nabla \times \mathbf{v} \, d\Omega + \varepsilon \int_{\Omega_{coil}} \mathbf{A}^\Delta \cdot \mathbf{v} \, d\Omega = \int_{\Omega_{coil}} \mathbf{J}_0^\Delta \cdot \mathbf{v} \, d\Omega \qquad \text{in } \Omega_{coil} \tag{6.17a}$$

$$\begin{aligned} \int_{\Omega_{Fe}} \nu_{FP} \nabla \times \mathbf{A}^\Delta \cdot \nabla \times \mathbf{v} \, d\Omega + \varepsilon \int_{\Omega_{Fe}} \mathbf{A}^\Delta \cdot \mathbf{v} \, d\Omega = & \\ \int_{\Omega_{Fe}} (\nu_{FP} - \nu^\Delta) \nabla \times \mathbf{A}^{\Delta,(n)} \cdot \nabla \times \mathbf{v} \, d\Omega & \end{aligned} \qquad \text{in } \Omega_{Fe} \tag{6.17b}$$

$$\int_{\Omega_0} \nu_0 \nabla \times \mathbf{A}^\Delta \cdot \nabla \times \mathbf{v} \, d\Omega + \varepsilon \int_{\Omega_0} \mathbf{A}^\Delta \cdot \mathbf{v} \, d\Omega = \mathbf{0} \qquad \text{in } \Omega_0 \tag{6.17c}$$

$$\mathbf{A}^\Delta \times \mathbf{n} = \mathbf{0} \qquad \text{on } \Gamma_{FB} \tag{6.17d}$$

is selected. For the sake of simplicity, the superscript $(n+1)$ for the unknown time instant has been omitted. The reluctivity of vacuum is denoted by ν_0. The selected fixed-point value ν_{FP}^Δ is set as the inverse of (5.31). Using $\mathbf{A}^{\Delta,(n+1)} = \frac{1}{\Delta t}\big(\mathbf{A}^{(n+1)} - \mathbf{A}^{(n)}\big)$ and multiplying by Δt yields

$$\begin{aligned}
&\int_{\Omega_{coil}} \nu_0 \nabla\times\mathbf{A}^{(n+1)}\cdot\nabla\times\mathbf{v}\,d\Omega + \varepsilon\int_{\Omega_{coil}} \mathbf{A}^{(n+1)}\cdot\mathbf{v}\,d\Omega \\
&\qquad = \int_{\Omega_{coil}} \nu_0 \nabla\times\mathbf{A}^{(n)}\cdot\nabla\times\mathbf{v}\,d\Omega + \varepsilon\int_{\Omega_{coil}} \mathbf{A}^{(n)}\cdot\mathbf{v}\,d\Omega + \int_{\Omega_{coil}} \mathbf{J}_0^{\Delta}\cdot\mathbf{v}\,d\Omega \qquad \text{in } \Omega_{coil}
\end{aligned} \tag{6.18a}$$

$$\begin{aligned}
&\int_{\Omega_c} \nu_{FP} \nabla\times\mathbf{A}^{(n+1)}\cdot\nabla\times\mathbf{v}\,d\Omega + \varepsilon\int_{\Omega_c} \mathbf{A}^{(n+1)}\cdot\mathbf{v}\,d\Omega \\
&\qquad = \int_{\Omega_c} (\nu_{FP} - \nu^{\Delta})\nabla\times\big(\mathbf{A}^{(n)} - \mathbf{A}^{(n-1)}\big)\cdot\nabla\times\mathbf{v}\,d\Omega \qquad \text{in } \Omega_{Fe} \\
&\qquad\quad + \int_{\Omega_c} \nu_{FP} \nabla\times\mathbf{A}^{(n)}\cdot\nabla\times\mathbf{v}\,d\Omega + \varepsilon\int_{\Omega_c} \mathbf{A}^{(n)}\cdot\mathbf{v}\,d\Omega
\end{aligned} \tag{6.18b}$$

$$\begin{aligned}
&\int_{\Omega_0} \nu_0 \nabla\times\mathbf{A}^{(n+1)}\cdot\nabla\times\mathbf{v}\,d\Omega + \varepsilon\int_{\Omega_0} \mathbf{A}^{(n+1)}\cdot\mathbf{v}\,d\Omega \\
&\qquad = \int_{\Omega_0} \nu^{\Delta} \nabla\times\mathbf{A}^{(n)}\cdot\nabla\times\mathbf{v}\,d\Omega + \varepsilon\int_{\Omega_0} \mathbf{A}^{(n)}\cdot\mathbf{v}\,d\Omega \qquad \text{in } \Omega_0
\end{aligned} \tag{6.18c}$$

$$\mathbf{A}^{(n+1)}\times\mathbf{n} = \mathbf{0} \qquad \text{on } \Gamma_{FB}. \tag{6.18d}$$

6.4 Energy-Based Verification

To verify the model, the verification scheme shown in Fig. 1.1 is applied. Since no analytic solution is known, the verification is based on the linear model with a linear permeability $\mu = \frac{1.5}{1640}\frac{Vs}{Am}$. For the verification steps with linear material relations, the magnetic energy

$$W_H = \int_{\Omega_{Fe}} \frac{\mathbf{B}\cdot\mathbf{B}}{2\mu}\,d\Omega \tag{6.19}$$

based on (2.62) can be applied.
In the verification steps using a nonlinear material relation, the energy

$$W_H = \int_{\Omega_{Fe}} w(|\mathbf{B}|)\,d\Omega \tag{6.20}$$

with (2.61a) as energy density $w(|\mathbf{B}|)$ in the iron core is compared.
The verification of simulations with hysteresis against a simulation using a nonlinear material relation based on the according initial magnetisation curve is based on (2.63). The magnetic energy is then calculated as

$$W_H = \int_{\Omega_{Fe}} \frac{\mathbf{B}\cdot\mathbf{H}}{2}\,d\Omega. \tag{6.21}$$

However, the verification is only valid as long as the input signal increases, since in this case both models follow the initial magnetisation curve.

The simulations are computed with a Lorentzian Everett function (EF), see Section 2.2.2, with a number of $N_A = 601$ discretisation steps discretised by the adaptive discretisation algorithm. The maximal input fields are set to $H_{max} = 1640$A/m and $B_{max} = 1.5$T.

The current density in the coil

$$\mathbf{J}_{coil}(t) = J(t)\mathbf{J}_0 \tag{6.22}$$

is zero initially. Further, the value $J(t)$ is increased up to the value J_{max} in N equidistant steps, decreased to $-J_{max}$ and finally increased to J_{max} again. For an error estimation, the pure linear model and the differential nonlinear model are used as reference models. Moreover, the mean values

$$W_H = \frac{1}{N}\sum_{i=0}^{N} W_H, i \tag{6.23}$$

are used to calculate the relative error ε (5.34). Table 10 shows the calculated energies and the corresponding relative errors. All relative errors are less than 0.03%. Figure 6.2 outlines the occurring vector fields **H** and **J** in the ring core.

Verification Step	J_{max} in kA/m^2	W_H in W	ε in %
linear	80	2.948	ref.
differential linear	80	2.948	0
diff. lin. / non.-lin.	80	2.948	0
diff. lin. / iSPM	80	2.947	0.03
diff. nonlin.	80	1.008	ref.
diff. nonlin. / iSPM	80	1.008	0.02
diff. iSPM	80	2.900	-

Table 10: Verification steps for the ring core problem. Abbreviations according to Fig. 1.1.

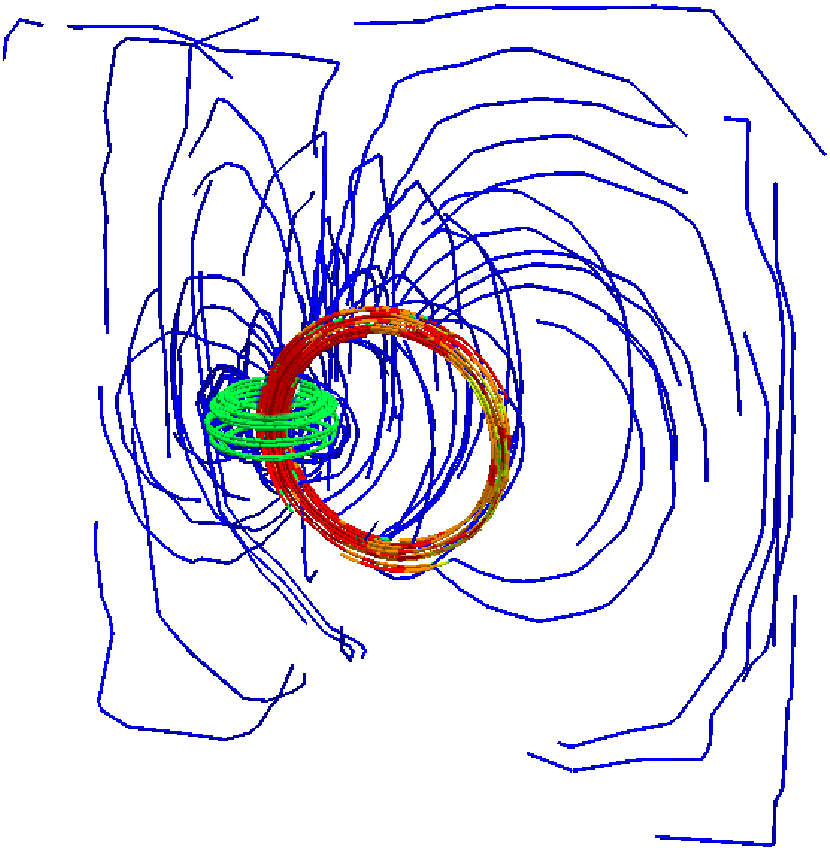

Figure 6.2: Illustration of the occurring vector fields **H** (red/blue) and **J** (green) in the ring core.

7 Static Magnetic Field in an L-Shape Problem

In this section, a comparison of different simulation approaches for a filamentary current in a geometry with two domains for the static magnetic field is presented. All simulations correspond to the different levels of the verification scheme in Fig. 1.1.
The problem shown in Fig. 7.1 is denoted by L-Shape problem and represents an eight of a full geometry, consisting of two iron layers, by utilising its symmetries. Figure 7.1 presents the geometry and the boundary conditions for the simulations. The filamentary current is placed in the centre of the symmetrical L-shaped iron sheet. For the specific dimensions see Fig. 7.2. The far boundary $\Gamma_{FB} = \Gamma_{S3} \cup \Gamma_{S4} \cup \Gamma_{S6}$ is defined as Dirichlet boundary for all simulation approaches.
The three different simulation approaches are

- the fixed-point method, which varies the load vector,
- the Bíró-Preis approach, which varies the stiffness matrix and
- an energy minimisation approach.

Additionally, the filamentary current is considered in two different ways.

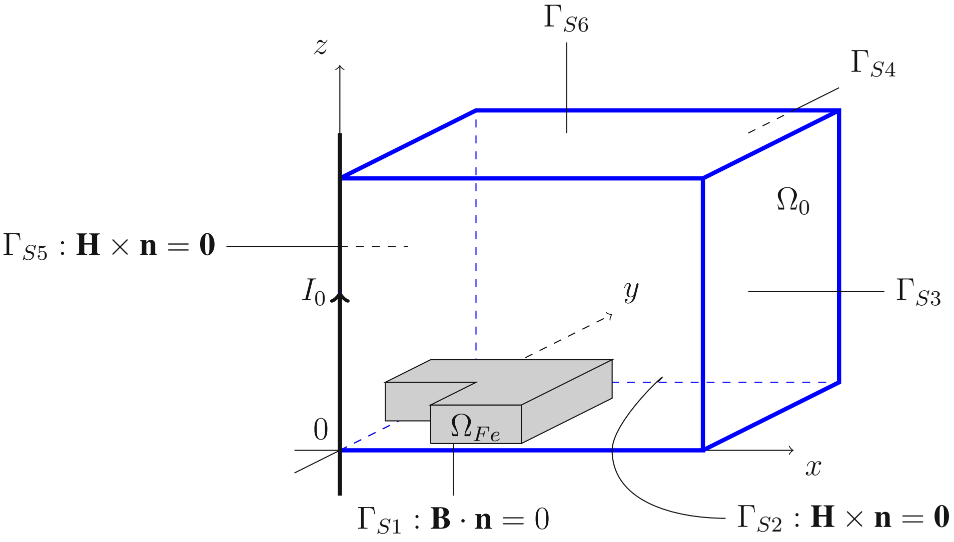

Figure 7.1: boundary value problem (BVP) of a L-shaped core with a filamentary current I_0 and the boundary conditions.

7.1 Defining the Boundary Values

For an infinitely long filamentary current the magnetic field strength is given as

$$\begin{aligned} \mathbf{H}_{BS}(\mathbf{r}) &= H_{BS}(\mathbf{r})\mathbf{e}_H && (7.1)\\ &= \frac{I_0}{2\pi|\mathbf{r}|}\mathbf{e}_I \times \mathbf{e}_r, && (7.2) \end{aligned}$$

which is derived from (4.2). For the given geometry, with the filamentary current $\mathbf{I}_0 = I_0\mathbf{e}_z$ and therefore $|\mathbf{r}| = \sqrt{x^2 + y^2}$, the known magnetic field strength $\mathbf{H}_{BS}$ equals

$$\mathbf{H}_{BS}(\mathbf{r}) = \frac{I_0}{2\pi(x^2 + y^2)}(-y\mathbf{e}_x + x\mathbf{e}_y), \tag{7.3}$$

which has a vanishing rotation $\nabla \times \mathbf{H}_{BS} = \mathbf{0}$.

7.1.1 Magnetic Vector Potential Formulation

The magnetic vector potential $\mathbf{A}$ is defined by

$$\mathbf{B} = \nabla \times \mathbf{A} \tag{7.4}$$

and fulfils Gauss' law for magnetism ($\nabla \cdot \mathbf{B} = 0$) identically. The definition for a far boundary is that only the Biot-Savart field $\mathbf{H}_{BS}$ of the filamentary current exists. Therefore, the vector potential of the Biot-Savart field has to fulfil the inhomogeneous boundary conditions $\mathbf{n} \cdot \mathbf{B} = \mathbf{n} \cdot \mu_0 \mathbf{H}_{BS}$ at the surfaces S_3, S_4 and S_6. The tangential component of the according vector potential $\mathbf{A}_0$ has to be defined. For the surface S_3 in Fig. 7.1, with its normal vector $\mathbf{n} = \mathbf{e}_x$, the boundary condition is defined by the equation

$$\mathbf{e}_x \cdot \nabla \times \mathbf{A} = \mathbf{e}_x \cdot \mu_0 \mathbf{H}_{BS} \tag{7.5}$$

or further

$$\partial_y A_z - \partial_z A_y = -\frac{\mu_0 I_0}{2\pi(x^2+y^2)} y. \tag{7.6}$$

Analogously, for S_4 with its normal vector $\mathbf{n} = \mathbf{e}_y$, the boundary condition is defined by the equation

$$\partial_z A_x - \partial_x A_z = \frac{\mu_0 I_0}{2\pi(x^2+y^2)} x \tag{7.7}$$

and for S_6, with the normal vector $\mathbf{n} = \mathbf{e}_z$, by

$$\partial_x A_y - \partial_y A_x = 0. \tag{7.8}$$

Solving the system of differential equations yields

$$\mathbf{A} \times \mathbf{n} = -\frac{\mu_0 I_0 \log(x^2+y^2)}{4\pi} \mathbf{e}_z \tag{7.9}$$

which fulfils the boundary conditions on S_3, S_4 and S_6.
Homogeneous Dirichlet boundary conditions are valid on S_1 and homogeneous Neumann boundary conditions are valid on S_2 and S_5.

7.1.2 Magnetic Scalar Potential Formulation

The magnetic field strength $\mathbf{H} = \mathbf{H}_{BS} - \nabla\Phi$, which is using the magnetic scalar potential Φ, is a superposition of the Biot-Savart field $\mathbf{H}_{BS}$ and the negative gradient $-\nabla\Phi$ of the magnetic scalar potential. The homogeneous boundary condition

$$-(\mu \mathbf{H}_{BS} - \mu\nabla\Phi) \cdot \mathbf{e}_z = 0 \tag{7.10}$$

on S_1 leads, with $\mu \mathbf{H}_{BS} \cdot \mathbf{e}_z = 0$, to a homogeneous Neumann boundary condition. The boundary conditions at S_2 and S_5 are homogeneous Dirichlet conditions. The Inhomogeneous Dirichlet boundary conditions on the far boundary Γ_{FB} are fulfilled by $\Phi = 0$.

7.2 Magnetic Vector Potential - Resolved Filamentary Current

In the first step, the filamentary current is modelled as an explicit current density in the finite element method (FEM) model. Therefore, all finite elements adjacent to the z-axis are carrying a current density

$$\mathbf{J}_0 = \frac{I_0}{4A}\mathbf{e}_z \tag{7.11}$$

with the impressed current I_0 and the element cross-section A of the element. The resulting domain is denoted by Ω_{con}. Moreover, the Maxwell equations for the static magnetic field

$$\nabla \times \mathbf{H} = \mathbf{J}_0 \tag{7.12a}$$
$$\nabla \cdot \mathbf{B} = 0 \tag{7.12b}$$

are considered. The magnetic vector potential $\mathbf{B} = \nabla \times \mathbf{A}$ solves Gauss's law (7.12b) identically. Taking into account the nonlinear material relation

$$\mathbf{H} = \nu(\mathbf{A})\mathbf{B} \tag{7.13}$$

and considering the introduced boundary values (7.9), the BVP

$$\nabla \times \big(\nu(\mathbf{A})\nabla \times \mathbf{A}\big) = \mathbf{0} \qquad \text{in } \Omega_{Fe} \tag{7.14a}$$
$$\nabla \times (\nu_0 \nabla \times \mathbf{A}) = \mathbf{0} \qquad \text{in } \Omega_0 \tag{7.14b}$$
$$\nabla \times (\nu_0 \nabla \times \mathbf{A}) = \mathbf{J}_0 \qquad \text{in } \Omega_{con} \tag{7.14c}$$
$$\mathbf{A} \times \mathbf{n} = \mathbf{0} \qquad \text{on } \Gamma_{S1} \tag{7.14d}$$
$$\mathbf{A} \times \mathbf{n} = -\frac{\mu_0 I_0 \log(x^2+y^2)}{4\pi}\mathbf{e}_z \qquad \text{on } \Gamma_{S3} \cup \Gamma_{S4} \cup \Gamma_{S6} \tag{7.14e}$$
$$(\nu_0 \nabla \times \mathbf{A}) \times \mathbf{n} = \mathbf{0} \qquad \text{on } \Gamma_{S2} \cup \Gamma_{S5} \tag{7.14f}$$

is obtained.

7.2.1 Weak Formulation

Applying the weak formulation analogously to Section 6.1.1 with the vector identity (6.9) yields

$$\int_\Omega \nu \nabla \times \mathbf{A} \cdot \nabla \times \mathbf{v} \, d\Omega + \int_\Gamma \mathbf{n} \cdot (\nu \nabla \times \mathbf{A} \times \mathbf{v}) \, d\Gamma = \int_\Omega \mathbf{J}_0 \cdot \mathbf{v} \, d\Omega. \tag{7.15}$$

Thereby, Gauss's theorem is used.
Since the test function $\mathbf{v}$ vanishes at Dirichlet boundaries $\Gamma_D = \Gamma_{S1} \cup \Gamma_{S3} \cup \Gamma_{S4} \cup \Gamma_{S6}$ and the value of the magnetic vector potential on the Neumann boundaries $\Gamma_N = \Gamma_{S2} \cup \Gamma_{S5}$ is zero, the according surface integral is zero.

Finally, the weak formulation of the BVP (7.14a) reads as

$$\int_{\Omega_{Fe}} \nu(\mathbf{A}) \nabla \times \mathbf{A} \cdot \nabla \times \mathbf{v} \, d\Omega + \varepsilon \int_{\Omega_{Fe}} \mathbf{A} \cdot \mathbf{v} \, d\Omega = \mathbf{0} \qquad \text{in } \Omega_{Fe} \tag{7.16a}$$
$$\int_{\Omega_0} \nu_0 \nabla \times \mathbf{A} \cdot \nabla \times \mathbf{v} \, d\Omega + \varepsilon \int_{\Omega_0} \mathbf{A} \cdot \mathbf{v} \, d\Omega = \mathbf{0} \qquad \text{in } \Omega_0 \tag{7.16b}$$
$$\int_{\Omega_{con}} \nu_0 \nabla \times \mathbf{A} \cdot \nabla \times \mathbf{v} \, d\Omega + \varepsilon \int_{\Omega_{con}} \mathbf{A} \cdot \mathbf{v} \, d\Omega = \int_{\Omega_{con}} \mathbf{J}_0 \cdot \mathbf{v} \, d\Omega \qquad \text{in } \Omega_{con} \tag{7.16c}$$

with the boundary conditions (7.14d) to (7.14f) and a small $\varepsilon > 0$ for the regularisation.

7.2.2 Fixed-Point Method

For solving the nonlinear material behaviour the fixed-point method is applied. With a fixed-point reluctivity ν_{FP} the equations

$$\int_{\Omega_0} \nu_0 \nabla \times \mathbf{A} \cdot \nabla \times \mathbf{v} \, d\Omega + \varepsilon \int_{\Omega_0} \mathbf{A} \cdot \mathbf{v} \, d\Omega = \mathbf{0} \qquad \text{in } \Omega_0 \qquad (7.17a)$$

$$\int_{\Omega_{Fe}} \nu_{FP} \nabla \times \mathbf{A} \cdot \nabla \times \mathbf{v} \, d\Omega + \varepsilon \, \cdots = \int_{\Omega_{Fe}} \big(\nu_{FP} - \nu(\mathbf{A})\big) \mathbf{B}^{(n)} \cdot \nabla \times \mathbf{v} \, d\Omega \qquad \text{in } \Omega_{Fe} \qquad (7.17b)$$

$$\int_{\Omega_{con}} \nu_0 \nabla \times \mathbf{A} \cdot \nabla \times \mathbf{v} \, d\Omega + \varepsilon \int_{\Omega_{con}} \mathbf{A} \cdot \mathbf{v} \, d\Omega = \int_{\Omega_{con}} \mathbf{J}_0 \cdot \mathbf{v} \, d\Omega \qquad \text{in } \Omega_{con} \qquad (7.17c)$$

at the $(n+1)$-th iteration are to be solved. The value $\mathbf{B}^{(n)}$ is the magnetic flux density of the previous solution. The boundary conditions are (7.14d) to (7.14f).

7.3 Magnetic Vector Potential - Biot-Savart Field of the Filamentary Current

With the magnetic vector potential (7.4), the magnetic field strength $\mathbf{H}$ is a superposition of the known Biot-Savart field $\mathbf{H}_{BS}$ (7.3) and a disturbance $\nu \nabla \times \mathbf{A}$ caused by the iron sheet.
Under consideration of the material relation (7.13), Ampere's law (7.12a) can be written as

$$\nabla \times (\nu \nabla \times \mathbf{A}) = -\nabla \times \mathbf{H}_{BS} \qquad (7.18)$$

where $\mathbf{H}_{BS}$ represents the Biot-Savart field of the filamentary current (7.3).

7.3.1 Weak Formulation

Applying the weak formulation analogously to Section 6.1.1 with the vector identity (6.9) and using

$$\mathbf{v} \cdot (\nabla \times \mathbf{H}_{BS}) = \mathbf{H}_{BS} \cdot (\nabla \times \mathbf{v}) + \nabla \cdot (\mathbf{H}_{BS} \times \mathbf{v}) \qquad (7.19)$$

yields

$$\begin{aligned} &\int_{\Omega} \nu \nabla \times \mathbf{A} \cdot \nabla \times \mathbf{v} \, d\Omega + \int_{\Gamma} \mathbf{n} \cdot (\nu \nabla \times \mathbf{A} \times \mathbf{v}) \, d\Gamma \\ &\qquad = -\int_{\Omega} \mathbf{H}_{BS} \cdot \nabla \times \mathbf{v} \, d\Omega - \int_{\Gamma} \mathbf{n} \cdot (\mathbf{H}_{BS} \times \mathbf{v}) \, d\Gamma. \end{aligned} \qquad (7.20)$$

Thereby, Gauss's theorem is used. Since the test function $\mathbf{v}$ vanishes at Dirichlet boundaries $\Gamma_D = \Gamma_{S1} \cup \Gamma_{S3} \cup \Gamma_{S4} \cup \Gamma_{S6}$ and the value of the magnetic vector potential on the Neumann boundaries $\Gamma_N = \Gamma_{S2} \cup \Gamma_{S5}$ is zero, the according terms are zero. The weak formulation

$$\int_{\Omega_{Fe}} \nu \nabla \times \mathbf{A} \cdot \nabla \times \mathbf{v} \, d\Omega + \varepsilon \int_{\Omega_{Fe}} \mathbf{A} \cdot \mathbf{v} \, d\Omega = -\int_{\Omega_{Fe}} \mathbf{H}_{BS} \cdot \nabla \times \mathbf{v} \, d\Omega \qquad \text{in } \Omega_{Fe} \qquad (7.21a)$$

$$\int_{\Omega_0} \nu_0 \nabla \times \mathbf{A} \cdot \nabla \times \mathbf{v} \, d\Omega + \varepsilon \int_{\Omega_0} \mathbf{A} \cdot \mathbf{v} \, d\Omega = -\int_{\Omega_0} \mathbf{H}_{BS} \cdot \nabla \times \mathbf{v} \, d\Omega \qquad \text{in } \Omega_0 \qquad (7.21b)$$

includes the necessary regularisation term with a small $\varepsilon > 0$. The according boundary conditions are (7.14d) to (7.14f).

7.3.2 Fixed-Point Method

If nonlinear material relations occur, the iterative fixed-point method is used. With a fixed-point reluctivity ν_{FP} the equations

$$\int_{\Omega_0} \nu_0 \nabla\times\mathbf{A}\cdot\nabla\times\mathbf{v}\, d\Omega + \varepsilon\int_{\Omega_0}\mathbf{A}\cdot\mathbf{v}\, d\Omega = -\int_{\Omega_0}\mathbf{H}_{BS}\cdot\nabla\times\mathbf{v}\, d\Omega \qquad \text{in } \Omega_0 \tag{7.22a}$$

$$\begin{aligned}\int_{\Omega_{Fe}} \nu_{FP}\nabla\times\mathbf{A}\cdot\nabla\times\mathbf{v}\, d\Omega + \varepsilon\int_{\Omega_{Fe}}\mathbf{A}\cdot\mathbf{v}\, d\Omega & \\ = -\int_{\Omega_{Fe}}\mathbf{H}_{BS}\cdot\nabla\times\mathbf{v}\, d\Omega + \int_{\Omega_{Fe}}(\nu_{FP}-\nu)\mathbf{B}^{(n)}\cdot\nabla\times\mathbf{v}\, d\Omega & \end{aligned} \qquad \text{in } \Omega_{Fe} \tag{7.22b}$$

at the $(n+1)$-th iteration are to be solved. The value $\mathbf{B}^{(n)}$ is the magnetic flux density of the solution in the (n)-th step. The boundary conditions are (7.14d) to (7.14f).

Energy Minimisation The weak formulation of an partial differential equation can in some cases be derived from a minimisation problem

$$\min_{\mathbf{x}\in\mathbb{R}^{(n)}} F(\mathbf{x}). \tag{7.23}$$

With the magnetic energy density (2.61a), the magnetic energy

$$F(\mathbf{A}) = \int_\Omega w(|\nabla\times\mathbf{A}|)\, d\Omega - \int_\Omega \mathbf{J}_0\cdot\mathbf{A}\, d\Omega \tag{7.24}$$

can be used as the functional $F(\mathbf{x})$ [18]. In a stationary solution of (7.23) the functional

$$\frac{d}{d\eta}F(\mathbf{A}) = \lim_{\eta\to 0}\frac{F(\mathbf{A}+\eta\mathbf{v}) - F(\mathbf{A})}{\eta} \tag{7.25}$$

with a solution $\mathbf{A}$ has to be zero for every direction $\mathbf{v}$ with $|\mathbf{v}| = 1$. Applying the functional (7.25) to the magnetic energy density function (2.61a) yields

$$\frac{d}{d\eta}w\big(|\nabla\times(\mathbf{A})|\big) = w'\big(|\nabla\times(\mathbf{A}+\eta\mathbf{v})|\big)\frac{\nabla\times(\mathbf{A}+\eta\mathbf{v})}{|\nabla\times(\mathbf{A}+\eta\mathbf{v})|}\cdot\nabla\times\mathbf{v} \tag{7.26}$$

where the chain rule $\frac{\partial}{\partial\eta}w(|\xi|) = \frac{\partial}{\partial\xi}w(|\xi|)\frac{\xi}{|\xi|}\cdot\frac{\partial}{\partial\eta}\xi$ is applied. Therefore, the minimisation problem (7.23) with the functional (7.24)

$$\frac{d}{d\eta}F(\mathbf{A}) = \int_\Omega w'\big(|\nabla\times(\mathbf{A}+\eta\mathbf{v})|\big)\frac{\nabla\times(\mathbf{A}+\eta\mathbf{v})}{|\nabla\times(\mathbf{A}+\eta\mathbf{v})|}\cdot\nabla\times\mathbf{v}\, d\Omega - \frac{d}{d\eta}\int_\Omega \mathbf{J}_0\cdot(\mathbf{A}+\eta\mathbf{v})\, d\Omega \tag{7.27}$$

$$= \int_\Omega w'\big(|\nabla\times(\mathbf{A}+\eta\mathbf{v})|\big)\frac{\nabla\times(\mathbf{A}+\eta\mathbf{v})}{|\nabla\times(\mathbf{A}+\eta\mathbf{v})|}\cdot\nabla\times\mathbf{v}\, d\Omega - \int_\Omega \mathbf{J}_0\cdot\mathbf{v}\, d\Omega \tag{7.28}$$

is derived. Applying the limit of the derivation functional (7.25) with $\eta\to 0$ and finding a local minimum with $\frac{d}{d\eta}F(\mathbf{A}) = 0$ yields

$$\int_\Omega w'\big(|\nabla\times\mathbf{A}|\big)\frac{\nabla\times\mathbf{A}}{|\nabla\times\mathbf{A}|}\cdot\nabla\times\mathbf{v}\, d\Omega + \varepsilon\int_\Omega \mathbf{A}\cdot\mathbf{v}\,\Omega = \int_\Omega \mathbf{J}_0\cdot\mathbf{v}\, d\Omega, \tag{7.29}$$

which includes the regularisation term with a $\varepsilon > 0$ for a unique solution. The latter equation is equivalent to the weak formulation of the BVP and can be solved by iterative nonlinear methods like the Newton-Raphson method [18, p. 31].

7.4 Magnetic Scalar Potential - Biot-Savart Field of the Filamentary Current

Under consideration of the magnetic field intensity (7.3) of the filamentary current along the z-axis, the magnetic field intensity

$$\mathbf{H} = \mathbf{H}_{BS} - \nabla\Phi \tag{7.30}$$

is a superposition of the Biot-Savart field $\mathbf{H}_{BS}$ and a gradient field $-\nabla\Phi$. Moreover, the Maxwell equations for the static magnetic field

$$\nabla \times \mathbf{H} = \mathbf{0} \tag{7.31a}$$
$$\nabla \cdot \mathbf{B} = 0 \tag{7.31b}$$

are fulfilled since the rotation of the Biot-Savart field $\nabla \times \mathbf{H}_{BS} = \mathbf{0}$ vanishes and $\nabla \times (\nabla\Phi) \equiv 0$. With the material relation (7.13), the approach (7.30) and the introduced boundary conditions, see Section 7.1.2, the BVP

$$-\nabla \cdot \big(\mu(\Phi)\nabla\Phi\big) = -\nabla \cdot \mu(\Phi)\mathbf{H}_{BS} \qquad \text{in } \Omega_{Fe} \tag{7.32a}$$
$$-\nabla \cdot \big(\mu_0\nabla\Phi\big) = -\nabla \cdot \mu_0\mathbf{H}_{BS} \qquad \text{in } \Omega_0 \tag{7.32b}$$
$$\Phi = 0 \qquad \text{on } \Gamma_{S2} \cup \Gamma_{S3} \cup \Gamma_{S4} \cup \Gamma_{S5} \cup \Gamma_{S6} \tag{7.32c}$$
$$\mu\nabla\Phi \cdot \mathbf{n} = 0 \qquad \text{on } \Gamma_{S1} \tag{7.32d}$$

is derived.

7.4.1 Weak Formulation

Similar to the weak formulation with the magnetic vector potential $\mathbf{A}$, the BVP (7.32) is multiplied by a scalar test function v and gets integrated over the area Ω to gain the weak formulation with the magnetic scalar potential. With the vector identity

$$\nabla \cdot (v\mathbf{u}) \equiv v\nabla \cdot \mathbf{u} + \mathbf{u} \cdot \nabla v \tag{7.33}$$

the weak formulation can be written as

$$\int_\Omega \mu\nabla\Phi \cdot \nabla v - \nabla \cdot (v\mu\nabla\Phi - v\mu\mathbf{H}_{BS})\, d\Omega = \int_\Omega \mu\mathbf{H}_{BS} \cdot \nabla v\, d\Omega. \tag{7.34}$$

With the Gauss' theorem and the required vanishing of the test function at Dirichlet boundaries, this leads to

$$\int_\Omega \mu\nabla\Phi \cdot \nabla v\, d\Omega - \int_{\Gamma_N} \mathbf{n} \cdot \mu\nabla\Phi\, v\, d\Gamma = \int_\Omega \mu\mathbf{H}_{BS} \cdot \nabla v\, d\Omega - \int_{\Gamma_N} \mathbf{n} \cdot (\mu\mathbf{H}_{BS}\, v)\, d\Gamma. \tag{7.35}$$

With the homogeneous Neumann boundary condition (7.32d) and $-\mathbf{e}_z \cdot \mathbf{H}_{BS} = 0$ on $\Gamma_{S1} = \Gamma_N$, the weak formulation

$$\int_{\Omega_{Fe}} \mu(\Phi)\nabla\Phi \cdot \nabla v\, d\Omega = \int_{\Omega_{Fe}} \mu(\Phi)\mathbf{H}_{BS} \cdot \nabla v\, d\Omega \qquad \text{in } \Omega_{Fe} \tag{7.36a}$$
$$\int_{\Omega_0} \mu_0\nabla\Phi \cdot \nabla v\, d\Omega = \int_{\Omega_0} \mu_0\mathbf{H}_{BS} \cdot \nabla v\, d\Omega \qquad \text{in } \Omega_0 \tag{7.36b}$$

is gained. The boundary conditions in (7.32) remain the same.

7.4.2 Fixed-Point Method

To solve the nonlinear material relation (7.13), the iterative fixed-point method

$$\int_\Omega \mu_{FP}\nabla\Phi\cdot\nabla v\; d\Omega = \int_\Omega \mu(\Phi)\mathbf{H}_{BS}\cdot\nabla v\; d\Omega + \int_\Omega (\mu_{FP}-\mu(\Phi))\nabla\Phi^{(n)}\cdot\nabla v\; d\Omega \quad \text{on } \Omega_{Fe} \quad (7.37a)$$

$$\int_\Omega \mu_0\nabla\Phi\cdot\nabla v\; d\Omega = \int_\Omega \mu_0\mathbf{H}_{BS}\cdot\nabla v\; d\Omega \quad \text{on } \Omega_0 \quad (7.37b)$$

with the fixed-point permeability μ_{FP} and the magnetic scalar potential $\Phi^{(n)}$ of the solution in the (n)-th step is used. The fixed-point permeability is set according to (5.31).

7.4.3 Differential Approach

Since the permeability in ferromagnetic materials is not defined for certain cases, the tensor-valued approximation of the differential permeability $\overline{\overline{\mu}}^{\Delta}$ (3.30) of the vector Preisach model (VPM) has to be used. Therefore, the time derivative of (7.37) is carried out. In particular, this yields

$$\begin{aligned} -\partial_t\overline{\overline{\mu}}\nabla\Phi &= \partial_t\mathbf{B} \\ &= \frac{\partial\mathbf{B}}{\partial\mathbf{H}}\frac{\partial\mathbf{H}}{\partial t} \\ &\approx -\frac{1}{\Delta t}\overline{\overline{\mu}}^{\Delta}\nabla\Phi^{\Delta}. \end{aligned} \quad (7.38)$$

This leads with the backward Euler formula to the weak formulation of the differential BVP

$$\int_\Omega \mu_{FP}\nabla\Phi^{\Delta}\cdot\nabla v\; d\Omega = \int_\Omega \overline{\overline{\mu}}^{\Delta}\mathbf{H}^{\Delta}_{BS}\cdot\nabla v\; d\Omega + \int_\Omega (\overline{\overline{\mu}}_{FP}-\overline{\overline{\mu}}^{\Delta})\nabla\Phi^{\Delta,(n)}\cdot\nabla v\; d\Omega \quad \text{on } \Omega_{Fe} \quad (7.39)$$

$$\int_\Omega \mu_0\nabla\Phi^{\Delta}\cdot\nabla v\; d\Omega = \int_\Omega \mu_0\mathbf{H}^{\Delta}_{BS}\cdot\nabla v\; d\Omega \quad \text{on } \Omega_0, \quad (7.40)$$

which uses the differential scalar potential $\Phi^{\Delta} = \Phi^{(n+1)} - \Phi^{(n)}$ and the differential excitation $\mathbf{H}_0^{\Delta} = \mathbf{H}_0^{(n+1)} - \mathbf{H}_0^{(n)}$. Moving known terms to the right yields

$$\begin{aligned} \int_{\Omega_{Fe}} \mu_{FP}\nabla\Phi^{(n+1)}\cdot\nabla v\; d\Omega &= \int_{\Omega_{Fe}} \overline{\overline{\mu}}^{\Delta}\mathbf{H}^{\Delta}_{BS}\cdot\nabla v\; d\Omega + \int_{\Omega_{Fe}} \mu_{FP}\nabla\Phi^{(n)}\cdot\nabla v\; d\Omega \\ &\quad + \int_{\Omega_{Fe}} (\overline{\overline{\mu}}_{FP}-\overline{\overline{\mu}}^{\Delta})\nabla\Phi^{\Delta,(n)}\cdot\nabla v\; d\Omega \end{aligned} \quad \text{on } \Omega_{Fe} \quad (7.41)$$

$$\int_{\Omega_0} \mu_0\nabla\Phi^{(n+1)}\cdot\nabla v\; d\Omega = \int_{\Omega_0} \mu_0\mathbf{H}^{\Delta}_{BS}\cdot\nabla v\; d\Omega + \int_{\Omega_0} \mu_0\nabla\Phi^{(n)}\cdot\nabla v\; d\Omega \quad \text{on } \Omega_0. \quad (7.42)$$

7.5 Numerical Example

For the simulation, the dimensions outlined in Fig. 7.2 are used. Thereby, two sheets are considered and the symmetries of the problem are taken into account. The current I_0 is either considered as discrete elements or analytically as Biot-Savart field.
Beside that, the three different formulation for solving the BVP are used. Since the VPM is not implemented for the inverse mode, simulations considering hysteresis can only be executed with the magnetic scalar potential.

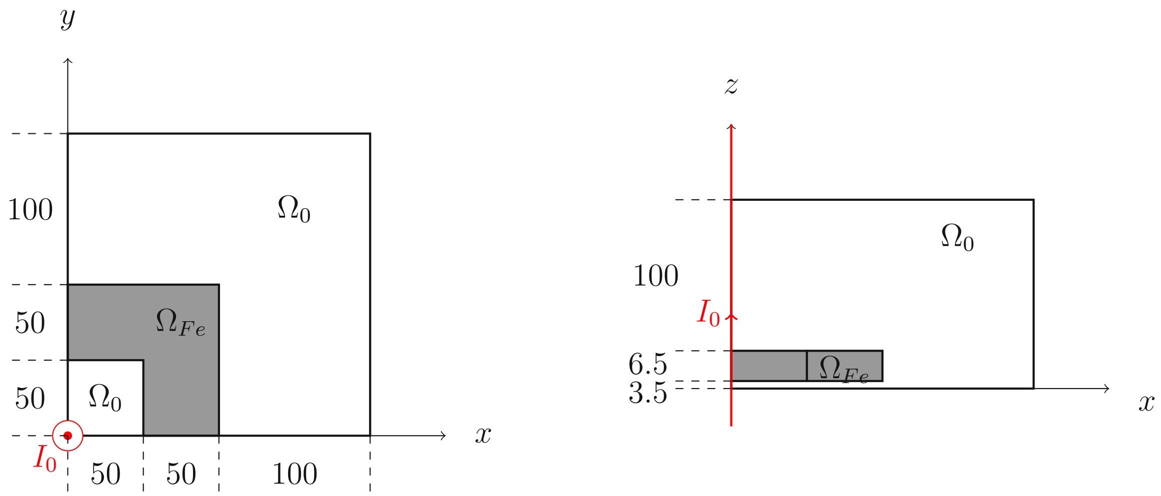

Figure 7.2: Dimensions of the L-Shape used for the simulation. All values are in mm.

The filamentary current is assumed to be $I(t) = I_{max}\sin(\omega t)$, with a fixed angular frequency $\omega = 2\pi f = 100\pi$ and a variable amplitude I_{max}. For the verification the energy in the iron

$$W_H = \frac{1}{2T}\int_{t'}^{t'+T}\int_{\Omega_{Fe}} \mathbf{B}\cdot\mathbf{H}\, d\Omega\, dt \tag{7.43}$$

over one Period $T = 1/f$ is calculated and compared by means of the relative error (5.34). The results are presented in Table 11.

Following the verification scheme, see Fig. 1.1, linear material relations are considered in the first step. The formulation using the magnetic scalar potential with an analytic filamentary current is selected as reference model. Beside the three different linear models, three reduced nonlinear models are simulated. With the reduction, the nonlinear models behave like linear models. Additionally, a simulation is done, which is based on a VPM with a bilinear Everett function (EF) (see Section 2.2.1). Therefore, a comparison of seven different linear models is possible.
The simulations result in a maximal relative error of 1.52% and occurs for the simulation using th VPM.

Formulation	Verification Step	I_{max} in A	W_H in mW	ε in %
Φ, anal. current	linear	100	0.519	ref.
A, disc. current	linear	100	0.518	0.13
A, anal. current	linear	100	0.518	0.18
A, disc. current	lin. / nonlin.	100	0.519	0.09
A, anal. current	lin. / nonlin.	100	0.520	0.22
Φ, anal. current	differential lin. / nonlin.	100	0.519	0.007
Φ, anal. current	diff. VPM / lin.	100	0.511	1.52

Table 11: Verification steps for the linear magneto-static L-shape problem with a filamentary current. Abbreviations according to Fig. 1.1.

In the second step, nonlinear material relations are taken into account. The relations are based on the initial magnetisation curve shown in Table 12.

H in A/m	0	42	53	62	70	79	88	100	113	132	157	193	255	376	677	1624	90168
B in T	0	0.1	0.2	0.3	0.4	0.5	0.6	0.7	0.8	0.9	1.0	1.1	1.2	1.3	1.4	1.5	10

Table 12: Values for the magnetisation curve.

The simulations are executed using the introduces approaches to solve the nonlinearity. Table 13 summarises the results. Beside the specification of the used approach, the amplitude of the electric current, the magnetic energy (7.43) and the calculated relative error (5.34) are presented.

Further, the value N_{steps} represents the length of the input sequence which sets the current state of the current I_0. The value t_{pI} equals the quotient of the total simulation time and the number of input values N_{steps}. The simulation is calculated for a duration of $t_{end} = 1.25$.

Formulation	Verification Step	I_{max} in A	W_H in mW	ε in %	N_{steps}	t_{pI} in s
Φ, anal. cur.	nonlin.	100	2.355	ref.	125	0.25
Φ, anal. cur.	diff nonlin., Linear interp.	100	2.385	1.26	125	0.23
Φ, anal. cur.	diff, nonlin., BSpline, FP	100	2.360	0.22	125	0.43
$\mathbf{A}$, disc. cur.	diff nonlin.	100	2.285	2.97	1750	1.33
$\mathbf{A}$, anal. cur.	nonlin, Energy min.	100	2.33	1.24	250	1.96
$\mathbf{A}$, disc. cur.	nonlin, Energy min.	100	2.366	0.48	75	2.64
Φ, anal. cur.	diff, VPM / nonlin.	100	2.372	0.74	125	4.46

Table 13: Various implementations for the nonlinear magneto-static L-shape problem with a filamentary current.

The results in Table 13 outline the functionality of the used algorithms and approaches. The maximum relative error is 4.46% and occurs for the simulation using the VPM.

8 Eddy Current Problem

There are only little physically meaningful applications for simulations of the quasi-static magnetic field. However, simulating eddy current problems (ECPs), shown in Fig. 8.1, is of huge interest for electric devices like transformers or electric machines. The ECP couples a static magnetic field in an electrically non-conducting domain Ω_0 with a quasi-static magnetic field in an electrically conducting domain Ω_c.
Since the vector Preisach model (VPM) is implemented for the forward mode only, the ECP can not be solved, using the magnetic vector potential **A**. This approach would need an inverse mode of the vector Preisach model (iVPM). Therefore, an alternative approach with the current vector potential (CVP) $\boldsymbol{T}$ and the magnetic scalar potential (MSP) Φ in terms of the $\boldsymbol{T}, \Phi$-Φ formulation is applied [19], [20].

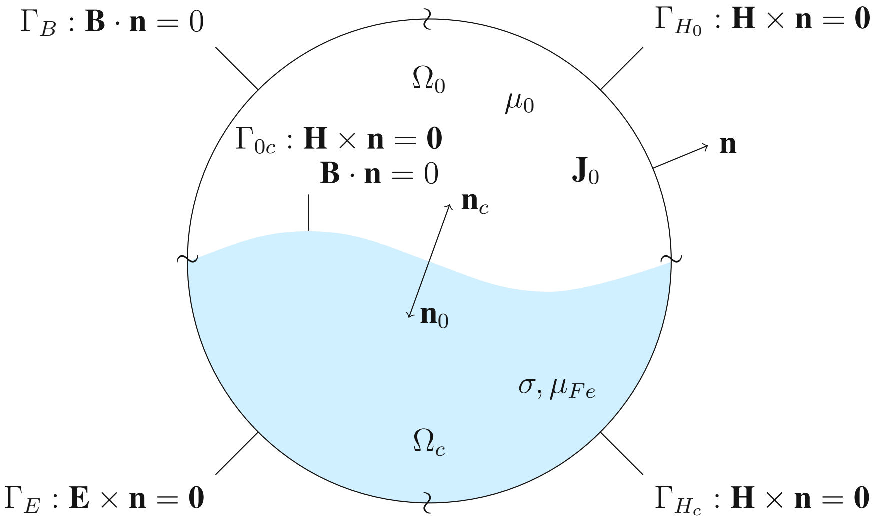

Figure 8.1: The boundary value problem (BVP) of an ECP.

8.1 Boundary Value Problem

The problem is based on the Maxwell equations for the quasi static magnetic field

$$\nabla\times\mathbf{H} = \mathbf{J}+\mathbf{J}_0 \tag{8.1a}$$
$$\nabla\times\mathbf{E} = -\partial_t\mathbf{B} \tag{8.1b}$$
$$\nabla\cdot\mathbf{B} = 0 \tag{8.1c}$$

in Ω_c and the Maxwell equations for the static magnetic field

$$\nabla\times\mathbf{H} = \mathbf{J}_0 \tag{8.2a}$$
$$\nabla\cdot\mathbf{B} = 0 \tag{8.2b}$$

in Ω_0 with the material relations

$$\mathbf{B} = \mu\mathbf{H} \tag{8.3a}$$
$$\mathbf{J} = \sigma\mathbf{E}, \qquad \mathbf{E} = \rho\mathbf{J} \quad . \tag{8.3b}$$

The vector field $\mathbf{J}$ describes the eddy currents and $\mathbf{J}_0$ an excitation, for instance a rectangular current loop or electric coils. The boundary conditions of the problem are assumed to be

$$\mathbf{H} \times \mathbf{n} = \mathbf{0} \quad \text{on } \Gamma_{H_c} \tag{8.4a}$$
$$\mathbf{E} \times \mathbf{n} = \mathbf{0} \quad \text{on } \Gamma_{E} \tag{8.4b}$$
$$\mathbf{H} \times \mathbf{n} = \mathbf{0} \quad \text{on } \Gamma_{H_0} \tag{8.4c}$$
$$\mathbf{B} \cdot \mathbf{n} = 0 \quad \text{on } \Gamma_{B} \tag{8.4d}$$

and the interface conditions on Γ_{0c} are

$$\mathbf{H} \times \mathbf{n} = \mathbf{0} \tag{8.5a}$$
$$\mathbf{B} \cdot \mathbf{n} = 0. \tag{8.5b}$$

Since the divergence of Ampere's law (8.1a) $\nabla \cdot (\mathbf{J} + \mathbf{J}_0) = \nabla \cdot \nabla \times \mathbf{H}$ is identically equal to zero, the approach

$$\mathbf{J} + \mathbf{J}_0 = \nabla \times (\boldsymbol{T} + \boldsymbol{T}_{BS}) \tag{8.6}$$

can be applied. The CVP $\boldsymbol{T}_{BS}$ may either represent a known Biot-Savart-field, see Section 4. Comparing Ampere's law (8.1a) and (8.6),

$$\nabla \times \mathbf{H} = \nabla \times (\boldsymbol{T} + \boldsymbol{T}_{BS}) \tag{8.7}$$

yields

$$\mathbf{H} = \boldsymbol{T} + \boldsymbol{T}_{BS} - \nabla\Phi \tag{8.8}$$

with a reduced magnetic scalar potential Φ. The potentials $\boldsymbol{T}$ and Φ describe the quasi-static field in the conducting domain.

8.1.1 Non-Conduction Domain Ω_0

The reduced approach in air is

$$\mathbf{H} = \boldsymbol{T}_{BS} - \nabla\Phi. \tag{8.9}$$

Considering (8.9) and (8.3a)

$$-\nabla \cdot (\mu_0 \nabla\Phi) = -\nabla \cdot (\mu_0 \boldsymbol{T}_{BS}) \tag{8.10}$$

is obtained. The boundary conditions $\mathbf{B} \cdot \mathbf{n} = 0$ and $\mathbf{H} \times \mathbf{n} = \mathbf{0}$ on the boundaries Γ_B and Γ_{H_0} transform into

$$-\mu\nabla\Phi \cdot \mathbf{n} = -\mu\boldsymbol{T}_{BS} \cdot \mathbf{n} \quad \text{on } \Gamma_B \tag{8.11a}$$
$$\Phi = 0 \quad \text{on } \Gamma_{H_0} \tag{8.11b}$$

using (8.9).

8.1.2 Conducting Domain Ω_c

The approach (8.8) and (8.3b) in Ampere's law (8.1a) yield

$$\rho\nabla \times \boldsymbol{T} + \rho\nabla \times \boldsymbol{T}_{BS} = \mathbf{E}, \tag{8.12}$$

Further, Faraday's law (8.1b) results in

$$\begin{aligned}\nabla \times (\rho \nabla \times \boldsymbol{T}) + \nabla \times (\rho \nabla \times \boldsymbol{T}_{BS}) &= -\partial_t \mu \mathbf{H} && (8.13a)\\ &= -\partial_t \mu (\boldsymbol{T}_{BS} + \boldsymbol{T} - \nabla \Phi). && (8.13b)\end{aligned}$$

Moreover, moving known terms to the right and unknown terms to the left leads to

$$\nabla \times (\rho \nabla \times \boldsymbol{T}) + \partial_t \mu \boldsymbol{T} - \partial_t \mu \nabla \Phi = -\nabla \times (\rho \nabla \times \boldsymbol{T}_{BS}) - \partial_t \mu \boldsymbol{T}_{BS}. \tag{8.14}$$

Finally, using the approach (8.8), Gauss law of magnetism (8.1c) in the conducting domain is equivalent to

$$\nabla \cdot (\mu \boldsymbol{T}_{BS} + \mu \boldsymbol{T} - \mu \nabla \Phi) = 0, \tag{8.15}$$

which can be written as

$$-\nabla \cdot \mu \nabla \Phi + \nabla \cdot \mu \boldsymbol{T} = -\nabla \cdot \mu \boldsymbol{T}_{BS}, \tag{8.16}$$

where the known excitation is moved to the right side. The boundary conditions on Γ_E are

$$\mathbf{E} \times \mathbf{n} = \mathbf{0} \rightarrow (\rho \nabla \times \boldsymbol{T}) \times \mathbf{n} = -(\rho \nabla \times \boldsymbol{T}_{BS}) \times \mathbf{n} \tag{8.17}$$

$$\mathbf{B} \cdot \mathbf{n} = 0 \rightarrow \mu (\boldsymbol{T} - \nabla \Phi) \cdot \mathbf{n} = -\mu \boldsymbol{T}_{BS} \cdot \mathbf{n} \tag{8.18}$$

and on Γ_{H_c}

$$\mathbf{H} \times \mathbf{n} = \mathbf{0} \rightarrow \boldsymbol{T} \times \mathbf{n} = -\boldsymbol{T}_{BS} \times \mathbf{n} (= \mathbf{0}), \Phi = 0, \tag{8.19}$$

respectively.

8.1.3 Interface Conditions on Γ_{0c}

The required interface conditions on Γ_{0c} are

$$\mathbf{B} \cdot \mathbf{n}_c + \mathbf{B} \cdot \mathbf{n}_0 = 0 \tag{8.20}$$

and

$$\mathbf{H} \times \mathbf{n}_c + \mathbf{H} \times \mathbf{n}_0 = 0, \tag{8.21}$$

leading to

$$\mu (\boldsymbol{T} - \nabla \Phi) \cdot \mathbf{n}_c - \mu_0 \nabla \Phi \cdot \mathbf{n}_0 = -\mu \boldsymbol{T}_{BS} \cdot \mathbf{n}_c - \mu_0 \boldsymbol{T}_{BS} \cdot \mathbf{n}_0 \tag{8.22}$$

and

$$\boldsymbol{T} \times \mathbf{n}_c = \mathbf{0}, \tag{8.23}$$

respectively.

To summarise, the BVP with the mixed $\boldsymbol{T}, \Phi$-Φ formulation for the quasi-static magnetic field is described by

$$\begin{aligned} \nabla \times (\rho \nabla \times \boldsymbol{T}) + \partial_t \mu \boldsymbol{T} - \partial_t \mu \nabla \Phi &= -\nabla \times (\rho \nabla \times \boldsymbol{T}_{BS}) - \partial_t \mu \boldsymbol{T}_{BS}, \\ -\nabla \cdot \mu \nabla \Phi + \nabla \cdot \mu \boldsymbol{T} &= -\nabla \cdot \mu \boldsymbol{T}_{BS} \end{aligned} \qquad \text{in } \Omega_c \tag{8.24a}$$

$$\begin{aligned} \boldsymbol{T} \times \mathbf{n} &= \mathbf{0}, \\ \Phi &= 0 \end{aligned} \qquad \text{on } \Gamma_{H_c} \tag{8.24b}$$

$$\begin{aligned} (\rho \nabla \times \boldsymbol{T}) \times \mathbf{n} &= -(\rho \nabla \times \boldsymbol{T}_{BS}) \times \mathbf{n}, \\ \mu(\boldsymbol{T} - \nabla \Phi) \cdot \mathbf{n} &= -\mu \boldsymbol{T}_{BS} \cdot \mathbf{n} \end{aligned} \qquad \text{on } \Gamma_E. \tag{8.24c}$$

The static magnetic field is described by

$$-\nabla \cdot (\mu_0 \nabla \Phi) = -\nabla \cdot (\mu_0 \boldsymbol{T}_{BS}) \qquad \text{in } \Omega_0 \tag{8.25a}$$

$$-\mu \nabla \Phi \cdot \mathbf{n} = -\mu \boldsymbol{T}_{BS} \cdot \mathbf{n} \qquad \text{on } \Gamma_B \tag{8.25b}$$

$$\Phi = 0 \qquad \text{on } \Gamma_{H_0}. \tag{8.25c}$$

The interface conditions on Γ_{0c} are

$$\begin{aligned} \mu(\boldsymbol{T} - \nabla \Phi) \cdot \mathbf{n}_c - \mu_0 \nabla \Phi \cdot \mathbf{n}_0 &= -\mu \boldsymbol{T}_{BS} \cdot \mathbf{n}_c - \mu_0 \boldsymbol{T}_{BS} \cdot \mathbf{n}_0 \\ \boldsymbol{T} \times \mathbf{n}_c &= \mathbf{0} \end{aligned} \qquad \text{on } \Gamma_{0c}. \tag{8.26}$$

8.2 Weak Formulation

Multiplying the first equation in (8.24a) with a vector test function $\boldsymbol{T}'$, integrating over Ω_c and carrying out integration by parts leads to

$$\begin{aligned} &\int_{\Omega_c} \rho \nabla \times \boldsymbol{T} \cdot \nabla \times \boldsymbol{T}' \, d\Omega + \oint_{\Gamma_c} \big((\rho \nabla \times \boldsymbol{T}) \times \boldsymbol{T}'\big) \cdot \mathbf{n} \, d\Gamma + \partial_t \int_{\Omega_c} \mu(\boldsymbol{T} - \nabla \Phi) \cdot \boldsymbol{T}' \, d\Omega \\ &= -\int_{\Omega_c} \rho \nabla \times \boldsymbol{T}_{BS} \cdot \nabla \times \boldsymbol{T}' \, d\Omega - \oint_{\Gamma_c} \big((\rho \nabla \times \boldsymbol{T}_{BS}) \times \boldsymbol{T}'\big) \cdot \mathbf{n} \, d\Gamma \\ &\quad - \partial_t \int_{\Omega_c} \mu \boldsymbol{T}_{BS} \cdot \boldsymbol{T}' \, d\Omega, \end{aligned} \tag{8.27}$$

where $\Gamma_c = \Gamma_E \cup \Gamma_{H_c} \cup \Gamma_{0c}$. Considering the boundary conditions in (8.24b), (8.24c), (8.26) and $\boldsymbol{T}' \times \mathbf{n} = \mathbf{0}$ on $\Gamma_{H_c} \cup \Gamma_{0c}$ the surface integrals in (8.27) vanish [19]. Multiplying the second equation in (8.24a) and (8.25a), respectively, with a scalar test function Φ', integrating over $\Omega = \Omega_c \cup \Omega_0$ and carrying out integration by parts leads to

$$\begin{aligned} \int_{\Omega} \mu \nabla \Phi \cdot \nabla \Phi' \, d\Omega - \oint_{\Gamma} \mu \nabla \Phi \Phi' \cdot \mathbf{n} \, d\Gamma - \int_{\Omega_c} \mu \boldsymbol{T} \cdot \nabla \Phi' \, d\Omega + \oint_{\Gamma_c} \mu \boldsymbol{T} \cdot \mathbf{n} \Phi' \, d\Gamma \\ = \int_{\Omega} \mu \boldsymbol{T}_{BS} \cdot \nabla \Phi' \, d\Omega - \oint_{\Gamma} \mu \boldsymbol{T}_{BS} \Phi' \cdot \mathbf{n} \, d\Gamma. \end{aligned} \tag{8.28}$$

Considering the boundary conditions (8.25c), (8.24b), (8.26) and $\Phi' = 0$ on $\Gamma_{H_0}, \Gamma_{Hc}, \Gamma_{0c}$, surface integrals in (8.28) vanish [19].

To obtain a symmetric finite element (FE)-system of the mixed formulation, the time derivative of

(8.28) is used resulting in

$$\begin{aligned}\int_{\Omega_c} \rho \nabla \times \boldsymbol{T} \cdot \nabla \times \boldsymbol{T}' \, d\Omega + \partial_t \int_{\Omega_c} \mu (\boldsymbol{T} - \nabla \Phi) \cdot \boldsymbol{T}' \, d\Omega \\ = - \int_{\Omega_c} \rho \nabla \times \boldsymbol{T}_{BS} \cdot \nabla \times \boldsymbol{T}' \, d\Omega - \partial_t \int_{\Omega_c} \mu \boldsymbol{T}_{BS} \cdot \boldsymbol{T}' \, d\Omega\end{aligned} \tag{8.29a}$$

and

$$\partial_t \int_{\Omega} \mu \nabla \Phi \cdot \nabla \Phi' \, d\Omega - \partial_t \int_{\Omega_c} \mu \boldsymbol{T} \cdot \nabla \Phi' \, d\Omega = \partial_t \int_{\Omega} \mu \boldsymbol{T}_{BS} \cdot \nabla \Phi' \, d\Omega. \tag{8.29b}$$

8.3 Differential Approach

Since the permeability μ is not defined for any case, see Section 2.9.1, the approximation of the differential permeability $\overline{\overline{\mu}}^{\Delta}$ (3.30) is considered. Therefore, the time derivative, for instance, in (8.29a) is rewritten leading to

$$\begin{aligned}\int_{\Omega_c} \partial_t \big(\mu (\boldsymbol{T} - \nabla \Phi + \boldsymbol{T}_{BS})\big) \cdot \boldsymbol{T}' \, d\Omega &= \int_{\Omega_c} \partial_t \mathbf{B} \cdot \boldsymbol{T}' \, d\Omega \\ &= \int_{\Omega_c} \frac{\partial \mathbf{B}}{\partial \mathbf{H}} \frac{\partial \mathbf{H}}{\partial t} \cdot \boldsymbol{T}' \, d\Omega \qquad . \\ &\approx \frac{1}{\Delta t} \int_{\Omega_c} \overline{\overline{\mu}}^{\Delta} \big(\mathbf{H}^{(n+1)} - \mathbf{H}^{(n)}\big) \cdot \boldsymbol{T}' \, d\Omega\end{aligned} \tag{8.30}$$

Applying the backward Euler method to (8.29) and considering (8.30) yields

$$\begin{aligned}\Delta t \int_{\Omega_c} \rho \nabla \times \boldsymbol{T}^{(n+1)} \cdot \nabla \times \boldsymbol{T}' \, d\Omega + \int_{\Omega_c} \overline{\overline{\mu}}^{\Delta} (\boldsymbol{T}^{\Delta} - \nabla \Phi^{\Delta}) \cdot \boldsymbol{T}' \, d\Omega \\ = - \int_{\Omega_c} \overline{\overline{\mu}}^{\Delta} \boldsymbol{T}^{\Delta}_{BS} \cdot \boldsymbol{T}' \, d\Omega\end{aligned} \qquad \text{in } \Omega_c \tag{8.31}$$

and

$$\int_{\Omega_0} \mu_0 \nabla \Phi^{\Delta} \cdot \nabla \Phi' \, d\Omega = \int_{\Omega_0} \mu_0 \boldsymbol{T}^{\Delta}_{BS} \cdot \nabla \Phi' \, d\Omega \qquad \text{in } \Omega_0 \tag{8.32a}$$

$$\int_{\Omega_c} \overline{\overline{\mu}}^{\Delta} \big(\nabla \Phi^{\Delta} - \boldsymbol{T}^{\Delta}\big) \cdot \nabla \Phi' \, d\Omega = \int_{\Omega_c} \overline{\overline{\mu}}^{\Delta} \boldsymbol{T}^{\Delta}_{BS} \cdot \nabla \Phi' \, d\Omega \qquad \text{in } \Omega_c. \tag{8.32b}$$

with the differential potentials $\boldsymbol{T}^{\Delta} = \boldsymbol{T}^{(n+1)} - \boldsymbol{T}^{(n)}$, $\Phi^{\Delta} = \Phi^{(n+1)} - \Phi^{(n)}$ and the differential version of the excitation $\boldsymbol{T}^{\Delta}_{BS} = \boldsymbol{T}^{(n+1)}_{BS} - \boldsymbol{T}^{(n)}_{BS}$. The double bar indicates that the differential magnetic permeability $\overline{\overline{\mu}}^{\Delta}$ is tensor-valued. The rotation of the Biot-Savart field of the excitation is considered to vanish.

8.4 Solving the Nonlinearity

To solve the problem due to the nonlinear material relation $\mu(\mathbf{B})$, the fixed-point method is applied. The relative error of two subsequent solutions in the fixed-point iteration $\frac{\|(\boldsymbol{T}^{k+1} - \nabla \Phi^{k+1}) - (\boldsymbol{T}^{k} - \nabla \Phi^{k})\|^2_{2,\Omega_c}}{\|\boldsymbol{T}^{k+1} - \nabla \Phi^{k+1}\|^2_{2,\Omega_c}} < \varepsilon$ with a small ε is used as convergence criterion. Using the fixed-point permeability μ_{FP} according to (5.31), (8.31) and (8.32) yield

$$\begin{aligned}\Delta t \int_{\Omega_c} \rho \nabla \times \boldsymbol{T}^{(n+1)} \cdot \nabla \times \boldsymbol{T}' \, d\Omega + \int_{\Omega_c} \mu_{FP} (\boldsymbol{T}^{\Delta} - \nabla \Phi^{\Delta}) \cdot \boldsymbol{T}' \, d\Omega & \\ = - \int_{\Omega_c} \overline{\overline{\mu}}^{\Delta} \boldsymbol{T}_{BS}^{\Delta} \cdot \boldsymbol{T}' \, d\Omega + \int_{\Omega_c} \left(\overline{\overline{\mu}}_{FP} - \overline{\overline{\mu}}^{\Delta} \right) \left(\boldsymbol{T}^{\Delta,(n)} - \nabla \Phi^{\Delta,(n)} \right) \cdot \boldsymbol{T}' \, d\Omega & \qquad \text{in } \Omega_c \end{aligned} \tag{8.33}$$

and

$$\int_{\Omega_0} \mu_0 \nabla \Phi^{\Delta} \cdot \nabla \Phi' \, d\Omega = \int_{\Omega_0} \mu_0 \boldsymbol{T}_{BS}^{\Delta} \cdot \nabla \Phi' \, d\Omega \qquad \text{in } \Omega_0 \tag{8.34a}$$

$$\begin{aligned}\int_{\Omega_c} \mu_{FP} \left(\nabla \Phi^{\Delta} - \boldsymbol{T}^{\Delta} \right) \cdot \nabla \Phi' \, d\Omega = \int_{\Omega_c} \overline{\overline{\mu}}^{\Delta} \boldsymbol{T}_{BS}^{\Delta} \cdot \nabla \Phi' \, d\Omega & \\ + \int_{\Omega_c} \left(\overline{\overline{\mu}}_{FP} - \overline{\overline{\mu}}^{\Delta} \right) \left(\nabla \Phi^{\Delta,(n)} - \boldsymbol{T}^{\Delta,(n)} \right) \cdot \nabla \Phi' \, d\Omega & \qquad \text{in } \Omega_c . \end{aligned} \tag{8.34b}$$

The potentials $\boldsymbol{T}^{\Delta,(n)} = \boldsymbol{T}^{(n)} - \boldsymbol{T}^{(n-1)}$ and $\Phi^{\Delta,(n)} = \Phi^{(n)} - \Phi^{(n-1)}$ belong to the (n)-th and $(n-1)$-th time instances. In an additional step, known values, i.e. all values from the (n)-th time instant in the differential potentials, on the left side of the equations can be moved to the right side.

8.5 Frequency Domain

For linear material relations and harmonic excitations, the complex representation can be used. Therefore, the fields are written as $\tilde{\underline{\mathbf{F}}}(\mathbf{x}, t) = \underline{\mathbf{F}}(\mathbf{x}) e^{-j\omega t}$. The underlining bar denotes complex values. The parameters ω and j denote the angular frequency and the imaginary unit $j^2 = -1$. Consequently, the time derivative $\frac{d}{dt} \tilde{\underline{\mathbf{F}}}(\mathbf{x}, t)$ yields $-j\omega \underline{\mathbf{F}}(\mathbf{x}) e^{-j\omega t}$.
Hence the weak formulation (8.29) results in

$$\begin{aligned}\int_{\Omega_c} \rho \nabla \times \underline{\boldsymbol{T}} \cdot \nabla \times \underline{\boldsymbol{T}}' \, d\Omega + j\omega \int_{\Omega_c} \mu (\underline{\boldsymbol{T}} - \nabla \underline{\Phi}) \cdot \underline{\boldsymbol{T}}' \, d\Omega & \\ = - \int_{\Omega_c} \rho \nabla \times \underline{\boldsymbol{T}}_{BS} \cdot \nabla \times \underline{\boldsymbol{T}}' \, d\Omega - j\omega \int_{\Omega_c} \mu \underline{\boldsymbol{T}}_{BS} \cdot \underline{\boldsymbol{T}}' \, d\Omega & \end{aligned} \tag{8.35a}$$

and

$$j\omega \int_{\Omega} \mu \nabla \underline{\Phi} \cdot \nabla \underline{\Phi}' \, d\Omega - j\omega \int_{\Omega_c} \mu \underline{\boldsymbol{T}} \cdot \nabla \underline{\Phi}' \, d\Omega = j\omega \int_{\Omega} \mu \underline{\boldsymbol{T}}_{BS} \cdot \nabla \underline{\Phi}' \, d\Omega . \tag{8.35b}$$

The solutions $\underline{\mathbf{H}} = \underline{\boldsymbol{T}} - \nabla \underline{\Phi} + \underline{\boldsymbol{T}}_{BS}$ and $\underline{\mathbf{J}} = \nabla \times \underline{\boldsymbol{T}}$ should agree with the steady-state solutions of (8.29) obtained by the time-stepping method with time harmonic excitation.

8.6 Numerical Example

The ECP with the L-shaped core consisting of four sheets in Fig. 8.2 is studied.

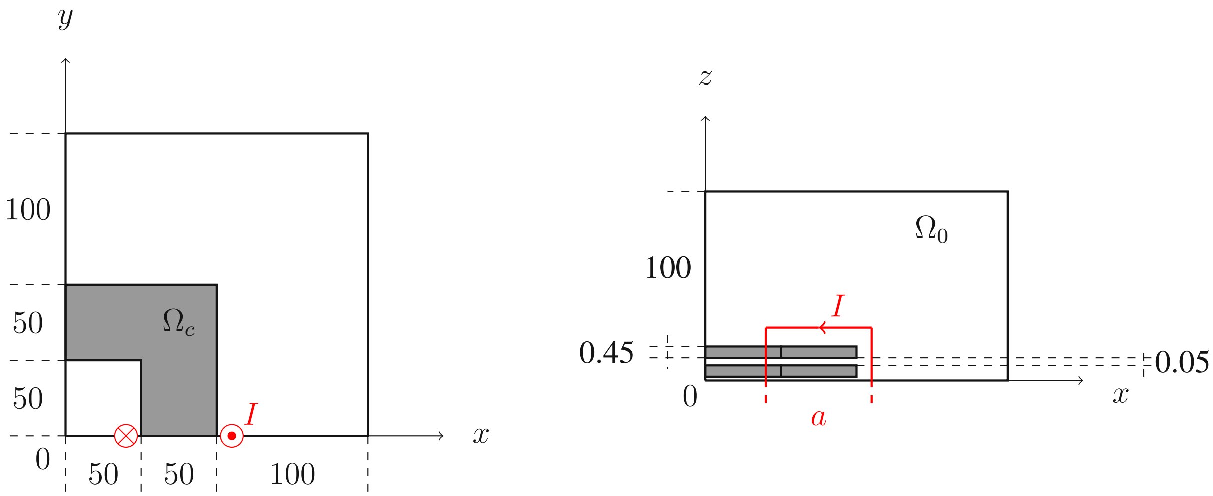

Figure 8.2: L-shaped core with a quadratic current loop (red). The origin of the coordinate system is denoted by 0.

The excitation is considered by the Biot-Savart field of the quadratic current loop. Du to the symmetry, only one eighth has been considered. The side length of the current loop is $a = 70$mm. The maximum of the impressed sinusoidal current is denoted by I_{max} with the frequency set to $f = 50$Hz. Since the impressed current is time harmonic, the verification scheme can be based on the complex analysis with linear material relations [4], [19].
To verify simulations with (8.31) and (8.32), the temporal mean value of the magnetic energy-based functional (3.35)

$$W_H = \frac{1}{T}\int_{t'}^{t'+T}\int_{\Omega_c}\frac{\mu}{2}\mathbf{H}\cdot\mathbf{H}\,d\Omega\,dt \tag{8.36}$$

and that of the losses due to eddy currents

$$P = \frac{1}{T}\int_{t'}^{t'+T}\int_{\Omega_c}\frac{1}{\sigma}\mathbf{J}\cdot\mathbf{J}\,d\Omega\,dt, \tag{8.37}$$

where T denotes the period in time are compared with

$$W_H = \frac{1}{2}\int_{\Omega_c}\frac{\mu}{2}\underline{\mathbf{H}}\cdot\underline{\mathbf{H}}^*\,d\Omega \quad \text{and} \quad P = \frac{1}{2}\int_{\Omega_c}\frac{1}{\sigma}\underline{\mathbf{J}}\cdot\underline{\mathbf{J}}^*\,d\Omega, \tag{8.38}$$

respectively. Next, the relative errors

$$\varepsilon_H = \left|\frac{W_H - W_{H,ref}}{W_{H,ref}}\right|100\% \qquad \text{and} \qquad \varepsilon_E = \left|\frac{P - P_{ref}}{P_{ref}}\right|100\% \tag{8.39}$$

of the solutions are calculated. The electric conductivities in iron and in air are set to typical values $\sigma_{Fe} = 2\cdot 10^6$S/m and $\sigma_0 = 1\cdot 10^{-4}$S/m.

Table 14 presents the verification steps according to Fig. 1.1. The solution calculated in the frequency domain sets the initial linear reference solution. Based on that, the direct linear and the differential linear solution are verified. Additionally, the differential fixed-point method with a linear magnetisation curve and the differential fixed-point method using the VPM with a bilinear Everett function, see Section 2.2.1, are verified. The maximal error is less than 0.2%.

For the verification of simulations with nonlinear material relations, the magnetisation curve of an Everett function (EF) based on an arctangent function, see Section 2.2.2, with $N_A = 701$ discretisation steps, $H_{max} = 1640$A/m and $B_{max} = 1.5$T and an adaptive discretisation of the Preisach plane is used. The verification without hysteresis phenomenon yields an maximal error of 5%. In comparison with the results published in [4] the relative error in the eddy current losses is 3.82%.

The eddy current losses for an excitation amplitude of $I_0 = 75$A and nonlinear materials or materials with hysteresis are shown in Fig. 8.3 and Fig. 8.4, respectively. The excitation with 75A yields a highly saturated material.

Results in terms of the magnetic fields and the eddy currents are shown in Fig. 8.5.

Verification Step	I_{max} in A	W_H in μW	ε_H in %	P in mW	ε_E in %
complex	10	2.8	ref.	0.023	ref.
linear	10	2.8	0	0.023	0
diff. lin.	10	2.8	0	0.023	0
diff. lin. / nonlin.	10	2.8	0	0.023	0
diff. lin. / VPM	10	2.8	0	0.023	0
diff. nonlin.	10	6.0	ref.	0.160	ref.
diff. nonlin. / VPM	10	6.3	5.0	0.160	0
diff. VPM	10	7.0	-	0.180	-
diff. nonlin.	25	71.5	ref.	2.920	ref.
diff. nonlin. / VPM	25	74.5	4.19	2.957	1.26
diff. VPM	25	79.3	-	3.758	-
diff. nonlin.	50	274.1	ref.	10.323	ref.
diff. nonlin. / VPM	50	281.5	2.70	10.423	0.96
diff. VPM	50	292.8	-	15.049	-
complex	75	156.9	ref.	1.309	ref.
linear	75	157.1	0.13	1.307	0.15
diff. lin.	75	157.1	0.13	1.307	0.15
diff. lin. / nonlin.	75	157.1	0.13	1.307	0.15
diff. lin. / VPM	75	163.3	4.07	1.308	0.07
diff. nonlin.	75	524.2	ref.	17.482	ref.
diff. nonlin. / VPM	75	528.2	0.57	17.562	0.45
diff. VPM	75	543.5	-	26.737	-

Table 14: Verification steps for the ECP with a rectangular current loop. Abbreviations according to Fig. 1.1.

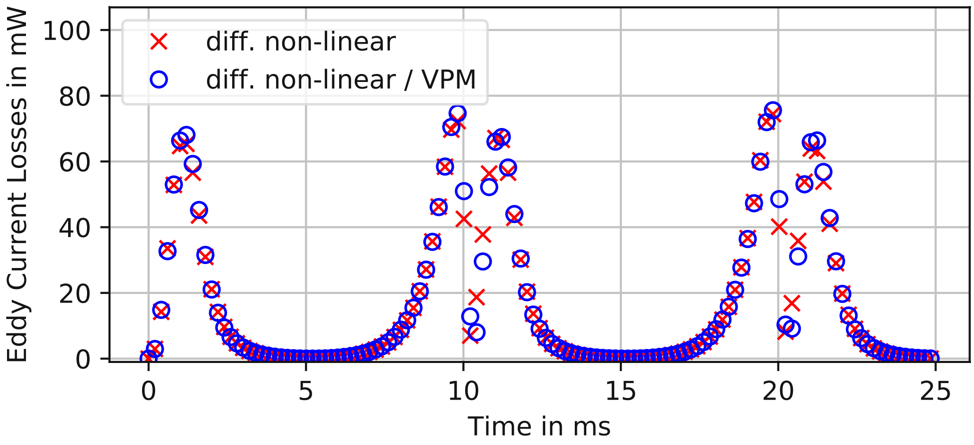

Figure 8.3: Eddy current losses for $I_0 = 75\text{A}$ for the nonlinear material without hysteresis. The nonlinear material is defined by the initial magnetisation curve of the ferromagnetic material.

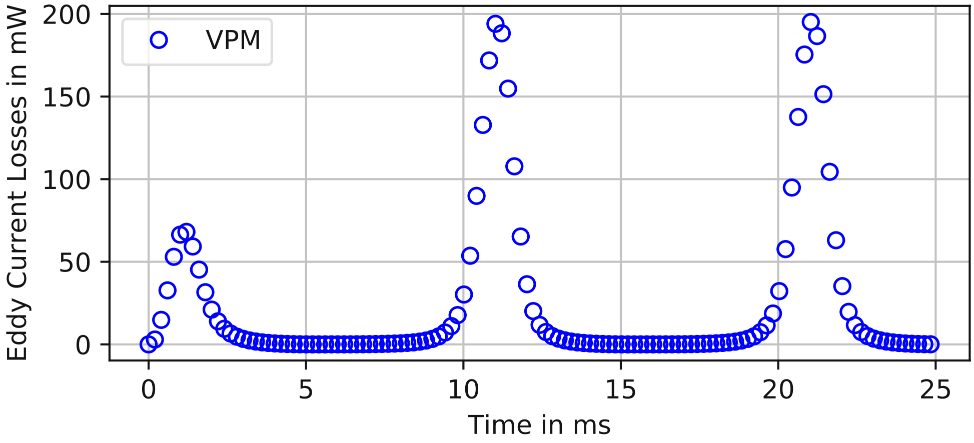

Figure 8.4: Eddy current losses for $I_0 = 75\text{A}$ for the nonlinear material with vector hysteresis. The ferromagnetic material is set by a Lorentzian EF with parameters of 50Hz, see Table 2.

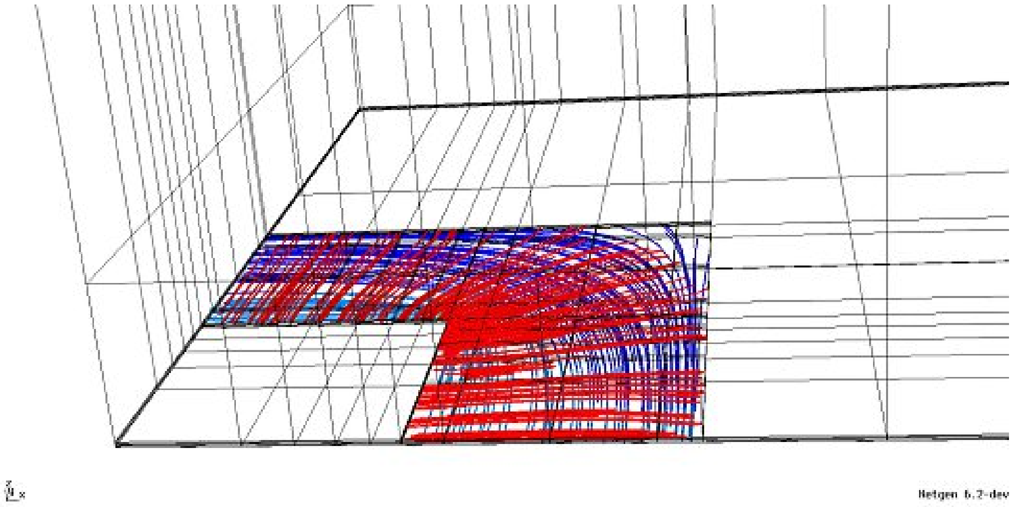

Figure 8.5: Magnetic flux density (blue) and the eddy current density (red) in an iron sheet.

9 Mixed Multiscale Method

In this section, an efficient and accurate technique to solve the eddy current problem (ECP) in laminated iron cores by a mixed multiscale finite element method (MMSFEM) based on the $\boldsymbol{T}$, Φ-Φ formulation using the vector Preisach model (VPM) is introduced and studied by the numerical example in Section 8. Moreover, the electromagnetic excitation of the problem is given by coils. Additionally to the verification scheme in Fig. 1.1, a verification against the standard finite element method (SFEM) has been carried out.

The MMSFEM is used to avoid the necessity to resolve the individual sheets in a laminated core. Using MMSFEM, the laminated core is considered as bulk material. The MMSFEM approach

$$\tilde{\mathbf{H}} = \begin{cases} \boldsymbol{T}_{BS} + \boldsymbol{T}_2\phi_2 - \nabla\Phi_0 & \text{in } \Omega_c \\ \boldsymbol{T}_{BS} - \nabla\Phi_0 & \text{in } \Omega_0 \end{cases} \tag{9.1}$$

with the micro-shape function ϕ_2, shown in Fig. 9.1, is selected. The approach is based on the fact that the problem can be observed on the large scale with the overall dimensions of the laminated core, on the one hand, and, on the other, on the small scale with the very small thickness of the sheets and the insulation layer. The magnetic scalar potential (MSP) Φ_0 takes into account the solution on the large scale while the current vector potential (CVP) $\boldsymbol{T}_2$ along with the periodic micro-shape function ϕ_2 considers the oscillating variation on the small scale due to the sheets [4]. The second order Gauss-Lobatto polynomial

$$\begin{aligned} \phi_2 : & z \in [-d/2, d/2] \to \mathbb{R} \\ & z \mapsto \begin{cases} \sqrt{\frac{3}{8}}\left(\frac{4}{d_{Fe}^2} z^2 - 1\right) & \text{for } z \in [-d_{Fe}/2, d_{Fe}/2] \\ 0 \text{ otherwise} \end{cases} \end{aligned} \tag{9.2}$$

is chosen as micro-shape function ϕ_2 [3]. The thickness $d = d_{Fe} + d_0$ is the sum of the width of the sheet and the width of the gap, respectively.

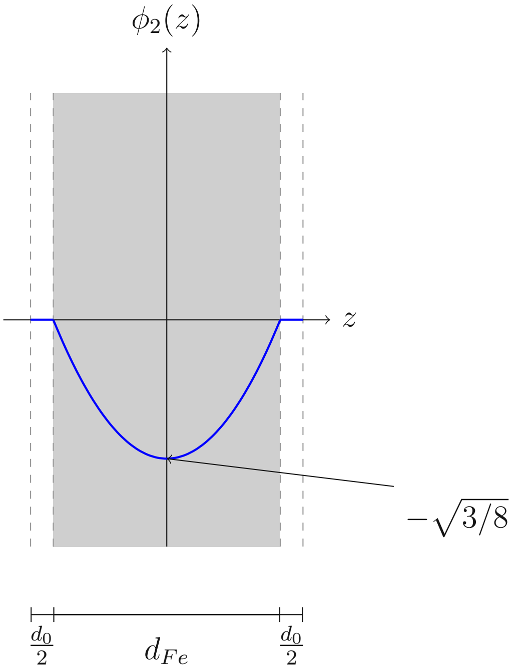

Figure 9.1: Second order Gauss-Lobatto polynomial as micro-shape function ϕ_2 in a sheet (grey) with an air gap of width d_0.

9.1 Material Parameters

The MMSFEM observes the laminated core as bulk material. To obtain the specific material parameters in a global integration point (GIP), an additional local integration of, for example, the differential permeability $\overline{\overline{\mu}}^{\Delta}$ in the local integration points (LIPs) is needed, as shown in Fig. 9.2. In each LIP an independent VPM is set up and is updated in every time instant.

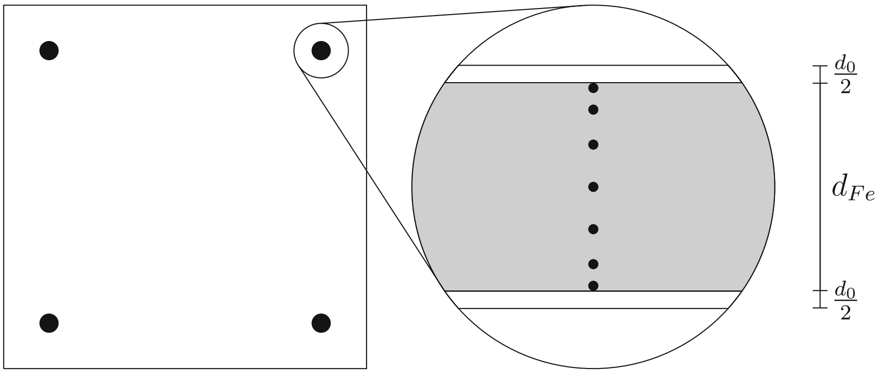

Figure 9.2: Global (left) and local integration points (right) in the bulk iron core Ω_c.

As an example for the different homogenised material parameters the homogenised parameter

$$\overline{\mu\phi_2} = \frac{1}{d}\int_{-\frac{d}{2}}^{\frac{d}{2}} \mu(z)\phi_2(z)\; dz \tag{9.3}$$

is calculated with the scalar nonlinear parameter $\mu(z)$ with the micro-shape function $\phi_2(z)$. All multiscale coefficients are marked by the bar and are calculated accordingly. In particular, the calculation of the tensor-valued differential permeability $\overline{\overline{\mu}}^{\Delta}$ the integration is done for each matrix element separately.

For the verification, according to Fig. 1.1, linear material relations are necessary. With (9.3), the coefficients for a generic linear material coefficient λ are

$$\overline{\lambda} = \frac{\lambda d_{Fe} + \mu_0 d_0}{d}, \tag{9.4a}$$

$$\overline{\lambda\phi_2} = -\lambda\frac{d_{Fe}}{\sqrt{6}\; d}, \tag{9.4b}$$

$$\overline{\lambda\phi_2\phi_2} = \lambda\frac{d_{Fe}}{5\; d}, \tag{9.4c}$$

$$\overline{\lambda\partial_z\phi_2\partial_z\phi_2} = \lambda\frac{2}{d_{Fe}\; d}. \tag{9.4d}$$

The coefficient λ stands either for the linear magnetic permeability μ or the electric resistivity ρ.

9.2 Boundary Value Problem

Analogously to the boundary value problem (BVP) in Section 8, the BVP for the ECP with the MMSFEM is derived. The MMSFEM uses the approach (9.1).
The BVP with the mixed $\boldsymbol{T}, \Phi$-Φ formulation for the quasi-static magnetic field in the conducting

domain Ω_c is described by

$$\left.\begin{aligned} \nabla \times (\rho \nabla \times \phi_2 \boldsymbol{T}) + \partial_t \mu \phi_2 \boldsymbol{T} - \partial_t \mu \nabla \Phi_0 &= -\nabla \times (\rho \nabla \times \boldsymbol{T}_{BS}) - \partial_t \mu \boldsymbol{T}_{BS}, \\ -\nabla \cdot \mu \nabla \Phi_0 + \nabla \cdot \mu \phi_2 \boldsymbol{T} &= -\nabla \cdot \mu \boldsymbol{T}_{BS} \end{aligned}\right\} \quad \text{in } \Omega_c \tag{9.5a}$$

$$\left.\begin{aligned} \phi_2 \boldsymbol{T} \times \mathbf{n} &= \mathbf{0}, \\ \Phi_0 &= 0 \end{aligned}\right\} \quad \text{on } \Gamma_{H_c} \tag{9.5b}$$

$$\left.\begin{aligned} (\rho \nabla \times \phi_2 \boldsymbol{T}) \times \mathbf{n} &= -(\rho \nabla \times \boldsymbol{T}_{BS}) \times \mathbf{n}, \\ \mu(\phi_2 \boldsymbol{T} - \nabla \Phi_0) \cdot \mathbf{n} &= -\mu \boldsymbol{T}_{BS} \cdot \mathbf{n} \end{aligned}\right\} \quad \text{on } \Gamma_E. \tag{9.5c}$$

The static magnetic field in the non-conducting domain Ω_0 is described by

$$-\nabla \cdot (\mu_0 \nabla \Phi_0) = -\nabla \cdot (\mu_0 \boldsymbol{T}_{BS}) \quad \text{in } \Omega_0 \tag{9.6a}$$

$$-\mu \nabla \Phi_0 \cdot \mathbf{n} = -\mu \boldsymbol{T}_{BS} \cdot \mathbf{n} \quad \text{on } \Gamma_B \tag{9.6b}$$

$$\Phi_0 = 0 \quad \text{on } \Gamma_{H_0}. \tag{9.6c}$$

Finally, the interface conditions on Γ_{0c} are

$$\left.\begin{aligned} \mu(\phi_2 \boldsymbol{T} - \nabla \Phi_0) \cdot \mathbf{n}_c - \mu_0 \nabla \Phi_0 \cdot \mathbf{n}_0 &= -\mu \boldsymbol{T}_{BS} \cdot \mathbf{n}_c - \mu_0 \boldsymbol{T}_{BS} \cdot \mathbf{n}_0 \\ \phi_2 \boldsymbol{T} \times \mathbf{n}_c &= \mathbf{0} \end{aligned}\right\} \quad \text{on } \Gamma_{0c}. \tag{9.7}$$

9.3 Weak Formulation

The weak formulation is obtained by multiplying (9.5a) and (9.6a) with the test functions and by integrating over the associated domains. The scalar test function is denoted by Φ_0' and the vectorial test function is $\boldsymbol{T}_2'$.
Additionally, the differential approach to overcome the singularity of the tensor-valued permeability $\overline{\overline{\mu}}$ in the magnetic remanence, see Section 8.3, and the fixed-point method to solve the nonlinear problem, see Section 8.4, are carried out.

Find $(\boldsymbol{T}_2^{(n+1)}, \Phi_0^{(n+1)}) \in V_D := \{(\boldsymbol{T}_2^{(n+1)}, \Phi_0^{(n+1)}) : \boldsymbol{T}_2^{(n+1)} \in \mathcal{U}, \Phi_0^{(n+1)} \in \mathcal{V}, \boldsymbol{T}_2^{(n+1)} \times \boldsymbol{n} = \mathbf{0}$ on $\Gamma_{0c} \setminus \Gamma_{T_2} \cup \Gamma_{H_c}$, $\Phi_0^{(n+1)} = 0$ on $\Gamma_{H_c} \cup \Gamma_{H_0}\}$, such that

$$\left.\begin{aligned} &\Delta t \int_{\Omega_c} \overline{\rho \phi_2 \phi_2}\, \nabla \times \boldsymbol{T}_2^{(n+1)} \cdot \nabla \times \boldsymbol{T}_2'\, d\Omega \\ &+ \Delta t \int_{\Omega_c} \overline{\rho \partial_z \phi_2 \partial_z \phi_2}\, (\boldsymbol{T}_{2,x}^{(n+1)} \boldsymbol{T}_{2,x}' + \boldsymbol{T}_{2,y}^{(n+1)} \boldsymbol{T}_{2,y}')\, d\Omega \\ &+ \int_{\Omega_c} \overline{\mu_{FP}^{\Delta} \phi_2 \phi_2}\, \boldsymbol{T}_2^{\Delta} \cdot \boldsymbol{T}_2'\, d\Omega - \int_{\Omega_c} \overline{\mu_{FP}^{\Delta} \phi_2}\, \nabla \Phi_0^{\Delta} \cdot \boldsymbol{T}_2'\, d\Omega \\ &\quad = \int_{\Omega_c} \overline{(\overline{\overline{\mu}}_{FP}^{\Delta} - \overline{\overline{\mu}}^{\Delta}) \phi_2 \phi_2}\, \boldsymbol{T}_2^{\Delta,(n)} \cdot \boldsymbol{T}_2'\, d\Omega \\ &\qquad - \int_{\Omega_c} \overline{(\overline{\overline{\mu}}_{FP}^{\Delta} - \overline{\overline{\mu}}^{\Delta}) \phi_2}\, \nabla \Phi_0^{\Delta,(n)} \cdot \boldsymbol{T}_2'\, d\Omega \\ &\qquad - \int_{\Omega_c} \overline{\overline{\overline{\mu}}^{\Delta} \phi_2}\, \boldsymbol{T}_{BS}^{\Delta} \cdot \boldsymbol{T}_2'\, d\Omega \end{aligned}\right. \quad \text{in } \Omega_c \tag{9.8}$$

and

$$\int_{\Omega_0} \mu_0\, \nabla \Phi_0^{\Delta} \cdot \nabla \Phi_0'\, d\Omega = \int_{\Omega_0} \mu_0 \boldsymbol{T}_{BS}^{\Delta} \cdot \nabla \Phi_0'\, d\Omega \quad \text{in } \Omega_0 \tag{9.9a}$$

$$\begin{aligned}&\int_{\Omega_c} \overline{\mu_{FP}^{\Delta}}\, \nabla\Phi_0^{\Delta} \cdot \nabla\Phi_0'\, d\Omega - \int_{\Omega_c} \overline{\mu_{FP}^{\Delta}\phi_2}\, \boldsymbol{T}_2^{\Delta} \cdot \nabla\Phi_0'\, d\Omega \\ &= \int_{\Omega_c} \overline{(\overline{\overline{\mu}}_{FP}^{\Delta} - \overline{\overline{\mu}}^{\Delta})}\, \nabla\Phi_0^{\Delta,(n)} \cdot \nabla\Phi_0'\, d\Omega - \int_{\Omega_c} \overline{(\overline{\overline{\mu}}_{FP}^{\Delta} - \overline{\overline{\mu}}^{\Delta})\phi_2}\, \boldsymbol{T}_2^{\Delta,(n)} \cdot \nabla\Phi_0'\, d\Omega \qquad \text{in } \Omega_c \qquad (9.9b) \\ &\quad + \int_{\Omega_c} \overline{\overline{\overline{\mu}}^{\Delta}}\, \boldsymbol{T}_{BS}^{\Delta} \cdot \nabla\Phi_0'\, d\Omega\end{aligned}$$

for all $(\boldsymbol{T}_2', \Phi_0') \in V_0$, where $\mathcal{U} \subset H(\mathrm{curl}, \Omega_c)$, $\mathcal{V} \subset H^1(\Omega)$ and $\phi_2 \in H^1_{per}(\Omega_c)$ have been selected [21]. The interface Γ_{T_2} is the part of Γ_{0c}, which represents the smooth surface of the laminated iron core, see Fig. 9.3. The multiscale coefficients are denoted by the overlining bar and are calculated according to (9.3). The differential potentials $\boldsymbol{T}_2^{\Delta} = \boldsymbol{T}_2^{(n+1)} - \boldsymbol{T}_2^{(n)}$ and $\Phi_0^{\Delta} = \Phi_0^{(n+1)} - \Phi_0^{(n)}$ are differential potentials from the $(n+1)$-th time instant. For the sake of readability, it has been omitted to move the known terms of the differential potentials to the right hand side in (9.8) and (9.9). The differential potentials of the (n)-th time instant are denoted by $\boldsymbol{T}_2^{\Delta,(n)} = \boldsymbol{T}_2^{(n)} - \boldsymbol{T}_2^{(n-1)}$ and $\Phi_0^{\Delta,(n)} = \Phi_0^{(n)} - \Phi_0^{(n-1)}$.

9.4 Numerical Example

The ECP of the laminated iron core shown in Figs. 9.3 and 9.4 is investigated. The thickness of an iron sheet is $d_{Fe} = 0.5$mm and the width of the gap is $d_0 = 0.01$mm, yielding a fill-factor $k_f = \frac{d_{Fe}}{d_{Fe}+d_0} = 0.9804$. The core is composed of 184 sheets. The electric conductivity of iron is selected with $\sigma = \rho^{-1} = 2 \cdot 10^6$S/m. The excitation of the problem is considered by the Biot-Savart field of four symmetric cylindrical coils with 60 turns each. The frequency is selected with $f = 50$Hz. The arrangement of the core with the coils exhibits three planes of symmetry. Hexahedral finite elements (FEs) are used for the mesh. One period of time is discretised in 600 steps. The material of the iron sheets is considered to be demagnetised initially. For the SFEM each iron sheet and each air gap are resolved. For the MMSFEM the mesh is generated according to the rule described in [4, p. 3]. Thereby, the penetration depth is considered by generating a finer mesh at the top of the stack. The simulations have been carried out by Netgen/NGSolve [2].

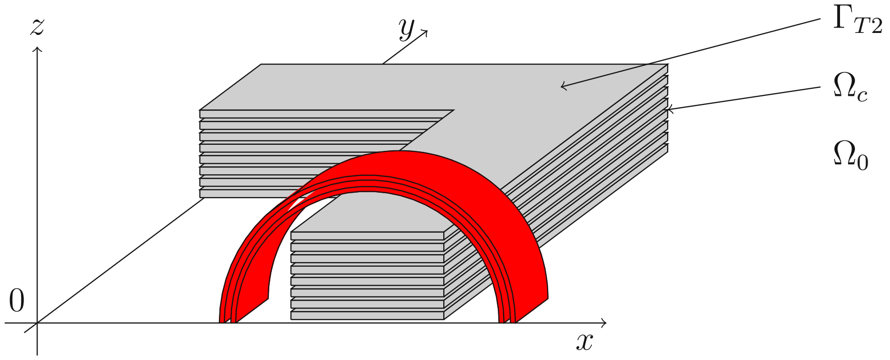

Figure 9.3: One eighth of the laminated iron core (gray) with the coils (red), not drawn to scale.

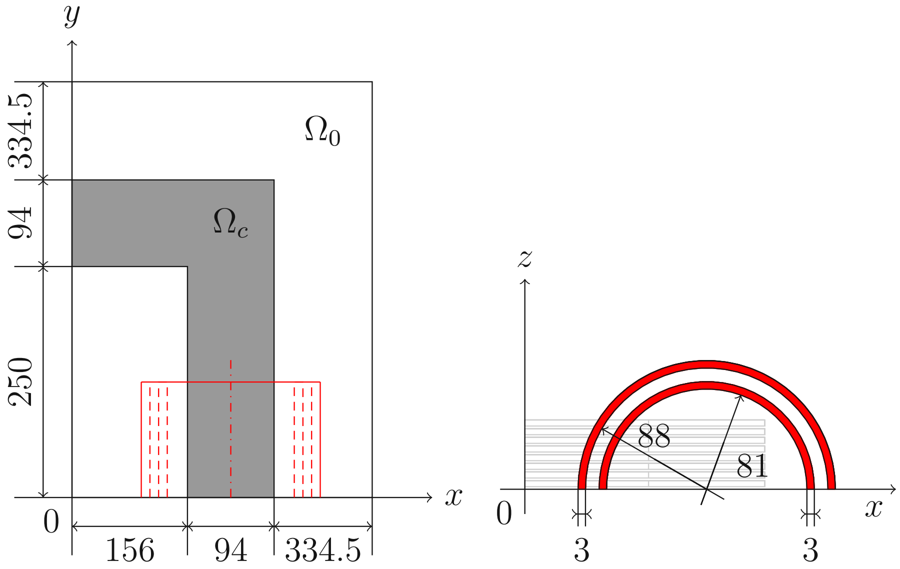

Figure 9.4: Top (left) and front (right) view of the geometry, not drawn to scale, dimensions are in mm, planes of symmetry are $x = 0$, $y = 0$ and $z = 0$. Thus only one eight of the problem has been simulated. The total length of the coil is 192mm.

The reference solution with SFEM has been computed to verify the results obtained by the MMSFEM. Simulations with different peak values of the impressed currents I_0 and a different number of iron sheets have been carried out. For every time instant the eddy current losses

$$p(t) = \int_{\Omega_c} \rho \mathbf{J}(t) \cdot \mathbf{J}(t) \, d\Omega \tag{9.10}$$

have been calculated. The eddy current losses for simulations with $I_0 = 1\text{A}$ and $I_0 = 3\text{A}$ and 184 sheets obtained by the SFEM and the MMSFEM are shown in Fig. 9.5 and Fig. 9.6, respectively. For the sake of visibility, only every fifth time instant is shown.

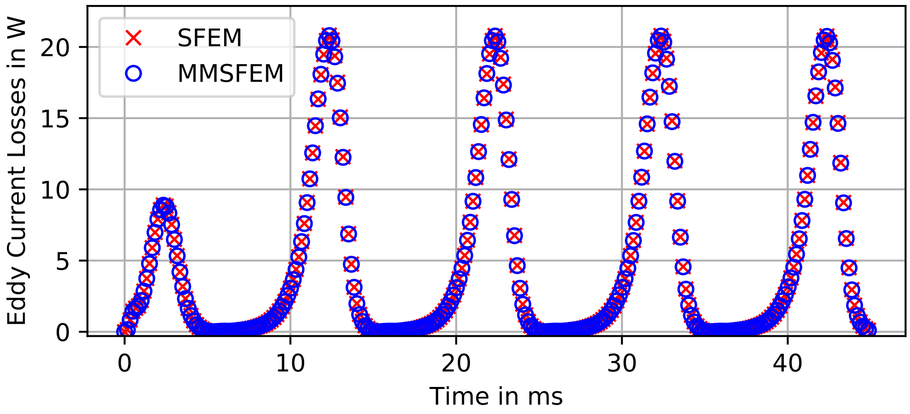

Figure 9.5: Eddy current losses for $I_0 = 1\text{A}$ peak.

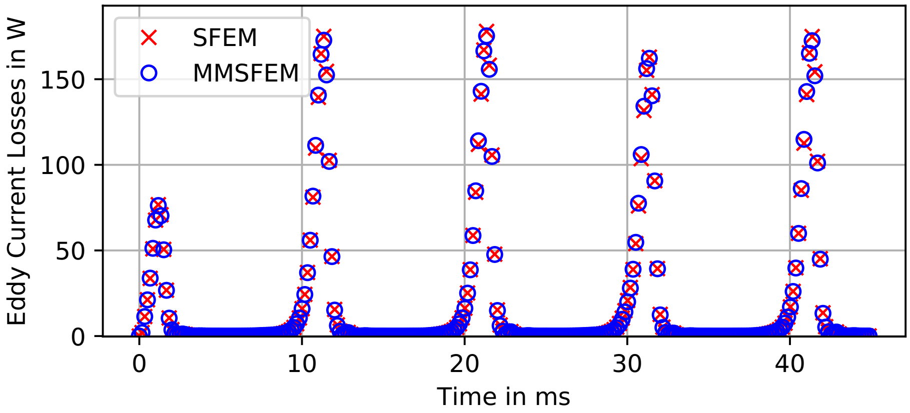

Figure 9.6: Eddy current losses for $I_0 = 3\text{A}$ peak.

Further, the mean value of the losses

$$P = \frac{1}{T}\int_{t'}^{t'+T} p(t)\ dt \tag{9.11}$$

has been calculated in the steady state. With the aid of P the error

$$\varepsilon_1 = 100\frac{|P_{SFEM} - P_{MMSFEM}|}{|P_{SFEM}|} \tag{9.12}$$

has been calculated, which is not very sensitive. For a stricter criterion the error

$$\varepsilon_2 = \frac{100}{T}\int_{t'}^{t'+T} \frac{|p_{SFEM} - p_{MMSFEM}|}{|p_{SFEM}|}\ dt \tag{9.13}$$

using the time instants of the eddy current losses $p(t)$, has been introduced.
A comparison of the local solution of the SFEM and the MMSFEM is shown in Fig. 9.7 and Fig. 9.8 representing the magnetic flux density **B** and the current density **J** in the same layer. Moreover, the simulation results with different impressed currents and a different number of sheets are summarised in Table 15.
The reduction of degrees of freedom N_{DOF} increases with the number of sheets in the laminated iron core for both MMSFEM and SFEM. However, MMSFEM requires essentially less N_{DOF}. The same holds for the number of VPMs N_{VPM}, as well as for the required computation time. The number of needed VPMs for small problems with just a few sheets is relatively high, which results in long simulation times t_{sim} also for MMSFEM. Therefore, the advantage of the MMSFEM becomes clearly visible for a large number of sheets.
In the given example with 184 sheets and an excitation with $I_0 = 3\text{A}$, the SFEM needs 130h whereas the MMSFEM only needs 23h on the same computer.

For the sake of completeness, the simulation results for the verification according to Fig. 1.1 with the relative errors (8.39) based on the eddy current losses and the magnetic energy densities are summarised in Table 16.

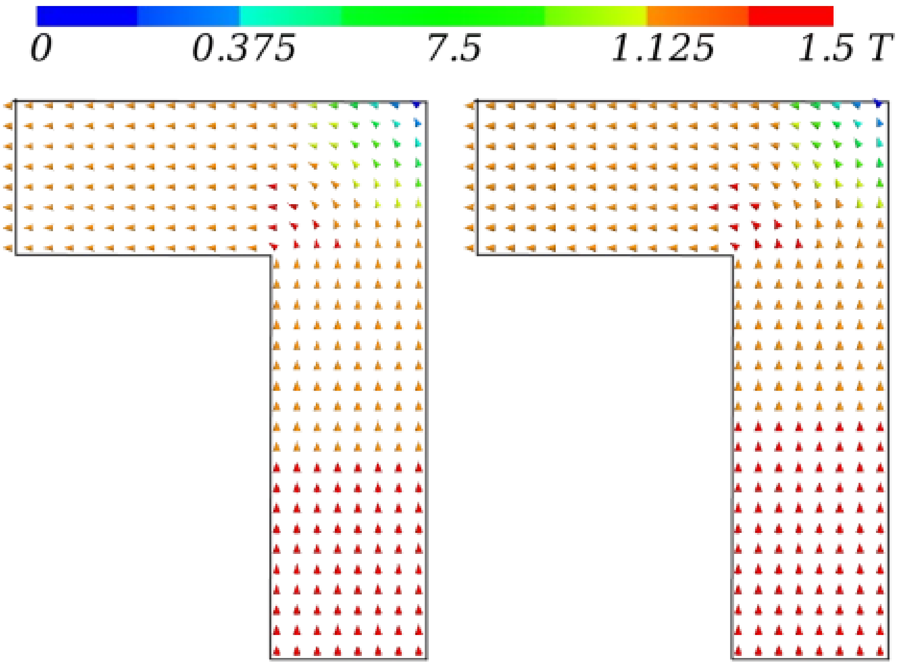

Figure 9.7: Magnetic flux density **B** for $I_0 = 3\text{A}$ peak-to-peak at $z \approx 49.9\text{mm}$ and $t = 25\text{ms}$, reference solution with SFEM on the left and MMSFEM on the right.

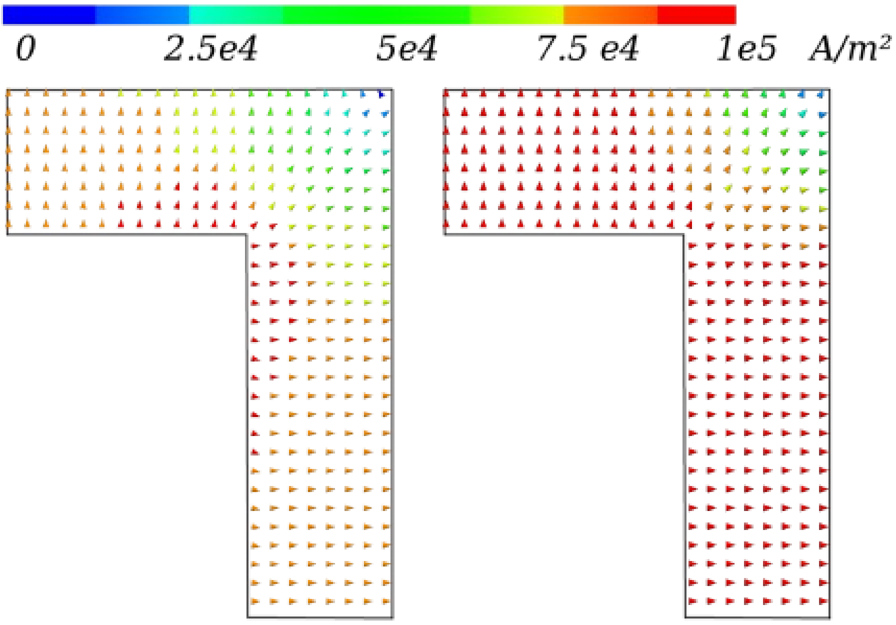

Figure 9.8: Current Density **J** for $I_0 = 3\text{A}$ peak-to-peak at $z \approx 49.9\text{mm}$ and $t = 50\text{ms}$, reference solution with SFEM on the left and MMSFEM on the right.

No. Sheets		4	20	184	184
I_0 in A		3	3	1	3
P in W	SFEM	0.405	2.09	5.011	19.307
	MMSFEM	0.402	2.088	5.006	19.294
ε_1 in %		0.724	0.092	0.110	0.068
ε_2 in %		6.131	12.069	0.727	11.812
N_{DOF}	SFEM	58,868	195,940	1,600,928	1,600,928
	MMSFEM	50,013	74,175	122,499	122,499
N_{VPM}	SFEM	14,336	71,680	659,456	659,456
	MMSFEM	100,352	200,704	401,408	401,408
t_{sim} in h	SFEM	6.1	17.9	125.8	130.7
	MMSFEM	9.7	14.6	21.3	22.7

Table 15: Numerical data for various simulations with up to 184 sheets.

Verification Step	SFEM	MMSFEM	I_{max} in A	W_H in μW	ε_H in %	W_E in mW	ε_E in %
linear	●		3	2287.6	ref.	24.049	ref.
		●	3	2273.6	0.61	23.530	2.16
diff. linear	●		3	2287.3	0.01	24.049	0.00
		●	3	2273.6	0.61	23.530	2.16
diff. lin. / non- lin.	●		3	2287.3	0.01	24.049	0.00
		●	3	2312.0	1.07	23.528	2.17
diff. lin. / VPM	●		3	2321.8	1.50	24.049	0.00
		●	3	2318.2	1.34	23.539	2.12
nonlin.	●		3	6566.0	ref.	311.193	ref.
		●	3	6585.8	-0.30	305.756	1.75
diff. nonlin. / VPM	●		3	6314.4	3.83	335.293	7.74
		●	3	6488.7	1.18	321.940	3.45
VPM	●		3	6297.7	ref	419.348	ref.
		●	3	6520.7	3.40	406.741	3.45

Table 16: Verification steps for the ECP excited by coils with 4 sheets for SFEM and MMSFEM. Abbreviations according to Fig. 1.1.

10 Conclusions

This thesis deals with the problem to efficiently compute the eddy currents in ferromagnetic sheets by the method of finite elements. The used hysteresis model is the vector Preisach model (VPM), which is based on a superposition of scalar Preisach models (SPMs), to deal with the ferromagnetism. The multiscale finite element method (MSFEM) is used to avoid the requirement of modelling each individual sheet in the finite element (FE) mesh.

The implemented SPM is flexible, accurate and high performant. Due to special modifications of the Everett function (EF), a verification against linear and nonlinear model is feasible. Carrying out investigations on different distributions of SPMs on the surface of a unit sphere and different discretisation methods for the Preisach plane, an accurate and fast VPM has been developed. The presented SPM and the VPM are implemented in C++ and integrated into Netgen/NGSolve [2] to facilitate convenient simulations of electromagnetic field problems.

Different simulations of electromagnetic field problems have been carried out. First, a fixed-point method to solve nonlinear equations is exploit. Second, a numerical example for the inverse mode of the scalar Preisach model (iSPM) with the $\mathbf{A}$ formulation is given. Third, a magneto-static example with different formulations is presented. In the fourth step, the eddy current problem (ECP) is solved using the $\boldsymbol{T}, \Phi$-Φ formulation. In the last step, the mixed multiscale finite element method (MMSFEM) is successfully introduced, with which it is no longer necessary to resolve individual sheets in the FE model. Using MMSFEM, the computational effort could be reduced enormously compared to the standard finite element method (SFEM) while maintaining the accuracy.

All simulations are verified according to the scheme in Fig. 1.1. The simulations using MMSFEM are additionally verified against the solution obtained by the SFEM.

The implemented Preisach models work properly and the simulation approach with the MMSFEM is valid.

Future work could deal with various problems summarised in the following:

- To gain smaller computation times, the number of VPM or the number of SPM per VPM has to be reduced radically.
- Since the thesis does not discuss the inverse mode of the vector Preisach model (iVPM), this has to be done in a future work. One approach is to find a fitting input, analogously to the scalar approach. Another approach is shown for instance in [22] which modifies the EF.
- The calculation of hysteresis losses by means of the SPM is well discussed in [1]. However, the determination of the losses vector hysteresis is still a challenging task.
- In this thesis, the verification is always done against reference solutions obtained by SFEM. To evaluate the models for hysteresis measurement data shall be used.

References

[1] I. D. Mayergoyz, *Mathematical models of hysteresis*. Springer-Verlag, Dec. 1991.

[2] J. Schöberl. (). Netgen/ngsolve, [Online]. Available: `https://ngsolve.org/`.

[3] K. Hollaus, “A MSFEM to simulate the eddy current problem in laminated iron cores in 3D”, *COMPEL - The international journal for computation and mathematics in electrical and electronic engineering*, pp. 1667–1682, 2019.

[4] K. Hollaus and M. Schöbinger, “A Mixed Multiscale FEM for the Eddy Current Problem with $\boldsymbol{T}$, Φ-Φ in Laminated Conducting Media”, *IEEE Transactions on Magnetics*, pp. 1–1, 2020.

[5] D. techn. Karl Hollaus, *Numerical Simulation of Eddy Currents and the Associated Losses in Laminated Ferromagnetic Materials by the Method of Finite Elements. PhD Thesis*. TU Graz, 2001.

[6] M. Tousignant, F. Sirois, S. Dufour and G. Meunier, “Efficient numerical implementation of a vector preisach hysteresis model for 3-d finite element applications”, 2017.

[7] M. Schöbinger, S. Steentjes, J. Schöberl, K. Hameyer and K. Hollaus, “Msfem for the eddy current problem in a laminated core including hysteresis”, *IEEE Transactions on Magnetics*, vol. 55, no. 8, pp. 1–9, 2019.

[8] G. M. Fasching, *Werkstoffe für die Elektrotechnik: Mikrophysik, Struktur, Eigenschaften (German Edition), 4. Auflage*. Springer, Jan. 2005.

[9] A. Katanforoush and M. Shahshahani, “Distributing points on the sphere”, *Exp. Math.*, vol. 12, Apr. 2012.

[10] C. H. L. Beentjes, “Quadrature on a spherical surface”, University of Oxford, Technical report, 2016.

[11] S. Ringkowski, “Ausarbeitung zum Vortrag im Proseminar Analysis”, Ruprecht-Karls-Universität Heidelberg, Seminar work, 2009.

[12] V. Lebedev, “Quadratures on a sphere”, *USSR Computational Mathematics and Mathematical Physics*, vol. 16, no. 2, pp. 10–24, 1976.

[13] J. Gyselinck, L. Vandevelde, D. Makaveev and J. A. A. Melkebeek, “Calculation of no load losses in an induction motor using an inverse vector preisach model and an eddy current loss model”, *IEEE Transactions on Magnetics*, vol. 36, no. 4, pp. 856–860, Jul. 2000.

[14] A. Prechtl, *Vorlesungen über die Grundlagen der Elektrotechnik II*, 2. Aufl. Berlin Heidelberg New York: Springer-Verlag, 2009.

[15] M. Kuczmann and A. Ivanyi, *The Finite Element Method in Magnetics*. Jan. 2008.

[16] O. Bottauscio, D. Chiarabaglio, M. Chiampi and M. Repetto, “A hysteretic periodic magnetic field solution using preisach model and fixed point technique”, *IEEE Transactions on Magnetics*, vol. 31, no. 6, pp. 3548–3550, Nov. 1995.

[17] D. techn. Karl Hollaus, *Einführung in partielle Differentialgleichungen und Methode der finiten Elemente*. TU Wien, 2016.

[18] H. J. Silm, *Benchmark for the eddy current problem in laminated iron cores*, eng. Wien, 2016.

[19] K. Hollaus, “Eddy Current Problem: $\boldsymbol{T}$, Φ-Φ - Formulation, PhD course on Numerical Analysis of Electromechanical Devices: Theory and Application”, Helsinki, talk, 2017.

[20] O. Bíró, “Edge element formulations of eddy current problems”, *Computer Methods in Applied Mechanics and Engineering*, vol. 169, no. 3, pp. 391–405, 1999.

[21] J. Schoeberl and S. Zaglmayr, “High order Nédélec elements with local complete sequence properties”, *COMPEL-the International Journal for Computation and Mathematics in Electrical and Electronic Engineering*, vol. 24, pp. 374–384, Jun. 2005.

[22] Y. Bernard, E. Mendes, L. Santandrea and F. Bouillault, “Inverse Preisach model in finite elements modelling”, *European Physical Journal-applied Physics - EUR PHYS J-APPL PHYS*, vol. 12, pp. 117–121, Nov. 2000.

Mathematical Symbols and Nomenclature

This table holds all symbols used in mathematical expressions.

Symbol	Description	Unit
$\mathbf{A}$	magnetic vector potential	Vs/m
Φ	magnetic scalar potential	A
ϕ	micro-shape function	
$\mathbf{T}$	current vector potential	A/m
$\mathbf{B}$	magnetic flux density	Vs/m^2
$\mathbf{H}$	magnetic field strength	A/m
μ	permeability $\mu = B/H$	$Vs/(Am)$
μ^Δ	approximation of the differential permeability $\mu^\partial = \partial B/\partial H$	$Vs/(Am)$
μ_0	permeability of vacuum, $\mu_0 := 4 \cdot 10^{-7}\pi$	$Vs/(Am)$
ν	magnetic reluctivity $\nu = 1/\mu = H/B$	$Am/(Vs)$
Ω	volume of a geometry	m^3
Γ	boundary or part of the boundary of a volume, $\Gamma = \partial\Omega$	m^2
S_i	face of a cube	
$\mathbf{e}_x, \mathbf{e}_y, \mathbf{e}_z$	unit vectors in the Cartesian coordinate system	
$\mathbf{e}_R, \mathbf{e}_\theta, \mathbf{e}_\varphi$	unit vectors in the spherical coordinate system	
T_{max}	Preisach Plane	
N_A	number of discretisation points in one axis of the Preisach Plane T_{max}.	

In general the nomenclature outlined in Fig. 10.1 for faces of cubes is used.

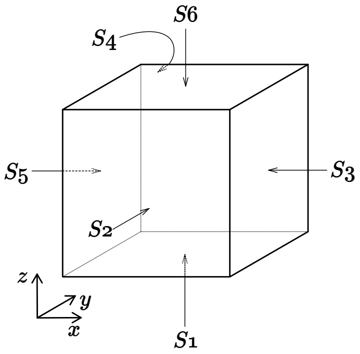

Figure 10.1: Numbering of the surfaces.

Glossary

BVP boundary value problem. 30, 45–47, 50–52, 54, 55, 58, 60, 62–64, 67, 69, 78, 79, 91, 95

CF NGSolve CoefficientFunction. 39, 40

CVP current vector potential. 67, 68, 77

ECP eddy current problem. 1, 67, 71, 73, 75, 77, 78, 80, 84, 85, 91, 92

EF Everett function. 1, 5–16, 20–22, 24–26, 28–32, 37, 40, 42, 56, 65, 74, 76, 85, 90–92, 100, 101

FE finite element. 70, 80, 85

FEM finite element method. 1, 43, 44, 59, 78

GIP global integration point. 78

iSPM inverse mode of the scalar Preisach model. 1, 23, 26–28, 54, 56, 85, 90, 92, 94

iVPM inverse mode of the vector Preisach model. 67, 85

LIP local integration point. 78

MMSFEM Mixed Multiscale Finite Element Method. 1, 77, 78, 80–82, 84, 85, 92

MSP magnetic scalar potential. 67, 77

SFEM standard finite element method. 77, 80–82, 84, 85, 92

SPM scalar Preisach model. 1–4, 6–8, 11–13, 16, 17, 20, 22–26, 28–32, 38, 39, 41, 42, 52, 53, 85, 90–92, 100, 101

VPM vector Preisach model. 1, 2, 31, 33, 37–42, 50–52, 64–67, 74, 75, 77, 78, 80, 82, 84, 85, 91, 94, 95

List of Figures

List of Tables

A Minimal Python Example for the Preisach Model

The following code illustrates the usage of the implemented Preisach models in a python code.

```python
from ngsolve import *
from ngsolve import *
import preisachCLib as pCV

# Everett Function and Sphere Distribution
NA = 401
maxH = 1640
maxB = 1.5
ev = pCV.Everett_ArcTanArcTan(NA, maxH, maxB)
dist = pCV.sphereLebedev(170, True)

# ---------------- without CF ------------------
P = pCV.preisachVector(ev, dist)
P.addH(maxH, 0, 0)
P.addH(0, 0, 0)
print("positive_remanence:\t%f" % P.getB().first)
# output : "positive_remanence:  0.869660"
P.addH(-maxH, 0, 0)
P.addH(0, 0, 0)
print("negative_remanence:\t%f" % P.getB().first)
# output : "negative_remanence:  -0.869660"

# ---------------- with CF ---------------------
from netgen.csg import *
# create a geometry
geo = CSGeometry()
geo.Add (OrthoBrick( Pnt(0,0,0), Pnt(1,1,1) ))
net_mesh = geo.GenerateMesh(maxh=2)
mesh = Mesh(net_mesh)
# create FESpace
fes = L2(mesh, dim=3)
intrule = IntegrationRule(TET,2)

# Gridfunction
H = GridFunction(fes, "H")
# Preisach CoefficientFunction
P = pCV.PreisachVectorCF(mesh, intrule, H, ev, dist, "H")
B = P.GetB()

# --- Apply input values ---
H.Set(CoefficientFunction((maxH, 0, 0)))
P.UpdatePast()
H.Set(CoefficientFunction((0, 0, 0)))
P.UpdatePast()
print("positive_remanence:\t%f" % Integrate(P.GetB(), mesh)[0])
# output: "positive_remanence:  0.869660"

H.Set(CoefficientFunction((-maxH, 0, 0)))
P.UpdatePast()
H.Set(CoefficientFunction((0, 0, 0)))
```

```
P.UpdatePast()
print("negative_remanence:\t%f" % Integrate(P.GetB(), mesh)[0])
# output : "negative_remanence:  -0.869660"
```

B Minimal C++ Example for the Preisach Model

The following code illustrates the usage of the forward and inverse mode of the scalar Preisach model (iSPM) and the usage of the forward vector Preisach model (VPM) in `C++`.

```
#include "preisachVector.h"

int main (/*int argc, char const* argv[]*/  ){

unsigned int NA = 501;
double maxH = 1640;
double maxB = 1.5;

shared_ptr<EverettMatrix>ev1D  =
make_shared<Everett_ArcTanArcTan>(NA, maxH, maxB);
shared_ptr<EverettMatrix>ev3D  =
make_shared<Everett_ArcTanArcTan>(NA, maxH, maxB);

shared_ptr<distributions> dist =
make_shared<sphereAdvPolarDistribution>(11);

preisach p1D(ev1D);
preisachVector p3D(ev3D, dist);

cout << "---- forward scalar Preisach model ----" << endl;
p1D.addH(maxH);
p1D.addH(0);
cout << "positive remanence:\t" << p1D.getB_interpolated() << endl;
// output: "positive remanence:  0.872972";

p1D.addH(-maxH);
p1D.addH(0);
cout << "negative remanence:\t" << p1D.getB_interpolated() << endl;
// output: "negative remanence:  -0.872972"


cout << "---- forward scalar Preisach model ----" << endl;
p1D.demagnetise();
p1D.addB(maxB);
p1D.addB(0);
cout << "positive coercivity:\t" << p1D.getH_interpolated() << endl;
// output: "positive coercivity:  -58.1846"
p1D.addB(-maxB);
p1D.addB(0);
cout << "negative coercivity:\t" << p1D.getH_interpolated() << endl;
// output: "negative coercivity:  58.1846"

cout << "---- forward vector Preisach model ----" << endl;
p3D.addH(maxH, 0, 0);
```

```
p3D.addH(0, 0, 0);
cout << "positive remanence:\t" << p3D.getB().first << endl;
//output: "positive remanence: 0.864891"

p3D.addH(-maxH, 0, 0);
p3D.addH(0, 0, 0);
cout << "negative remanence:\t" << p3D.getB().first << endl;
// output: "negative remanence:  -0.864891"

return 0;
}
```

C Example for the Differential Fixed-Point Method and the Vector Preisach Model

The following code yields an example for the usage of the implemented Preisach models in combination with Netgen/NGSolve [2], the fixed-point method and the differential method. In detail, the boundary value problem (BVP)

$$\nabla \cdot \left(\mu^{\Delta}(\phi^{\Delta})\nabla\phi^{\Delta}\right) = 0 \qquad \text{in } \Omega \tag{C.1}$$

$$\phi^{\Delta} = -H_0^{\Delta} x \qquad \text{on } S_1 \cup S_2 \cup S_3 \cup S_4 \cup S_5 \cup S_6 \tag{C.2}$$

is solved on a unit cube with only one domain Ω. The value H_0^{Δ} represents the boundary value difference in two steps.
The outcome is an image of the initial magnetisation curve followed by the major hysteresis loops and is displayed in Fig. C.1.

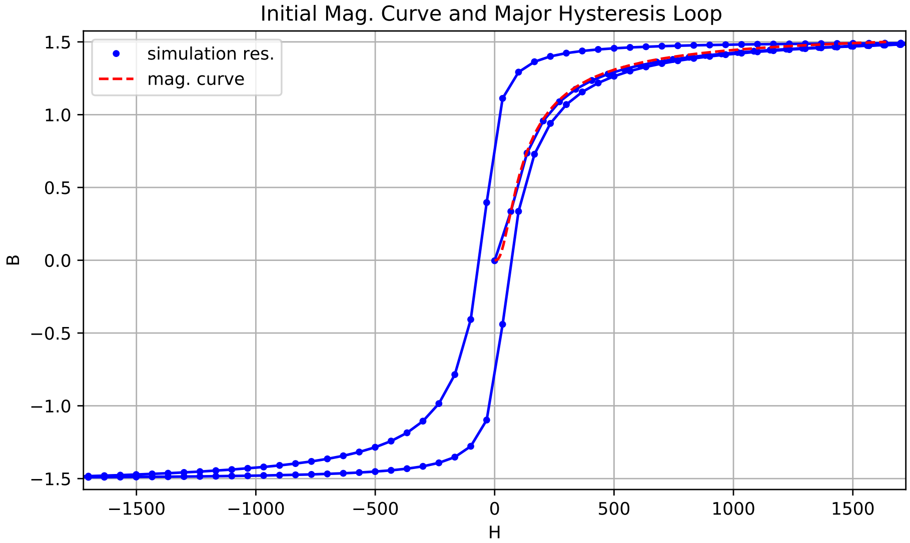

Figure C.1: Simulation outcome of the Netgen/NGSolve Example with a VPM.

```
# ---------------------------------------------------------------------
# -  Demonstration for the usage of the Preisach Library
# -
# -
# -  part of the Master thesis by Valentin Hanser
# -  valentin.hanser@student.tuwien.ac.at
```

```
# -
# -  Institute of Analysis and Scientific Computing, TU Wien
# -  March 2019
# -
# -
# -  Solves a laplace equation with a scalar magnetic potential and
# -  boundary conditions on a unit cube. The used approach for
# -  solving the nonlinear material relation is the fixed-point
# -  approach.
# -------------------------------------------------------------------

from ngsolve import *
import numpy as np
import preisachCLib as pCV

from netgen.csg import *

import matplotlib.pyplot as plt
import time

print("-----------------------ENTER MAIN----------------------------")
# -------------------------------------------------------------------
# -  Environment variables
# -------------------------------------------------------------------
SetNumThreads(10)
ngsglobals.msg_level = 0
# -------------------------------------------------------------------
# -  Input arguments
# -------------------------------------------------------------------
orderPhi = 1
mu0 = 4e-7*np.pi

# -------------------------------------------------------------------
# -  Geometry
# -------------------------------------------------------------------
geo = CSGeometry()
core = OrthoBrick( Pnt(0,0,0), Pnt(1,1,1) ).mat("iron").bc("outer")
geo.Add(core, maxh = 100)
mesh = geo.GenerateMesh(maxh=0.5)
mesh = Mesh(mesh)
intrule = IntegrationRule(TET,2*orderPhi)


# -------------------------------------------------------------------
# -  fes
# -------------------------------------------------------------------

fes = H1(mesh, order=orderPhi, dim=1, dirichlet="outer")

u = fes.TrialFunction()
v = fes.TestFunction()

sol = GridFunction(fes, "Phi")
```

```
sol_old = GridFunction(fes, "PhiOld")

dsol = GridFunction(fes, "dPhi")
dsol_old = GridFunction(fes, "dPhi_old")
dsol_it_old = GridFunction(fes, "dPhi_it_Old")


H = -grad(sol)
Draw(sol)

print("ndofs: ", fes.ndof)

# an exact integration point
mip_tD = pCV.GetExactMip(mesh, intrule, mesh(0.01, 0.01, 0.01))
mip = mesh(mip_tD.first, mip_tD.second, mip_tD.third)

# -------------------------------------------------------------------
# -  Preisach Model
# -------------------------------------------------------------------
NA = 401
maxH = 1640
maxB = 1.5

mask = CoefficientFunction([1])
ev = pCV.Everett_ArcTanArcTan(NA, maxH, maxB)
# ev.GenerateNonLinAdaption()
dist = pCV.sphereLebedev(170, True)
P = pCV.PreisachVectorCF(mesh, intrule, H, ev, dist, "H", mask)

dmu = P.GetMuDiff()
B = P.GetB()
# Is slightly different to the H (input) function
H_Preisach = P.GetH()

# initial magnetisation curve
KL = ev.GetInitialMagnetisationCurve().GetData()
KL = np.vstack(KL)
H_KL = KL[:, 0]
B_KL = KL[:, 1]


mu_diff_KL = (B_KL[1:]-B_KL[:-1])/((H_KL[1:]-H_KL[:-1]))
mu_diff_min = np.min(mu_diff_KL)
mu_diff_max = np.max(mu_diff_KL)
mu_FP = (mu_diff_max+mu_diff_min)/2


mu_FP = CoefficientFunction((mu_FP, 0, 0, 0, mu_FP, 0, 0, 0, mu_FP))
mu_FP.dims = (3,3)
dmu_var = mu_FP - dmu

# -------------------------------------------------------------------
# -  BFI
```

```
# ------------------------------------------------------------------


a = BilinearForm(fes, symmetric=False)
a += SymbolicBFI((mu_FP * grad(u))*grad(v))
c = Preconditioner(a, type = "direct")
a.Assemble()

f = LinearForm(fes)
f += SymbolicLFI((dmu_var * grad(dsol_old))*grad(v), \
definedon=mesh.Materials("iron"))

# ------------------------------------------------------------------
# -  Input
# ------------------------------------------------------------------
N = 30
val = np.linspace(0, maxH*1.2, N)
val = np.hstack([val, np.linspace(val[-1], -maxH*1.2, 2*N)])
val = np.hstack([val, np.linspace(val[-1], maxH*1.2, 2*N)])

bi = []
hi = []


time_sim = 0
with TaskManager():
 for i in range(len(val)):
  print("============================" + str(val[i]))
  sol_old.vec.data = sol.vec
  dsol_old.vec.data = dsol.vec
  time_sim_tmp = time.time()

  it = 0
  while True:

   it += 1
   # print ("Iteration",it)

   dsol_it_old.vec.data = dsol.vec
   if i == 0:
    dsol.Set(-val[i]*x, definedon=mesh.Boundaries("outer"))
   else:
    dsol.Set(-(val[i] - val[i-1])*x, \
    definedon=mesh.Boundaries("outer"))

   a.Assemble()

   bvp = BVP(bf = a, lf = f, gf = dsol, pre = c, maxsteps=50)
   bvp.Do()

   sol.vec.data = sol_old.vec + dsol.vec
   # pilot functions
   P.Update()
```

```
   # error estimation
   errL2=Integrate((dsol - dsol_it_old) * \
   (dsol - dsol_it_old),mesh)
   solL2=Integrate(dsol * dsol,mesh)

   # print("err:",errL2)
   # print("sol:",solL2)

   if solL2==0:
    break
   if errL2/solL2 < 1e-5:
   # print("Iterations:",it)
    break


   if it==5:
    print("warning: too many iterations", it)
    print("managed accuracy",errL2/solL2)
    break

  P.UpdatePast()
  # evaluate functions for plotting
  bi.append(B[0](mip))
  hi.append(H[0](mip))

  time_sim_tmp = time.time() - time_sim_tmp
  time_sim += time_sim_tmp

  if True and (i % 20 == 0 or i == len(val) - 1) :
   # plot
   plt.figure(1)
   plt.clf()
   plt.xlim([-1.05*maxH, 1.05*maxH])
   plt.ylim([-1.05*maxB, 1.05*maxB])
   plt.xlabel("H")
   plt.ylabel("B")
   plt.grid()
   plt.plot(hi, bi,'.b', label="simulation res.")
   plt.plot(hi, bi, '-b', label="simulation res.")
   plt.plot(H_KL, B_KL, '--r', label="mag. curve")
   plt.title("Initial Mag. Curve and Major Hysteresis Loop ")
   plt.legend()
   plt.show(False)
   plt.pause(0.1)

import netgen.gui
Redraw()

#save values
#dmu.Save("dmu.txt") # dmu.Load("B.txt")
#H.Save("H.txt") # H.Load("B.txt")
#B.Save("B.txt") # B.Load("B.txt")
```

```python
print("size of input data:\t %d" %(len(val)))
print("size of Everett Matrix:\t%d" % ev.size)
print("number of scalar Preisach models:\t %d" \
% (dist.size*P.CountVectorPreisachPoints()))
print("number of vectorial Preisach models:\t %d" \
% (P.CountVectorPreisachPoints()))
print("simulation time:\t %.3lf ms" % (time_sim * 1000))
print("t_pPpI:\t %.3lf us" %\
(time_sim/(dist.size*len(val)*P.CountVectorPreisachPoints()) * 1e6))

input()
```

D Example for the Calculation of an Everett Function based on an Initial Magnetisation Curve

This example presents a Python code for the calculation of an Everett function (EF) based on a given magnetisation curve. The magnetisation curve Table 12 of Section 7 is used. First, the magnetisation curve is used directly. Secondly, a cubic interpolation is used to increase the accuracy of the scalar Preisach model (SPM) by changing the discretisation of the Preisach Plane. Thirdly, the resulting initial magnetisation curve and the major loops are presented in Fig. D.1.

```python
import preisachCLib as pCV
import numpy as np
import matplotlib.pyplot as plt
# ----------------------------------------------------------------------
# - data of initial magnetisatin curve
# ----------------------------------------------------------------------
H_KL = [0,42,53,62,70,79,88,100,113,
                         132,157,193,255,376,677,1624,90168.5]
B_KL = [0,0.1,0.2,0.3,0.4,0.5,0.6,0.7,0.8,
                                 0.9,1,1.1,1.2,1.3,1.4,1.5,10]

KL_direct = np.transpose(np.vstack([H_KL, B_KL]))
ev_direct = pCV.Everett_NonLinear(KL_direct)
p_direct = pCV.preisach(ev_direct)
# ----------------------------------------------------------------------
# - interpolated approach
# ----------------------------------------------------------------------
NA = 401
KL_interpolated = pCV.KL(B_KL, H_KL, order=3)
B_KL_interpolated = np.linspace(0, 1.5, 501)
H_KL_interpolated = [KL_interpolated(B) for B in B_KL_interpolated]
KL_interpolated = np.transpose(np.vstack([H_KL_interpolated,


ev_interpolated = pCV.Everett_NonLinear(KL_interpolated)
p_interpolated = pCV.preisach(ev_interpolated)



# ----------------------------------------------------------------------
```

```
# - input signal
# -------------------------------------------------------------
ti = np.linspace(0, np.pi * 1.25, 5000)
hi = np.sin(ti)*1640

# -------------------------------------------------------------
# - calculate output signal
# -------------------------------------------------------------
bi_direct = [p_direct.addH(h) for h in hi]
bi_interpolated = [p_interpolated.addH(h) for h in hi]

# -------------------------------------------------------------
# - plot
# -------------------------------------------------------------
plt.figure(1)
plt.clf()
plt.plot(H_KL[:-1], B_KL[:-1],'og', label="KL roots")
plt.title("B/H plot for NL-EFs")
plt.plot(hi, bi_direct, '-b', label="direct")
plt.plot(hi, bi_interpolated, '--r', label="interpolated")

plt.xlabel("H")
plt.ylabel("B")
plt.legend()
plt.grid()
plt.show()
```

The result of the simulation is shown in Fig. D.1. The resulting initial magnetisation curve is a part of the major loop. This phenomenon is typical for nonlinear materials since no hysteresis phenomenon appears. The EF which uses the initial magnetisation curve results in a piece-wise linear output signal. The EF which interpolates the data first results in a smoother output signal.

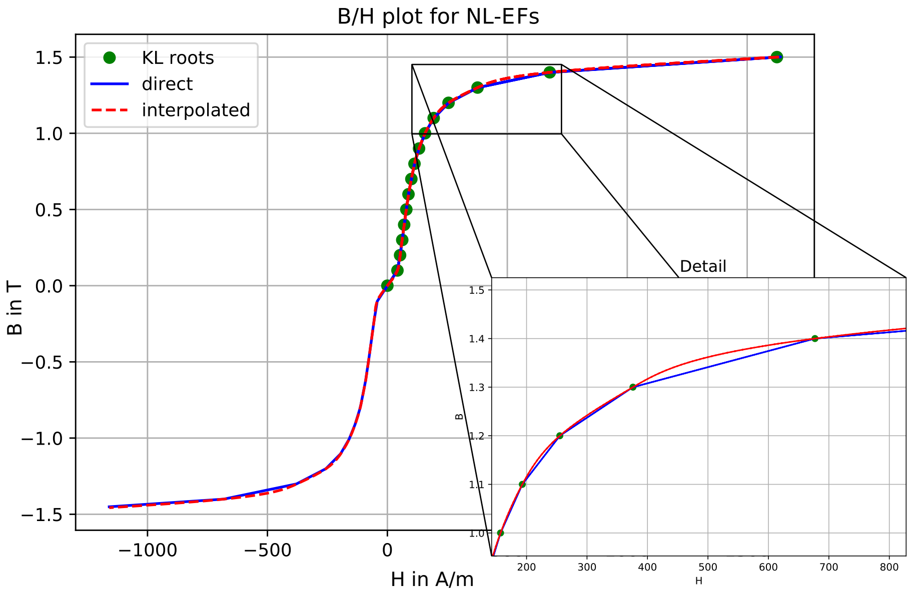

Figure D.1: Output Signal of two SPMs. Both based on the same initial magnetisation curve. One EF uses the magnetisation curve directly, the other one interpolates it with a cubic spline.

Eidesstattliche Erklärung

Hiermit erkläre ich, dass die vorliegende Arbeit gemäß dem Code of Conduct, insbesondere ohne unzulässige Hilfe Dritter und ohne Benutzung anderer als der angegebenen Hilfsmittel, angefertigt wurde. Die aus anderen Quellen direkt oder indirekt übernommenen Daten und Konzepte sind unter Angabe der Quelle gekennzeichnet. Die Arbeit wurde bisher weder im In- noch im Ausland in gleicher oder in ähnlicher Form in anderen Prüfungsverfahren vorgelegt.

Wien, am 04. Mar. 2021

Valentin Hanser, BSc